MAX-PLANCK-INSTITUT
FÜR METEOROLOGIE

Uncovering the effects of Agulhas eddies on low and high internal tide modes and their energetics in high-resolution ICON

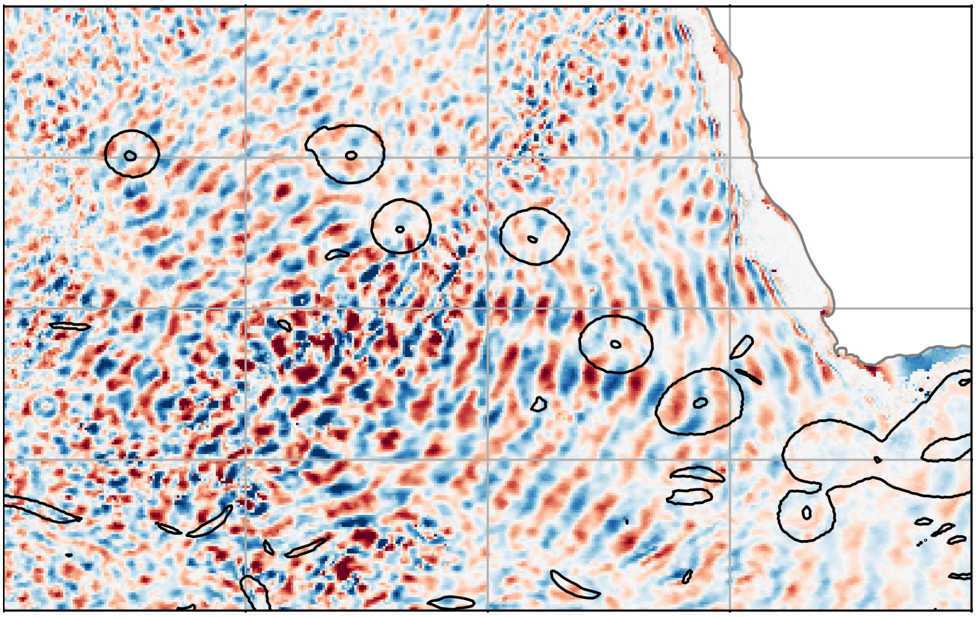

Zoi Kourkouraidou

Hamburg 2025

Berichte zur Erdsystemforschung
Reports on Earth System Science

294
2025

Hinweis

Die Berichte zur Erdsystemforschung werden vom Max-Planck-Institut für Meteorologie in Hamburg in unregelmäßiger Abfolge herausgegeben.

Sie enthalten wissenschaftliche und technische Beiträge, inklusive Dissertationen.

Die Beiträge geben nicht notwendigerweise die Auffassung des Instituts wieder.

Die "Berichte zur Erdsystemforschung" führen die vorherigen Reihen "Reports" und "Examensarbeiten" weiter.

Notice

The Reports on Earth System Science are published by the Max Planck Institute for Meteorology in Hamburg. They appear in irregular intervals.

They contain scientific and technical contributions, including PhD theses.

The Reports do not necessarily reflect the opinion of the Institute.

The "Reports on Earth System Science" continue the former "Reports" and "Examensarbeiten" of the Max Planck Institute.

Anschrift / Address

Max-Planck-Institut für Meteorologie
Bundesstrasse 53
20146 Hamburg
Deutschland

Tel./Phone: +49 (0)40 4 11 73 - 0
Fax: +49 (0)40 4 11 73 - 298

name.surname@mpimet.mpg.de
www.mpimet.mpg.de

Layout

Bettina Diallo and Norbert P. Noreiks
Communication

Copyright

Photos below: ©MPI-M
Photos on the back from left to right:
Christian Klepp, Jochem Marotzke,
Christian Klepp, Clotilde Dubois,
Christian Klepp, Katsumasa Tanaka

Uncovering the effects of Agulhas eddies on low and high internal tide modes and their energetics in high-resolution ICON

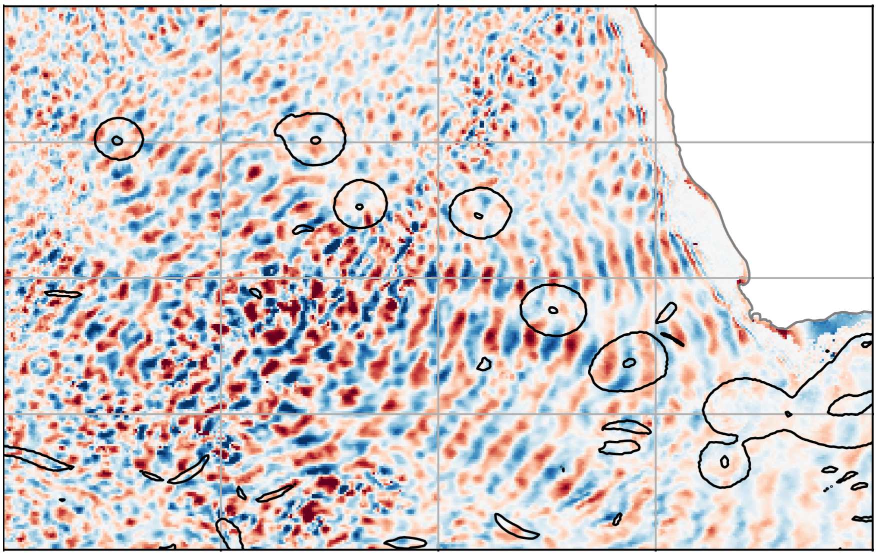

Zoi Kourkouraidou

Hamburg 2025

Zoi Kourkouraidou
aus Thessaloniki, Griechenland

Max-Planck-Institut für Meteorologie
The International Max Planck Research School on Earth System Modelling
(IMPRS-ESM)
Bundesstrasse 53
20146 Hamburg

Tag der Disputation: 30. Oktober 2025

Folgende Gutachter empfehlen die Annahme der Dissertation:
Prof. Dr. Jin-Song von Storch
Dr. Nils Brueggemann

Vorsitzender des Promotionsausschusses:
Prof. Dr. Hermann Held

Dekan der MIN-Fakultät:
Prof. Dr.-Ing. Norbert Ritter

Titelgrafik: *A snapshot of the M2 internal tide zonal velocity (colour shadings) at ca. 100m depth, together with Agulhas Rings (black lines) simulated by ICON-O. The Agulhas Rings are described by the mean horizontal current speed. By Zoi Kourkouraidou*

Berichte zur Erdsystemforschung / Max-Planck-Institut für Meteorologie 294
Reports on Earth System Science / Max Planck Institute for Meteorology 2025

ISSN 1614-1199 - doi: 10.17617/2.3684496

For the one who kept moving forward

ABSTRACT

The interaction between internal tides and mesoscale eddies is one of the processes which are thought to significantly contribute to energy dissipation and diapycnal mixing in the open ocean. Yet the details of such interactions still remain poorly understood. Observational, theoretical as well as numerical studies in idealized conditions have tried to shed light to these interactions. However, these can only capture aspects of the effects of mesoscale eddies on internal tides that are very localized, confined in time or oversimplified.

To date, no study has examined eddy - internal tide interactions using a comprehensive ocean model that resolves both features in a realistic setting. In this thesis I investigate these interactions in the southeast Atlantic, near the Walvis Ridge, where both features are strongly present, using the ocean-only ICON model with very high horizontal resolution. The study proceeds in three parts: First, focussing on the modal decomposition of the internal tidal (IT) waves resolved and diagnosed by the model, I highlight the limitations of the standard method based on linear wave theory and present an alternative based on data-driven empirical orthogonal function (EOF) analysis, which is more suitable for our model output since it inherently accounts for the influence of the bathymetry and stratification, but also of the mean currents resolved by our model. Second, focussing on the effects of Agulhas rings on the low and high modes of the internal tide, I use both decomposition methods to quantify the eddy effects during two seasons. An Agulhas ring that crosses a beam of M2 mode-1 IT is causing horizontal refraction, seen as a southward shift of the beam, without significantly altering the vertical component. This indicates that the Agulhas ring does not scatter the mode-1 IT into higher modes. Instead, higher IT modes are found to be trapped within the Agulhas rings before the interaction with mode-1 beams, implying that they do not necessarily arise from this interaction. Third, focussing on the energetics of the internal tide - eddy interactions I aim to answer whether and to what extent the overall energetics in the study area are altered due to the presence of eddies and whether or not the energy flux of the low-mode IT is more strongly damped in the presence of eddies. Together, my results offer new insights into IT-eddy interactions and their energetics in a realistic setting and introduce a framework for analyzing internal tides beyond linear wave assumptions, which is essential as computational power and model resolution continue to advance, making the resulting data increasingly complex.

ZUSAMMENFASSUNG

Die Wechselwirkung zwischen internen Gezeiten und mesoskaligen Wirbeln gilt als ein Prozess, der maßgeblich zur Energiedissipation und diapyknischen Mischung im offenen Ozean beiträgt. Die genauen Mechanismen dieser Wechselwirkungen sind jedoch nach wie vor nur unzureichend verstanden. Beobachtungsbasierte, theoretische sowie numerische Studien unter idealisierten Bedingungen haben versucht, diese Prozesse zu beleuchten. Sie erfassen jedoch meist nur sehr lokale, zeitlich begrenzte oder stark vereinfachte Aspekte der Auswirkungen mesoskaliger Wirbel auf interne Gezeiten. Bislang wurde keine Studie durchgeführt, die solche Wechselwirkungen mithilfe eines umfassenden Ozeanmodells untersucht, das beide Phänomene in realitätsnaher Weise auflöst.

In dieser Arbeit untersuche ich diese Wechselwirkungen im südöstlichen Atlantik nahe des Walvis-Rückens, einer Region, in der sowohl interne Gezeiten (IT) als auch mesoskalige Wirbel stark ausgeprägt sind. Grundlage ist das Ozeanmodell ICON in einer hochaufgelösten Konfiguration.

Die Studie gliedert sich in drei Teile: Zunächst liegt der Fokus auf der modalen Zerlegung der durch das Modell aufgelösten und diagnostizierten internen Gezeiten. Ich zeige die Grenzen der Standardmethode auf, die auf linearer Wellentheorie basiert, und stelle eine alternative Methode vor, die auf empirischer orthogonaler Funktionsanalyse (EOF) beruht. Diese datenbasierte Methode ist besser geeignet für unsere Modellausgabe, da sie nicht nur die Effekte von Bathymetrie und Schichtung, sondern auch die der mittleren Strömungen berücksichtigt.

Im zweiten Teil werden die Auswirkungen von Agulhas-Ringen auf niedrige und höhere Moden der internen Gezeiten untersucht. Beide Zerlegungsmethoden werden eingesetzt, um die Wirbeleffekte über zwei Jahreszeiten hinweg zu quantifizieren. Ein Agulhas-Ring, der einen Strahl der M2-Mode-1-IT kreuzt, verursacht eine horizontale Refraktion, erkennbar an einer südlichen Verschiebung des Strahls, während die vertikale Struktur weitgehend unverändert bleibt. Dies deutet darauf hin, dass der Agulhas-Ring keine signifikante Streuung der Mode-1-Gezeitenenergie in höhere Moden verursacht. Stattdessen sind höhere Moden bereits innerhalb der Wirbel gefangen, bevor sie mit dem Mode-1-Strahl interagieren, was darauf hindeutet, dass sie nicht zwangsläufig durch diese Wechselwirkung entstehen.

Im dritten Teil steht die Energiebilanz der Wechselwirkung im Vordergrund. Ziel ist es zu klären, ob und in welchem Maße mesoskalige Wirbel die Gesamtenergetik im Untersuchungsgebiet beeinflussen und ob der Energiefluss der niederfrequenten IT-Moden durch ihre Anwesenheit stärker gedämpft wird.

Insgesamt liefert diese Arbeit neue Erkenntnisse zu Wechselwirkungen zwischen internen Gezeiten und mesoskaligen Wirbeln und deren energetischen Konsequenzen unter realistischen Bedingungen. Darüber hinaus wird ein Analyseansatz vorgestellt, der über die Annahmen der linearen Wellentheorie hinausgeht – ein notwendiger Schritt angesichts zunehmender Modellkomplexität und steigender Rechenleistung.

PUBLICATIONS RELATED TO THIS DISSERTATION

The following two studies are part of this dissertation:

- **The M2 internal tide and its interaction with eddies in the Walvis ridge area simulated by a 5km ICON-O**

  Z.Kourkouraidou, J-S.von Storch (2025a)

  submitted in *Journal of Physical Oceanography*

- **Energetics of the internal tide - eddy interaction in a kilometer scale configuration of ICON-O**

  Z.Kourkouraidou, J-S.von Storch (2025b)

  in preparation for submission

As a PhD candidate I have contributed to an additional project, which is currently in preparation for submission:

- **The M2 internal tide generation: linear wave theory vs. high-resolution GCM**

  J-S.von Storch, **Z.Kourkouraidou**, Friederike Pollmann (2025)

  in preparation for submission

ACKNOWLEDGEMENTS

The completion of this thesis would not have been possible without the support, patience, and kindness of many people.

First and foremost, I want to thank my main supervisor, Jin, for patiently guiding me along my PhD path, for countless motivating and enlightening discussions and for always trusting me to find my way—even when I wasn't entirely sure where that way was. I'm also grateful to some past and present members of my working group, especially Dian, Florian, and Fraser, for answering all my "stupid"—I mean, perfectly reasonable—questions in those early months (and sometimes much later). My thanks also go to my panel members, Georg-Sebastian, Manita and Carsten, for their guidance and support throughout my work. Special appreciation goes to Helmuth, Nils, and Peter for their much-valued technical wizardry with ICON, and to the wonderful IMPRS office team—Antje, Florian, Connie, and Michi—for keeping everything running so smoothly.

A huge thank-you to everyone involved in the research cruise SONNETT II (M188) for making those six weeks aboard *RV Meteor* in the southeast Atlantic such an unforgettable adventure. It was a true honour to "see the real ocean" for the first time with you.

I also want to thank Dallas and Jens for their valuable comments on the very first draft of my paper during the Scientific Writing course.

To Lucas—best office mate ever, and a steady anchor through all the storms. To my IMPRS cohort—thank you for the endless lunch breaks, coffee runs, after-work drinks, spontaneous trips, and deep (and not-so-deep) discussions. To the "writing warriors"—Lucas, Quan, Arim, Abisha, and Jacqueline—thank you for sharing the highs and lows of spending the sunniest season of the year indoors, glued to our laptops. To my reading club—Melissa, Robert, Konsti, Felix, Fred, Jacob, Benni, and Manu—thank you for proof-reading the final version and catching the mistakes that I had stopped seeing.

And finally, to my family and friends—especially Eleni, Melissa, Elina and Evita: thank you from the bottom of my heart for all the emotional support, encouragement, and occasional reality checks that got me through the past years.

CONTENTS

1 INTRODUCTION 1
- 1.1 Motivation 1
- 1.2 Background 3
  - 1.2.1 Internal wave driven mixing 3
  - 1.2.2 Internal tides and mesoscale eddies 4
  - 1.2.3 Current understanding and research gap 5
- 1.3 Research Questions and Structure of the Thesis 7
  - 1.3.1 Research Questions 7
  - 1.3.2 Structure of the thesis 8

2 METHODOLOGY 9
- 2.1 Numerical approach 9
  - 2.1.1 ICON-O 9
  - 2.1.2 Experimental Set-up 10
- 2.2 The M2 Internal Tide in ICON 11
  - 2.2.1 Baroclinic velocity at M2 frequency 11
  - 2.2.2 Internal Tide Kinetic Energy 12
  - 2.2.3 Baroclinic energy flux at M2 frequency 12
- 2.3 The Area of Focus: the Internal Tide Generated at the Walvis Ridge and its Wave Environment 14
  - 2.3.1 Mesoscale Agulhas Rings and Bathymetry 15
  - 2.3.2 Stratification 16

3 VERTICAL MODE DECOMPOSITION: A NOVEL DATA-DRIVEN METHOD AND COMPARISON TO LINEAR WAVE THEORY BASED METHODS 19
- 3.1 Introduction 19
- 3.2 Model data 21
- 3.3 A novel modal decomposition method based on Empirical Orthogonal Functions 21
  - 3.3.1 EOF modes of the M2 Internal Tide in the Walvis Region 25
- 3.4 The Sturm-Liouville modal decomposition method 27
  - 3.4.1 The exact solution 28
  - 3.4.2 The approximate vertical modes 33
- 3.5 Summary and Discussion of Chapter 3 34

4 EFFECTS OF MESOSCALE EDDIES ON THE M2 INTERNAL TIDE AND ITS MODES IN DIFFERENT SEASONS 37
- 4.1 Introduction 37
- 4.2 Experimental set-up and research approach 39
- 4.3 Frequency Stability of the M2 Internal Tide in the Presence of Agulhas Rings 41
- 4.4 Impact of Agulhas Rings on the Low Modes 41
- 4.5 Impact of Agulhas Rings on High Modes 46
- 4.6 Effects of Seasonality on the Interactions 48
- 4.7 Representation of Eddy Effects by Alternative Decomposition Methods 51
  - 4.7.1 Exact SL solution 51

4.7.2 Approximate SL solution 52
4.8 Summary and Discussion of Chapter 4 56
5 ENERGETICS OF THE EDDY - INTERNAL TIDE INTERACTIONS 59
5.1 Introduction 59
5.2 The SMT simulation and experimental approach 61
5.3 High mode waves in the SMT simulation 62
5.4 Baroclinic energy flux ratios in regions with varying background eddy activity 63
5.4.1 Super- and subinertial baroclinic energy fluxes 63
5.4.2 Energy fluxes across corridors 64
5.4.3 Energy Flux Ratios in Domains with Varying Eddy Activity . 65
5.4.4 Directional Energy Fluxes Along and Across the Eddy Propagation 67
5.5 Summary and Discussion of chapter 5 68
6 CLOSING THOUGHTS 71
6.1 Summary and Conclusions 71
6.2 Looking ahead 73
A APPENDIX 77
A.1 Introduction 79
A.2 ICON-O Model and the Area of Focus Simulated by ICON-O 81
A.2.1 ICON-O and Experimental Set-up 81
A.2.2 The Area of Focus: the Internal Tide Generated at the Walvis Ridge and Agulhas Rings 81
A.2.3 The Wave Environment 84
A.3 Methodology 85
A.3.1 M2 Internal Tide in ICON-O 85
A.3.2 Mode Decomposition 87
A.3.3 M2 energy flux 90
A.3.4 Kinetic Energy 90
A.4 Results 92
A.4.1 Modes of the M2 Internal Tide in the Walvis Region 92
A.4.2 Impact of Agulhas Rings on the Mode 1 96
A.4.3 Impact of Agulhas Rings on High Modes 100
A.4.4 IT modes derived from Sturm-Liouville equation 101
A.5 Summary and Concluding Remarks 103

BIBLIOGRAPHY 107

1

INTRODUCTION

> *Even if you never have the chance to see or touch the ocean,*
> *the ocean touches you with every breath you take,*
> *every drop of water you drink, every bite you consume.*
> *Everyone, everywhere is inextricably connected to*
> *and utterly dependent upon the existence of the sea.*
> *— Sylvia A. Earle (2009)*
> *The World Is Blue: How Our Fate and the Ocean's Are One*

1.1 MOTIVATION

Modern climate science is driven by a central concern: human activities are intensifying the greenhouse effect in Earth's atmosphere, causing the planet's surface to warm. This trend is robustly documented and scientifically well-established (Masson-Delmotte et al., 2018; IPCC, 2023). Yet, understanding the broader implications of this warming, how it will reshape global climate patterns, disrupt atmospheric and oceanic circulation, alter weather extremes, and affect ecosystems and human societies, remains a major scientific challenge. These open questions are at the heart of climate research today. To address them, we must first deepen our understanding of the Earth's climate system as a whole.

A critical component of that system is the ocean. Covering approximately 71% of Earth's surface, the ocean stores 96.5% of the planet's near-surface liquid water. It is not only vast in size, but also in influence: the ocean acts as the primary reservoir of heat and carbon, helping to regulate Earth's temperature and driving large-scale atmospheric circulation. Its thermal inertia is immense, its heat capacity is about four times that of the atmosphere, and its mass is roughly 250 times greater. Consequently, warming the ocean by 1 K requires about 1,000 times more energy than warming the atmosphere by the same amount (Stevens, Brovkin, and Weitz, 2022). However, the ocean is not a passive heat sink. Its dynamics, currents, waves, eddies, large-scale circulation patterns, and vertical mixing, are driven by winds, tides, buoyancy forces, and Earth's rotation. These physical processes strongly influence climate variability and determine how the Earth system responds to continued warming.

Advancements in satellite altimetry in the recent decades, including the recently launched satellite mission, SWOT, have significantly improved our understanding of the ocean's surface. Through satellite observations, we can now monitor sea surface height, temperature, and currents with remarkable precision and spatiotemporal resolution (Srinivasan and Tsontos, 2023; Yao et al., 2025). However, our knowledge of the ocean beneath the surface, where most of its volume and variability reside, remains limited. Autonomous instruments like Argo floats have expanded our insights into the upper ocean by profiling temperature and salinity down to depths of around 2 kilometers (Johnson et al., 2022).

For higher depths (> 2km) there exist at present approximately 200 Deep Argo floats sampling some of the deepest regions of the ocean (Zilberman et al., 2023). Yet, gaining a clear picture of the deep ocean still relies on costly, time-limited ship-based observations.

To overcome these observational limitations, scientists increasingly rely on numerical models to simulate the ocean and the processes that shape it. The resolution of these models determines how much of the ocean's complexity can be explicitly captured. Finer-resolution models resolve more features, such as eddies, internal waves, and sharp gradients,while unresolved processes must be parameterized. Simulating ocean dynamics is inherently challenging, because they span a vast range of temporal and spatial scales, from planetary-scale circulation patterns and decade-long climate oscillations to minute-scale turbulence and meter-scale waves. No single model can fully capture this entire range, and choices must always be made based on the specific scientific question at hand.

Observations remain essential in this modeling framework. They not only serve to validate model outputs, but also guide the improvement of parameterizations and deepen our understanding of processes that models cannot yet resolve. In this way, observations and models are tightly interlinked, observations inform models, and models provide a structured context for interpreting observations (Stevens, Brovkin, and Weitz, 2022). Yet, developing an energy-consistent ocean model is not a trivial process. The effects of unresolved or not-yet-understood dynamics are often neglected or, at best, represented through parameterizations that rely on simplified physical relationships and approximations. If essential processes are inadequately parameterized or entirely neglected, models can become energetically inconsistent, violating fundamental physical principles such as the conservation of energy, mass and momentum. These violations can lead to biases in simulations of the current climate and wrong predictions of future climates.

Recent advances in computational efficiency and in translating physical principles into numerical algorithms now allow us to resolve and study processes on unprecedented resolution. This progress improves our ability to explore how small-scale processes and dynamics interact with larger dynamical processes of the climate system. In general, the more accurately we can represent and understand such crucial processes, the better and more energy consistent the models become. However, *"all models are wrong, but some are useful"* (Box, 1979). In our case we can interpret this well-known aphorism as follows: As numerical models grow in complexity and realism, interpreting their output becomes more and more challenging. While simplified, idealized models offer clarity and insight, realistic simulations often require new diagnostics to extract meaningful understanding from their rich and intricate dynamics. The choice of analysis techniques and even the model configuration itself must be tailored to the scientific question at hand, whether that involves long-term climate variability or short-term, high-frequency processes.

This thesis aims to contribute to this effort by focusing on one crucial component of oceanic dynamics, the internal tide, and its interaction with a part of the mean flow. The following section highlights the importance of these interactions, describes the prevailing scientific knowledge and the remaining research gap, which I intend to reduce.

1.2 BACKGROUND

1.2.1 *Internal wave driven mixing*

One of the most posed questions in physical oceanography is concerned about how energy transfers through scales, mixing the waters of different depths and densities and finally dissipates. Understanding ocean energetics and reducing uncertainties in climate models presents a central role but also a key challenge of today's research.

Internal gravity waves (IGWs) are waves in the ocean interior with gravity as their restoring force and are generated by a plethora of mechanisms. Some of the most prominent ones is tidal flow over topography, which generates internal tidal waves (ITs), wind variations at the sea surface, which generates near-inertial waves (NIWs), and flow of ocean currents and eddies over topography, which lead to the generation of lee waves.

As internal gravity waves propagate horizontally and vertically away from their generation sites, they interact with each other, which produces an internal gravity wave continuum consisting of energy in many wavenumbers and frequencies. Waves with high vertical wavenumbers and small horizontal and vertical scales are more likely to break, leading to turbulent mixing. The dissipation of turbulent energy in stratified water results in irreversible mixing across density surfaces, also called diapycnal mixing (MacKinnon et al., 2017). Depending on the spatial and temporal scales of different oceanic motions and processes, some of them can interact with each other and lead to dissipation.

Some of the most important processes that contribute to energy dissipation and diapycnal mixing are shown in Fig. 1. Here we will focus on the two processes indicated by the green box: the internal waves at tidal frequencies and their interaction with mesoscale eddies.

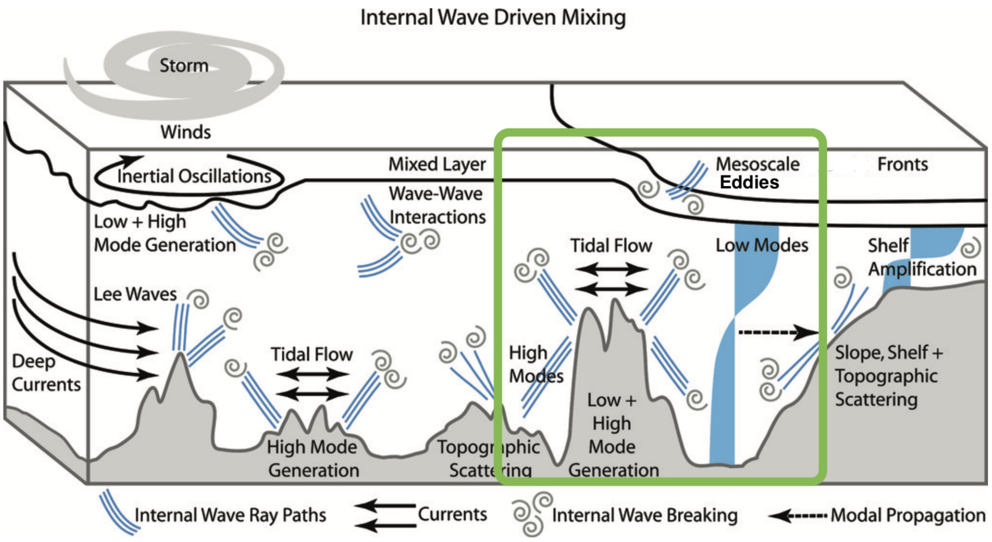

Figure 1: Schematic of internal wave mixing processes in the open ocean. We focus on the one caused by interactions of internal tides with mesoscale eddies, shown in the green box. Figure adapted from MacKinnon et al., 2017

1.2.2 *Internal tides and mesoscale eddies*

Internal tides (ITs) are internal gravity waves (IGWs) at tidal frequencies generated when ocean tidal currents impact rough topography, forcing stratified water to oscillate vertically (Garrett and Kunze, 2007), as indicated in the green box in Fig. 1. During this interaction with topography both low and high modes of the IT are generated (Garrett and Kunze, 2007; MacKinnon et al., 2017). The high modes are connected to small horizontal and vertical structures and tend to dissipate quickly close to the generation sites (Simmons and Alford., 2012; Vic, Naveira Garabato, and Green, 2019). The low modes on the other hand are connected to large horizontal structures (≈ 100km) and can propagate thousands of kilometers away from the generation sites carrying the largest part of the IT energy, as suggested by IT signatures extracted from altimetry (Ray and Mitchum, 1997; Zhao and Alford, 2009; Zhao et al., 2011; Cummins, Cherniawsky, and Foreman, 2001) in several regions worldwide. Diapycnal mixing induced by the breaking of the low modes of the IT contributes significantly to sustaining the global overturning circulation. In fact it was previously estimated to contribute with roughly 50% (1 TW) of the total energy needed to sustain the circulation (Munk and Wunsch, 1998; Ferrari and Wunsch, 2009).

Figure 2 shows the spatial and temporal scales of important oceanic motions (pink areas), namely the general circulation (left), the internal wave and mesoscale eddy compartments (middle), and the turbulence (right). Internal tides, as explained above, are found in the internal wave compartment, in the upper side of the green box. The frequency domain of such waves is rather sharply defined as clear peaks between the Brunt–Väisälä frequency N and Earth's rotation frequency f, while spatial scales can range depending on the wave mode.

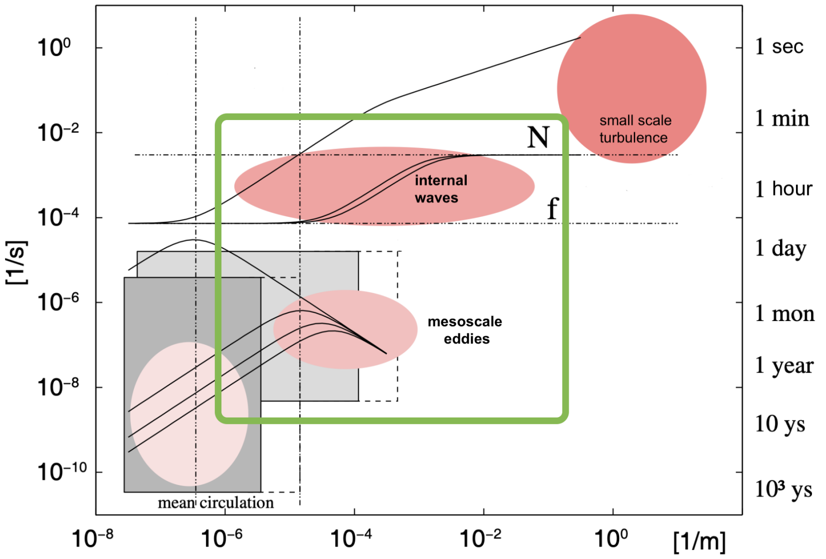

Figure 2: Spatial and temporal scales of oceanic processes (pink) and the ones explicitly resolved by state-of-the-art ocean models (grey boxes, expanded with dashed lines). The green box indicates the domain where internal waves and mesoscale eddies are located. Figure adapted from D.Olbers, C.Eden, and J.Willebrand, 2012.

1.2.3 *Current understanding and research gap*

There exist several processes that can lead to dissipation of the internal tide, especially its low modes. Here we mention the most dominant ones. One is the interaction with topography, which has been in focus of several studies, using both numerical simulations (Johnston and Merrifield, 2003; Buijsman et al., 2020) and observational data (Klymak, Pinkel, and Rainville, 2008). The other is wave-wave interaction, eg. nonlinear interactions that transfer energy via the parametric subharmonic instability (MacKinnon et al., 2013) to subharmonic frequencies and higher wavenumbers near a critical latitude. Yet another process is the interaction between ITs and mesoscale eddies. The mesoscale eddy field, also depicted in the green box of figure 2 involves spatial scales of several 100 kilometers down to kilometers and time scales of days to months. The comparable spatial scales of mesoscale eddies and low-mode internal tides create favorable conditions for interaction.

Evidence suggesting eddy-IT interactions has been found from direct observations (Löb et al., 2020; Huang et al., 2018; Cusack et al., 2020). In the Azores, Löb et al. (2020) detect a damped energy flux in the first and second mode, which could be interpreted as a result of scattering of lower to higher modes. However, they cannot conclusively prove this by using their mooring data. Huang et al. (2018) observe a weakening of low modes and a change in the propagation speed of the IT due to two eddies in the South China Sea. Cusack et al. (2020) deployed a mooring array over an abyssal hill in the Scotia Sea and found that eddies gain energy from the internal wave field, with around 50% of this exchange occurring at the tidal frequency. These results suggest that interactions with internal tides may also play a significant role in modifying the mesoscale eddy field in the Southern Ocean. Yet, observations are still too sparse in time and space to be sufficient for describing the details of the interactions. Especially resolving the high modes, which are crucial for identifying potential scattering of low modes by eddies, remains a significant challenge for observational studies.

To get more insight into this process, theoretical and numerical approaches have been considered. An example of a theoretical approach is the study by Savva, Kafiabad, and Vanneste (2021a), where the effect of geostrophically balanced turbulent flows on internal gravity waves was examined using a kinetic equation that governs the evolution of internal gravity wave energy density under certain assumptions about the quasi-geostrophic flows. Several studies have been carried out following numerical approaches (Dunphy et al., 2017; Dunphy and Lamb, 2014; Wang and Legg, 2023; Shakespeare, 2023). There, the wave-eddy interaction is examined using numerical models configured for idealized conditions. For example Dunphy and Lamb (2014) showed that baroclinic eddies can scatter a portion of the incident wave to higher vertical modes and wavenumbers, while energy is transferred from low modes to high modes through the eddy-IT interaction in an idealized configuration, while Wang and Legg (2023) found that higher modes are trapped inside eddies. Shakespeare (2023) focussed on the influence of internal tides on mesoscale eddies using a simple theoretical model and found that internal tides can, in the presence of a critical level, accelerate the eddies by increasing the eddy kinetic energy and reduce their lifetimes.

Recently, Wang and Legg (2025) combined observational data from Argo floats and numerical simulations and found that Agulhas rings serve as hotspots for internal tide dissipation.

Nonetheless, such models cannot sufficiently capture the complexity of the eddy-IT interactions, since they model very idealized conditions eg. unrealistic stratification, flat bottom, absence of mean flow etc. To date and to the best of our knowledge, there exists no study leveraging a high-resolution complex GCM to address this topic, leaving a significant research gap.

This work aims to reduce this gap employing the global, complex, state-of-the-art GCM *ICON* with very high spatial and temporal resolution with realistic topography and reanalysis data as surface boundary conditions, thereby creating a very realistic [1] set-up for the interactions. With this set-up, which enables us to realistically resolve both features, we try to provide some advanced understanding on the nature of the interactions and their impact on the energetics of the research area. Through this, we also demonstrate how targeted diagnostics can unlock new insights from increasingly realistic ocean simulations.

---

[1] Using the term 'realistic', we mean that we apply realistic topography and use reanalysis data as surface boundary conditions. Despite that, we are aware that our model configuration is subject to inaccuracies originating from errors due to numerics and parameterizations. Additionally, it is important to note that the quantitative results presented in this study are inherently influenced by the specific characteristics of the model used.

1.3 RESEARCH QUESTIONS AND STRUCTURE OF THE THESIS

Despite the significance of these interactions, it remains unclear how exactly mesoscale eddies impact the internal tide in a realistic setting. In such a setting, decomposing the resolved internal tide into vertical modes is not a trivial task. The fate of the low modes, along with their associated energy pathways and dissipation mechanisms, has yet to be fully characterized. Likewise, the question of whether the trapping of high modes inside an eddy, as reported in previous studies, truly results from the scattering of a low-mode internal tide remains open. This thesis addresses these gaps. Through our analysis, we pioneer the investigation of the eddy-IT interactions in realistic high-resolution ocean model configurations. We also aim to contribute to the understanding of analysis methods in GCM output, which is growing in complexity and increasingly resemble the ones obtained from the real ocean.

1.3.1 *Research Questions*

To address the gaps named above, I pose the following research questions:

Q1?

To what extent is the standard normal mode decomposition, derived from linear wave theory, applicable for studying internal tides in a complex, realistically simulated ocean environment and what can we learn from comparing this method with a data-driven one?

We introduce an alternative approach based on empirical orthogonal functions (EOFs) to extract IT modes from ICON simulations. Unlike traditional linear wave theory or the commonly used Sturm-Liouville decomposition, our method makes no assumptions about background stratification or wave linearity. It yields spatially coherent, three-dimensional wave structures influenced by both bathymetry and ambient currents. While Sturm-Liouville modes are solved independently at each location, our EOF-based modes capture horizontal wave propagation and preserve physical connectivity across the domain.

Q2?

What are the effects of mesoscale eddies on the low and high modes of the M2 internal tide in different seasons?

We decompose the lunar semidiurnal (M2) internal tide into low and high modes using both the linear wave theory-based method and our novel EOF-based method to study the impact of an Agulhas ring on the modes in different seasons. Despite methodological differences, both methods lead to similar results suggesting that nonlinear effects might be negligible.

Q3?

How do Agulhas rings influence the energetics in the Walvis ridge area, especially the energy flux of the internal tide?

We calculate the depth integrated baroclinic energy fluxes in areas with strong and weak eddying background to assess the impact of Agulhas rings on the energetics of the research area. We find that mesoscale eddies potentially play an important role in redirecting but also in gaining energy.

1.3.2 *Structure of the thesis*

The thesis is structured as follows:

Chapter 2 introduces the numerical model and the experimental set-up used in the thesis. It presents the methodology used to diagnose and compute important properties of the M2 IT, describes the area of focus and the physical environment of the IT, as it is resolved by our model.

Chapter 3 explains the reasons why standard decomposition methods based on linear wave theory are not ideal for studying eddy-IT interactions from high-resolution complex model output, as in our case. It introduces a novel method based on EOF spatial analysis and compares its results with two different variations of the standard decomposition method based on linear wave theory.

In chapter 4 we apply both the novel and the standard decomposition method to study the impact of Agulhas rings on the IT generated at the Walvis ridge during two different seasons. The research presented in chapters 3 and 4 has been written up together as one manuscript and submitted in the *Journal of Physical Oceanography*. The complete manuscript can be found attached in the appendix of this thesis.

Chapter 5 introduces a new configuration of ICON-O and the strategy used to quantify the energetics of the region as well as the influence of mesoscale eddies therein. Preliminary results on possible energy dissipation caused by the wave-eddy interaction are shown.

Lastly, chapter 6 summarizes the main results of the thesis and gives an outlook for future research.

METHODOLOGY

2

In this chapter, we introduce the main methods used in the thesis. We present the numerical approach by introducing the ICON-O model and our experimental set-up in 2.1. In section 2.2 we present the derivation of the M2 internal tide velocity, kinetic energy and energy flux. Finally, in 2.3 we describe the study area.

2.1 NUMERICAL APPROACH

2.1.1 *ICON-O*

The general circulation ocean-only model used in this study is ICON-O (Korn, 2018; Korn et al., 2022), a primitive equation global model recently developed at the Max-Planck-Institute for Meteorology. The model can be run including the barotropic tides by enabling the luni-solar tidal forcing in the momentum equation. ICON-O without being constrained by observations is able to realistically simulate the major features of barotropic tides (von Storch et al., 2023).
The horizontal grid of ICON-O is formed by 20 triangles (ICOsahedron), which are recursively divided at the middle of each edge, allowing for smaller triangles to be created, as depicted in figure 3.

The number of subdivisions defines the horizontal resolution of the grid, as explained in more detail in Giorgetta et al. (2018). In the vertical, the z^* coordinate introduced by Adcroft and Campin (2004) is used. The vertical resolution is defined by 128 vertical levels and gradually varies between less than 10m in the upper 140m and 200m below 4544m of the water column. The parameterization of mesoscale eddies, expressed as eddy induced diffusion and eddy induced advection, are deactivated. The turbulent vertical mixing is parameterized following Gaspar, Yves, and Lefevre (1990). ICON-O incorporates a sea ice model consisting of dynamic and thermodynamic components.

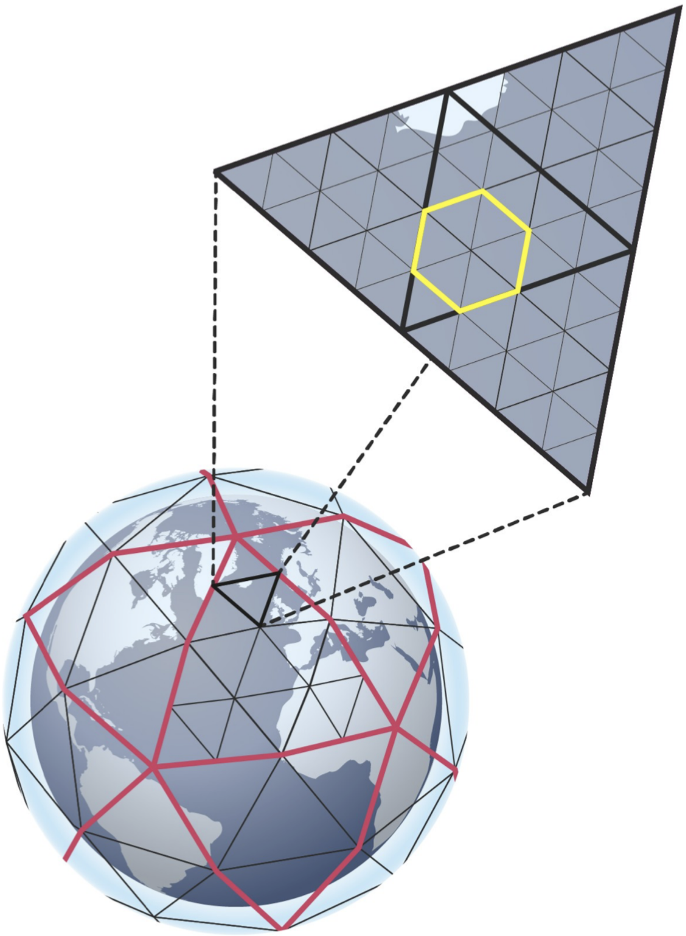

Figure 3: Horizontal grid of ICON. Magenta triangles represent the main icosahedral grid and the black ones the high-resolution grid obtained by recursively dividing the main grid. Figure adapted from the MPI-M website.

2.1.2 *Experimental Set-up*

To answer the three main research questions of this thesis in the next three chapters, we use two different configurations of ICON-O.

For the first two chapters, we use the ICON-R2B9 grid (in the following, R2B9), corresponding to a horizontal resolution of about 5 km globally. Some features of ICON-O with an R2B9 grid coupled to the atmospheric component ICON-A at the same R2B9 grid can be found in Hohenegger et al. (2023), Gutjahr et al. (2022), and von Storch and Lüschow (2023). More details for the experimental set-up and the data used for each study are found in chapters 3 and 4 respectively. For the third study we use a different configuration, the ICON-SMT (in the following, SMT), which allows for a gradual refining of the horizontal grid from 5km globally to approximately 600m in the focus region. This simulation is explained in more detail in chapter 5.

2.2 THE M2 INTERNAL TIDE IN ICON

2.2.1 *Baroclinic velocity at M2 frequency*

To study the interaction of internal tides with eddies, we need to first identify the internal tide simulated by the ICON-O model. This is done by first calculating the baroclinic horizontal velocity $\mathbf{u}'$ from the full horizontal velocity $\mathbf{u} = (u, v)$ as

$$\mathbf{u}' = \mathbf{u} - \mathbf{U} \quad \text{with} \quad \mathbf{U} = \frac{1}{\eta + d} \int_{d}^{\eta} dz\, \mathbf{u}(x, y, z, t) \tag{1}$$

where η is the surface elevation and d the bottom depth [1].

The baroclinic velocity $\mathbf{u}'_{bcl}$ contains motions at all possible frequencies. We then apply harmonic analysis (Foreman, Cherniawsky, and Ballatyne, 2008) to $\mathbf{u}'_{bcl}$ at each grid point (x, y, z) to get the amplitudes $A(x, y, z)$ and phases $\phi(x, y, z)$ for different constituents of the internal tide at that grid point. The analysis is done for hourly data within one month. Below, we focus on the M2 internal tide. The full M2 internal tide zonal velocity is then given by (dropping the subscript M2)

$$\begin{aligned} u'(x, y, z, t) &= \mathbb{R}e\Big(A(x, y, z)e^{i(\omega t - \phi(x,y,z))}\Big) \\ &= A(x, y, z)\Big(\cos(\phi(x, y, z))\cos(\omega t) + \sin(\phi(x, y, z))\sin(\omega t)\Big) \\ &= C(x, y, z)\cos(\omega t) + S(x, y, z)\sin(\omega t) \end{aligned} \tag{2}$$

with

$$C(x, y, z) = A(x, y, z)\cos(\phi(x, y, z)), \quad S(x, y, z) = A(x, y, z)\sin(\phi(x, y, z)), \tag{3}$$

where $\mathbb{R}e(\cdot)$ indicates the real part of its argument, ω is the M2 angular frequency. A similar expression is obtained for the meridional velocity v'.

Harmonic analysis, while useful for identifying the frequency components of internal tides, does not reveal the nature of the wave, such as whether it propagates horizontally, vertically, or in a more complex manner in three-dimensional space. To understand the propagation characteristics of internal tides, one must examine the phase function ϕ as it varies with spatial coordinates. If the phase ϕ depends solely on horizontal coordinates, for example $\phi = kx + ly$, where k and l represent the zonal and meridional angular wave numbers respectively, then the internal tide described by Eq. (2) corresponds to a horizontally propagating wave. In this case, the direction of propagation aligns with the horizontal wave vector (k, l). Conversely, if ϕ is a function only of the vertical coordinate, such as $\phi = mz$, with m being the vertical angular wave number, then the internal tide described by Eq. (2) represents a vertically propagating wave. This will be useful in the coming chapter.

---

[1] The coordinate transformation factor between z and z^* has a negligible impact (on the order of 10^{-9}) on the barotropic velocity component in our open-ocean study region. From this we deduce that it will not significantly affect the baroclinic velocity $\mathbf{u}'$, since the latter is obtained by subtracting the barotropic component from the full velocity. Hence, in the following analysis we disregard the term and perform all vertical integrations using the z coordinate.

2.2.2 *Internal Tide Kinetic Energy*

We quantify the strength of M2 internal tides in terms of the mean kinetic energy

$$E_{kin}(x, y, z) = \frac{A_u^2(x, y, z) + A_v^2(x, y, z)}{2}, \tag{4}$$

where A_u and A_v are, respectively, the amplitudes of the zonal and meridional internal tide velocity. They can be either the amplitudes of the full internal tide velocity given in Eq.(2), or the amplitudes of the internal tide velocity associated with the n-th mode described by the n-th EOF given in Eq.(14) in chapter 4. In the latter case, $E_{kin,n}$ indicates the strength of the n-th mode.

2.2.3 *Baroclinic energy flux at M2 frequency*

A fundamental quantity in internal wave energetics, which can help to identify energy sources and sinks as well as wave propagation, is the baroclinic energy flux $\mathbf{F}_E$. To compute the baroclinic energy fluxes $\mathbf{F}_E$

$$\mathbf{F}_E = < \mathbf{u}' p'_{bc} > \tag{5}$$

we use the monthly average of the product of baroclinic velocity $\mathbf{u}'$ (defined as in Eq. (1)) and the internal wave-induced baroclinic pressure perturbation p'_{bc} based on Li and Storch (2020). First we calculate density perturbation ρ' from the in-situ density ρ and its monthly average ρ_t

$$\rho'(x, y, z, t) = \rho(x, y, z, t) - \rho_t(x, y, z) \tag{6}$$

from which we obtain the pressure anomaly p' using the hydrostatic equation. The internal wave-induced baroclinic pressure perturbation is then given by

$$p'_{bc} = p' - \frac{1}{\eta + d} \int_d^\eta p' dz \quad . \tag{7}$$

We calculate the time-averaged baroclinic energy flux at M2 frequency using the amplitude and phase resulting from harmonic analysis by rewritting the harmonically analysed baroclinic pressure as in Eq. (2) with the corresponding amplitude $A_p(x, y,)$ and phase $\phi_p(x, y, z)$. Analytically computing the time integral for a tidal period, we obtain the following equation after some calculations

$$\mathbf{F}_{E,M2} = < \mathbf{u}'_{M2} p'_{M2} > = \tag{8}$$

$$= \frac{1}{2} A(x, y, z) A_p(x, y, z) (\cos(\phi(x, y, z) - \phi_p(x, y, z))). \tag{9}$$

Figure 4 shows the M2 internal tidal zonal energy flux u' globally, derived by Eq. (9) for the first month of our 5km ICON simulation. Contour lines indicate the bottom topography at around 2500m depth.

We identify several generation hotspots in the vicinity of rigdes and seamounts, which have also been observed using satellite altimetry eg. the Hawaiian ridge (Zhao et al., 2011), the Bay of Bengal (Wijesekera et al., 2019),

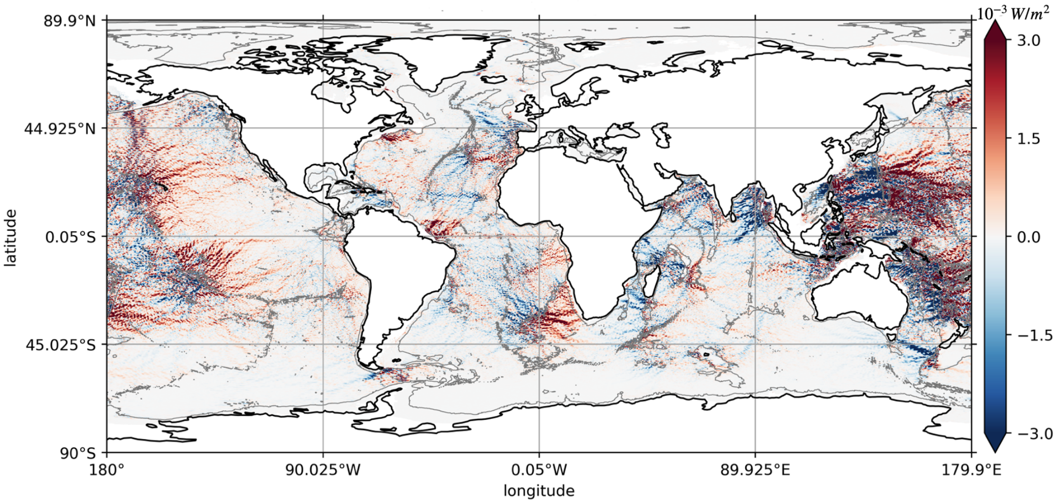

Figure 4: Global map of the internal tide zonal energy flux at M2 frequency averaged over the first month of our simulation (February 2022).

the Madagascar–Mascarene region with numerous generation sites (Zhao et al., 2016), the Midatlantic and Walvis ridges in the Atlantic (Zhao et al., 2016) and many more.

In figure 5 we show the examples of three regions with strong M2 internal tides resolved by our simulation: the Madagascar IT (a) which has been previously observed using moorings (Manders, Maas, and Gerkema, 2004) and satellite data (Wu et al., 2024), the Kuroshio IT (b), also observed by satellite (Zhao, 2014) and glider measurements (Rainville et al., 2013) and the Tasman tide (c) also observed in different studies (Johnston, Rudnick, and Kelly, 2015; Waterhouse et al., 2018).

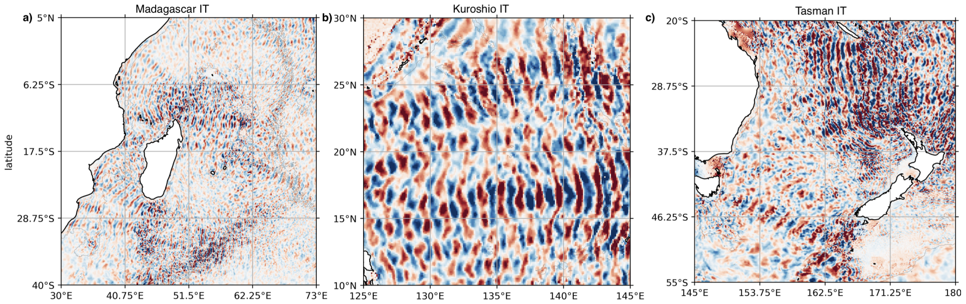

Figure 5: Zonal M2 internal tide velocity (m/s) in different regions worldwide resolved by our global model.

Seen from a global perspective, there is a small number of regions suitable for studying interactions between internal tides and eddies. These are some regions where mesoscale eddies and strong internal tides coexist. We focus on the southeast Atlantic where Agulhas Rings, shed by the retroflection of the Agulhas current, travel from the waters around the southern tip of the African continent northwestward and cross beams of internal tides -generated at and emitted from the Walvis Ridge. These beams have been identified both using semi-analytical solutions and numerical simulations (Garrett and Kunze, 2007; Nycander, 2005; Li and Storch, 2020).

For the following chapters of this thesis we will only consider the Walvis Ridge area. The focus region aligns closely with the study area of two concurrent observational campaigns conducted as part of the collaborative project CRC181.

2.3 THE AREA OF FOCUS: THE INTERNAL TIDE GENERATED AT THE WALVIS RIDGE AND ITS WAVE ENVIRONMENT

A typical situation in this region is depicted in figure 6. There are several beams of M2 internal tide (IT), indicated by the trains with positive (red) and negative (blue) internal tide zonal velocity, which radiate from the Walvis Ridge. Agulhas rings (indicated by the contours) propagate northwestward and cross the internal tide beams east of the ridge.

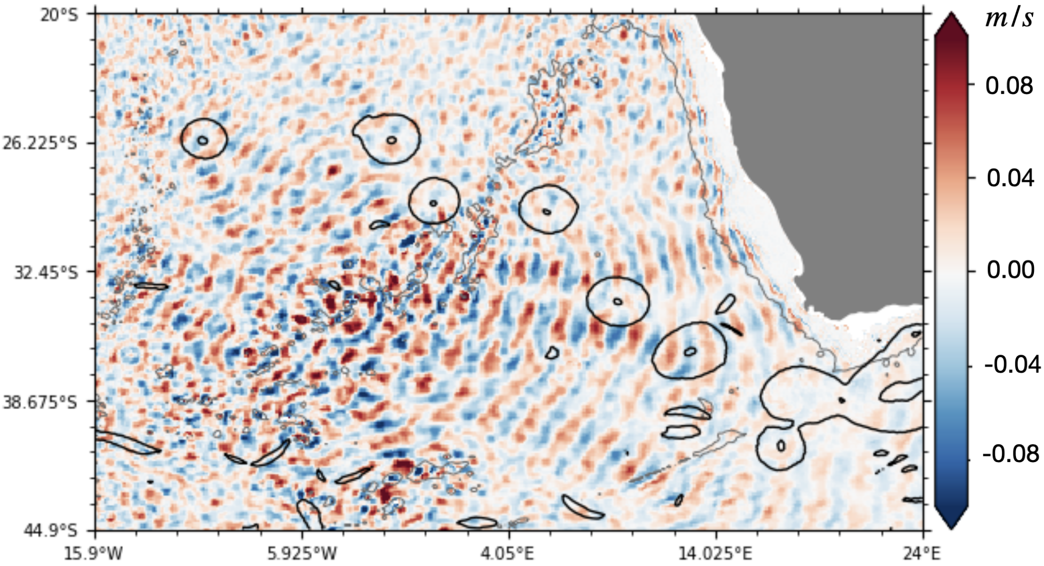

Figure 6: A snapshot of the M2 internal tide zonal velocity (colour shadings) at ca. 100m depth, together with topography (grey lines) and Agulhas Rings (black lines) simulated by ICON-O. The Agulhas Rings are described by the mean horizontal current speed.

Figure 6 shows u' at approximately 100 m depth obtained at one time instance. We observe the expected connection between strong internal tide and topography, here the Walvis Ridge, and the beam-like structures of the waves propagating away from it. The beams can be recognized by following the velocity maxima. The wave amplitudes are stronger when they are close to the generation site and weaken the further away they are, possibly due to dissipation or redistribution of the energy caused by non-parallel wavenumber vectors. In some areas along the continental coast we observe slightly stronger values, which can be caused by reflection at the coast and subsequent constructive interference between the incoming and the reflected beam. Furthermore, we observe that the horizontal wavelength of the waves is spatially varying and doesn't remain constant across the complete region of interest, thus the diagnosed internal tidal waves are not plane waves. The importance of this fact will be made clear in the next section.

2.3.1 *Mesoscale Agulhas Rings and Bathymetry*

This subsection describes the main features of the wave environment in our area of focus. These include the bathymetry shown in Figure 7, the mean circulation shown in Figure 8, and the mean stratification shown in Figure 10. Both the bathymetry and the mean circulation reveal strong and complex spatial dependence, with the latter being characterized by Agulhas rings aligning from the Agulhas retroflection toward the Walvis Ridge. Agulhas rings are some of the strongest mesoscale eddies globally (Laxenaire et al., 2018).

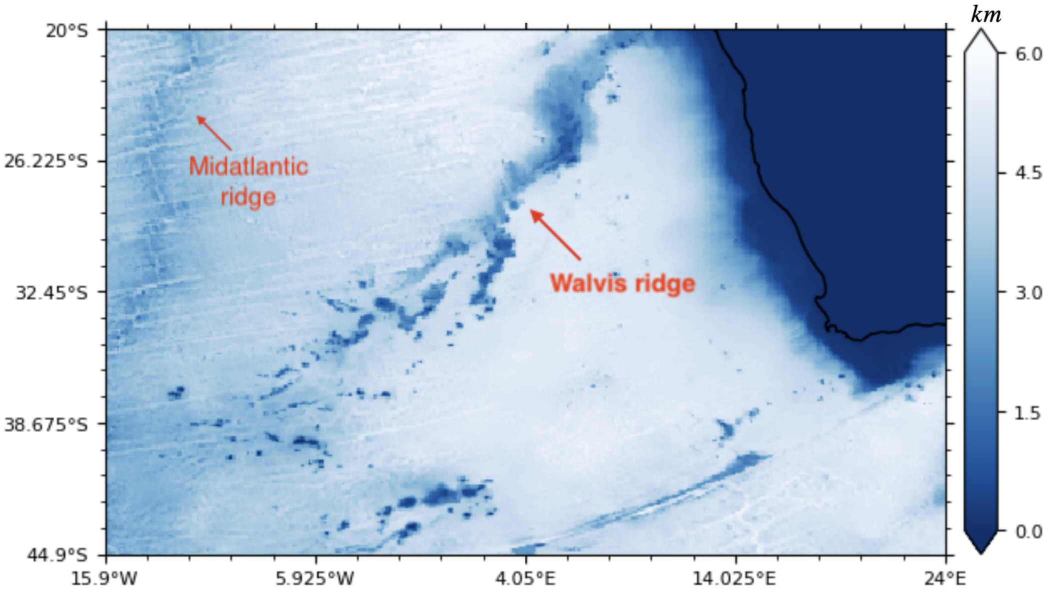

Figure 7: Bathymetry of the research area in the southeast Atlantic.

An Agulhas ring, as described by the composites in Figure 9, is characterized by a velocity minimum at the center of the ring. The mean radius of the rings is about 115 km. At 100 m depth, the maximum velocity reaches nearly 1 m/s at the northern rim of the rings. All simulated rings are anticyclonic, surface intensified, and essentially confined in the upper 500 m. Their propagation speed is roughly estimated to be 0.1 m/s.

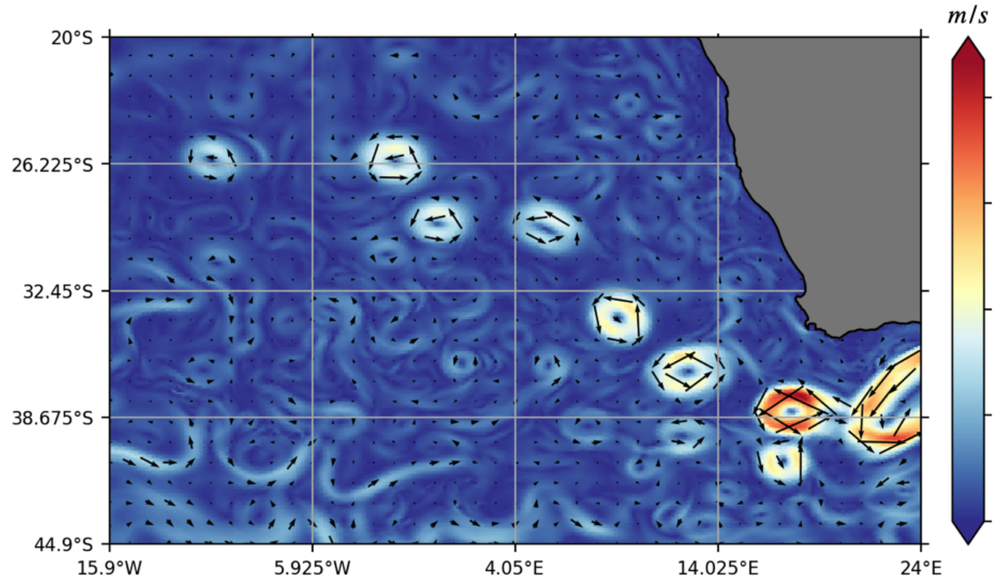

Figure 8: Mean horizontal current speed during late summer in February 2022 at about 50m depth.

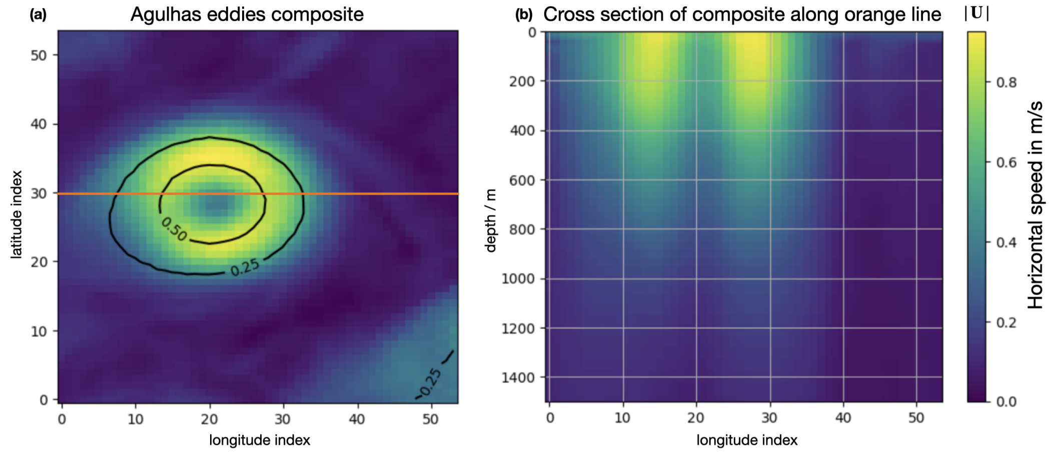

Figure 9: Composites of a) velocity speed at 100 m (color shadings) and sea surface height (black contours) and b) current velocity as a function of depth along the red line shown in a). The composites are obtained by averaging over the five largest Agulhas rings found in the 1.5 year simulation. Sea surface height is in m and horizontal velocity in m/s.

2.3.2 *Stratification*

We compute the time-averaged stratification N^2 for every month of each simulated season by first averaging the salinity $s(x, y, z)$ and temperature $T(x, y, z)$ fields in time, and then deriving the mean density $\rho_t(x, y, z)$. From this, we obtain the stratification at each grid point as

$$N^2 = \frac{g}{\rho_0} \frac{\partial}{\partial z} \rho_t(x, y, z) \tag{10}$$

with the gravitational acceleration g and the constant reference density ρ_0. By averaging s and T prior to computing N^2, rather than computing N^2 at each time step and then averaging, we effectively filter out high-frequency variability and emphasize the large-scale background stratification. This smoothed representation is more appropriate for characterizing the slowly varying wave-environment.

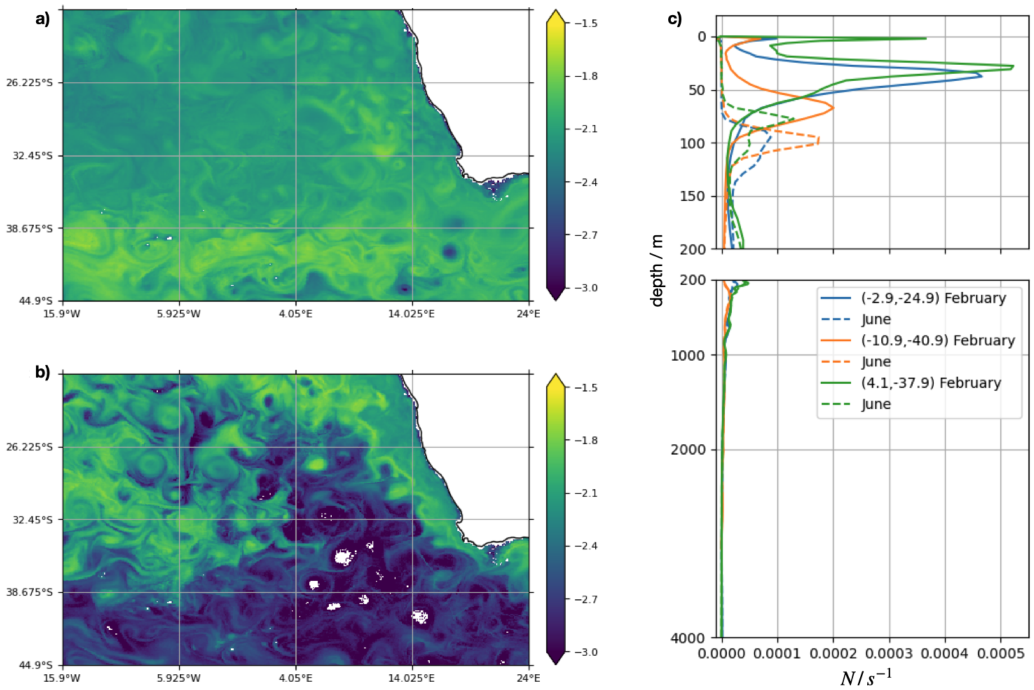

Figure 10: Mean stratification, as described by the Brunt-Väisäla frequency N in logarithmic scale ($\log_{10} N$) at about 70 m for a) February and b) June 2022, and as c) vertical profiles of N^2 at three grid points (x_0, y_0) for February (full lines) and June (dashed lines). N is derived from mean temperature T and salinity s in the respective month.

The mean stratification varies horizontally and vertically, introducing an additional complexity into the internal wave dynamics. These variations can influence the generation, propagation, energy dissipation of the waves, as well as the interaction of waves with the surrounding fluid medium, such as mesoscale and submesoscale flow features. Seasonal variations are also evident: we observe weaker stratification during winter in June-July 2022 than during late summer in Febuary-March 2022. In particular, N at about 70 m is about one order of magnitude weaker in winter than in summer in the southern part of the domain. In the vertical, the maximum of N is smaller and located deeper in winter than in summer. These patterns are consistent with seasonal cycles in surface forcing: stronger insolation and weaker winds in summer lead to enhanced surface stratification and a shallower mixed layer, whereas stronger mixing in winter deepens the pycnocline and reduces stratification near the surface.

In this chapter we introduced the model approach used in this thesis, explained the main methods we apply, described the focus area and the wave environment and presented the main characteristics of the M2 internal tide resolved by our model.

3

VERTICAL MODE DECOMPOSITION: A NOVEL DATA-DRIVEN METHOD AND COMPARISON TO LINEAR WAVE THEORY BASED METHODS

ABSTRACT

To assess the influence of Agulhas eddies on the propagation of the low-mode internal tide, it is essential to characterize the spatial properties of the wave in its complex environment both before and after the interaction. The widely used Sturm–Liouville (SL) decomposition provides local vertical modes derived from linear wave theory, but it has key limitations: it assumes linearity, neglects background currents, and does not provide coherent horizontal phase information across the domain. These limitations hinder its use in complex, eddy-rich environments. We introduce a novel decomposition method based on empirical orthogonal functions (EOF) to extract the internal tide modes from ICON simulations, without relying on the assumptions required by linear wave theory. Unlike SL modes, EOF modes are data-driven and defined for the full study area, enabling the reconstruction of fully three-dimensional, horizontally propagating internal tides with coherent vertical structures and spatially varying wavelengths. This approach inherently accounts for the influence on the internal tides not only of the bathymetry and stratification, but also of the mean currents resolved by our model. Furthermore, by comparing the result obtained from the standard method and our new method, the degree by which the non-linear interactions between the complex wave environment resolved by the model alter the structures of ITs can be assessed. In particular, in cases where the two methods produce comparable modes, this could indicate a minor role of mean flow in altering the wave structures. Where they differ, the discrepancies offer insight into how the mean flow reshapes the internal tide field beyond the scope of linear theory. With this, our method offers a powerful alternative for internal tide analysis in realistic simulations, particularly where standard modal approaches fall short.

3.1 INTRODUCTION

Recent advances in computational power and the development of increasingly sophisticated ocean models have significantly enhanced our ability to study small-scale oceanic processes under realistic conditions. However, while these complex simulations diverge from the idealized models that have long served as valuable research tools, the analytical methods commonly applied to both remain largely unchanged, even though the underlying assumptions of idealized and realistic models differ fundamentally. In this study, we focus on one such method: vertical mode decomposition, a widely used technique for examining how different oceanic processes affect wave dynamics across different spatial scales.

In existing literature the common approach used to decompose the internal tide into modes when studying the effects of mesoscale eddies on the different spatial scales of internal tidal waves using both in-situ observations (Löb et al., 2020; Huang et al., 2018) and idealized numerical models (Wang and Legg, 2023; Dunphy et al., 2017) is the standard modal decomposition method (Gill, 1982; D.Olbers, C.Eden, and J.Willebrand, 2012; Gerkema and Zimmerman, 2008). It is based on the Sturm-Liouville equation, which describes the vertical dependence of the linear wave solution.

However, almost a decade ago Dunphy et al. (2017) briefly discussed the challenges of the vertical mode representation based on the Sturm-Liouville equation, mainly focussing on the fact that using a reference stratification profile for a large domain (as in the approximate mode solution, discussed in section 3.4.2) may not be adequate, given the large dependence of internal tides on local changes of the density profile. For their study they chose to divide the domain into three smaller ones, each with a different stratification profile to better match the local stratification, satisfying the continuity conditions at the boundaries of each domain. However, they hint that this can also be hard to interpret and suggest to turn the focus into a direct analysis in the physical space. As we explain later, SL-based decomposition presents notable limitations, particularly when applied to realistic model data. It defines vertical modes locally, based on stratification at each grid point, making it difficult to track the evolution of a single mode across space. Moreover, while it separates vertical structures well, it does not provide direct information on horizontal propagation, such as directionality or phase coherence. For low modes, which can travel across ocean basins, this is a major shortcoming. Generally and especially for short waves, the wave phase ϕ may depend on both horizontal and vertical components, indicating oblique wave propagation. Long waves, such as those simulated by the primitive-equation ICON model, are well described by vertically standing waves. In this case, the part of ϕ that depends on z does not contributes to the complex wave form and can be absorbed in amplitude A. The first line of Eq.(2) reduces to $\mathbb{R}e\Big(A(x,y,z)e^{i(\omega t-\phi(x,y))}\Big)$, describing a horizontally propagating wave with either a fixed or spatially varying vertical structure. The horizontal propagation is in the direction of the horizontal wave number vector (k,l), which can be described by horizontal gradients of ϕ, with $k = \partial\phi/\partial x$ and $l = \partial\phi/\partial y$.

To assess how an Agulhas ring influences a propagating low-mode internal tide, it is essential to quantify the mode's 3-dimensional structures, both before and after the mode encountering an Agulhas ring. This calls for a decomposition method that not only identifies the vertical structure of a mode but also quantifies the horizontal dependence of the phase ϕ of the mode. Hence, we develop a new decomposition method, by which the structures of ITs are empirically extracted from the model output without imposing any assumptions needed to derive linear wave theory. We use EOFs to decompose the internal tide velocities along the vertical, which captures dominant vertical structures in a data-driven way. Unlike SL modes, EOF modes are computed over the complete study area, offering consistent vertical structures across space. This allows us to better characterize three-dimensional mode properties and later analyze how mesoscale features, like Agulhas rings, affect the propagation and transformation of internal tides.

Our EOF decomposition along the vertical could be one of those alternatives discussed by Dunphy et al. (2017), providing a more realistic and clearer picture of how internal waves interact with the ocean's large-scale flows.

This chapter is organised as follows: Section 3.2 explains the data used, 3.3 introduces our novel modal decomposition method based on EOF spatial analysis and presents the corresponding low- and high-mode waves, their vertical structures, wave properties etc. In section 3.4 we compare our results with the ones derived using the standard decomposition method. In 3.5 we provide a summary and discussion of the complete chapter.

3.2 MODEL DATA

For this chapter, in which we present a novel decomposition method and compare it on the one hand with the conventional method based on linear wave theory and on the other hand with a simplified and computationally less expensive alternative of the conventional one named the *approximate vertical modes*, we choose to use the model data from the first simulated month (February 2022) with hourly output data. The corresponding run is described in more detail in the next chapter.
The variables needed for the novel method are the phase $\phi(x, y, z)$ and amplitude $A(x, y, z)$ of the zonal and meridional M2 internal tide velocities resulting from harmonic analysis (see Eq. (2)). The conventional decomposition based on linear wave theory requires solving the Sturm-Liouville eigenvalue equation (see Eq. (19)) at each grid point using time-averaged stratification profiles, derived as in (10). The resulting eigenvectors are then projected onto the M2 internal tide velocities. Lastly, for the approximate vertical modes we use the temporal and horizontally averaged N profiles and project them onto the M2 velocities.

3.3 A NOVEL MODAL DECOMPOSITION METHOD BASED ON EMPIRICAL ORTHOGONAL FUNCTIONS

The new decomposition method is based on EOF analysis, a well-know method used to extract from high-dimensional data structures that maximize the total variance (Thomson and Emery, 2014; Storch and Zwiers, 1999). Different from the usual practice, which considers the variance with respect to time and a covariance matrix describing the spatial covariability averaged over time, we consider the variance with respect to depth and a covariance matrix that describes horizontal covariability averaged over depth. To avoid the land points associated with topographic features in the deep ocean, only data in the upper ~ 4000 m are used. The EOFs e_n with $n = 1, ...,$ are eigenvectors of the covariance matrix. They have the property that the first EOF e_1 captures the largest portion, and the second EOF e_2 the second largest portion of the variance with respect to depth, and so on. The corresponding principle components PCs α_n are functions of the depth z.

To take both the amplitude and phase information in u' into account, the covariance matrix is derived from a data vector composed of $C(x, y, z)$ and $S(x, y, z)$ given in Eq.(2). The resulting n-th EOF e_n is composed of the same two parts, denoted by e_n^c and the second one by e_n^s respectively.

$$e_n(x,y) = \begin{pmatrix} e_n^c(x,y) \\ e_n^s(x,y) \end{pmatrix}. \tag{11}$$

The corresponding principle component α_n is obtained by projecting the vector consisting of $C(x,y,z)$ and $S(x,y,z)$ onto $e_n(x,y)$

$$\alpha_n(z) = \nu \sum_{x,y} \Big(e_n^c(x,y)C(x,y,z) + e_n^s(x,y)S(x,y,z)) \Big), \tag{12}$$

where $\sum_{x,y}$ indicates the summation over all grid points (x,y). The proportionality factor ν is chosen such that α_n is normalized to one so that e_n has the physical unit of u'.

The internal tide velocity reconstructed using the n-th EOF is given by

$$u_n'(x,y,z,t) = \alpha_n(z)\Big(e_n^c(x,y)\cos(\omega t) + e_n^s(x,y)\sin(\omega t) \Big). \tag{13}$$

The decomposed and reconstructed u_n' has an amplitude A_n

$$A_n(x,y,z) = \alpha_n(z)\sqrt{\big(e_n^c(x,y)\big)^2 + \big(e_n^s(x,y)\big)^2}, \tag{14}$$

and a phase ϕ_n

$$\phi_n(x,y) = \arccos\left(\frac{e_n^c(x,y)}{\sqrt{\big(e_n^c(x,y)\big)^2 + \big(e_n^s(x,y)\big)^2}} \right). \tag{15}$$

By Taylor expanding ϕ_n and retaining only the leading term, we find

$$\phi(x,y) = \frac{\partial \phi_n}{\partial x}x + \frac{\partial \phi_n}{\partial y}y + \cdots \simeq k_n x + l_n y, \tag{16}$$

with

$$k_n = \frac{\partial \phi_n}{\partial x}, \quad l_n = \frac{\partial \phi_n}{\partial y}. \tag{17}$$

We define the wavelength λ_n associated with the n-th EOF $e_n(x,y)$ as

$$\lambda_n = \frac{2\pi}{K_n}, \quad \text{with } K_n^2 = k_n^2 + l_n^2. \tag{18}$$

An EOF analysis is designed to extract a horizontal structure (described by $e_n(x,y)$) that is optimally associated with the corresponding PC $\alpha_n(z)$. e_n^c and e_n^s are functions of horizontal coordinates x and y. e_n^c and e_n^s contain spatial dependence as simulated by the non-linear ICON-O without involving any additional assumptions. So far, it is not clear whether the wave properties described by u' in Eq.(2) prior the EOF analysis can be retained after the EOF analysis. We show below that this is the case.

One important property of internal-tide velocity is that it describes horizontally propagating wave structures. This means that internal-tide velocity u' at one time must be 90°-out-of-phase with u' a quarter of period later. Fig.11 shows that for both the full internal-tide velocity u' described by Eq.(2) and the velocity reconstructed using EOF1 according to Eq.(13), the zero lines of wave patterns one quarter of period earlier (thick black lines) are located at the wave maxima (colors) one quarter of period later. A similar picture is obtained for the meridional velocity (not shown here). Thus, the horizontal propagation is well retained by the EOF analysis. Another important property of long gravity wave is described by the polarisation relation that zonal velocity must be 90°-out-of-phase with meridional velocity. Fig.12 shows that this property is also retained by the EOF analysis.

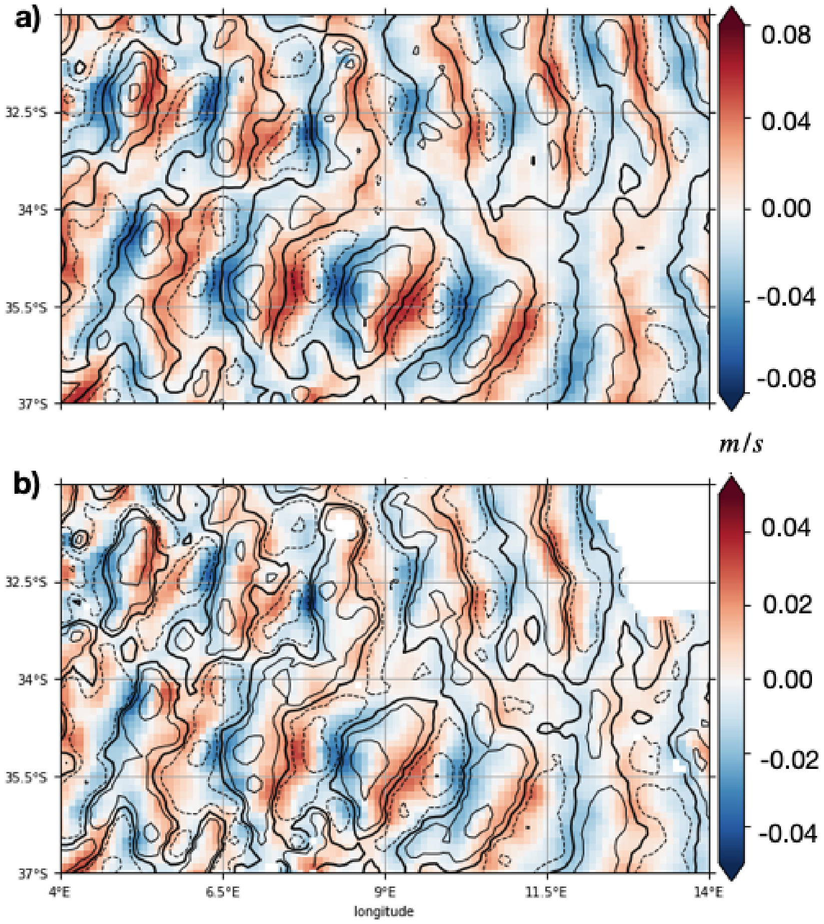

Figure 11: A snapshot of M2 internal-tide zonal velocity at time $t = t_0$ (contour lines) and a quarter of time period later (color shadings), a) as given in Eq.(2) and b) as reconstructed using EOF1 according to Eq.(13). The unit is m/s.

Thus, internal-tide velocities reconstructed using EOFs according to Eq.(13) represent horizontally propagating waves, whose vertical structure is fixed and whose horizontal wavenumber (k, l) is allowed to vary during the propagation. The variation of (k, l) results from the EOF phase given in Eq.(15) and can be interpreted as resulting from horizontal variations of the wave environment.

This simple interpretation is in striking contrast with a mode obtained from the

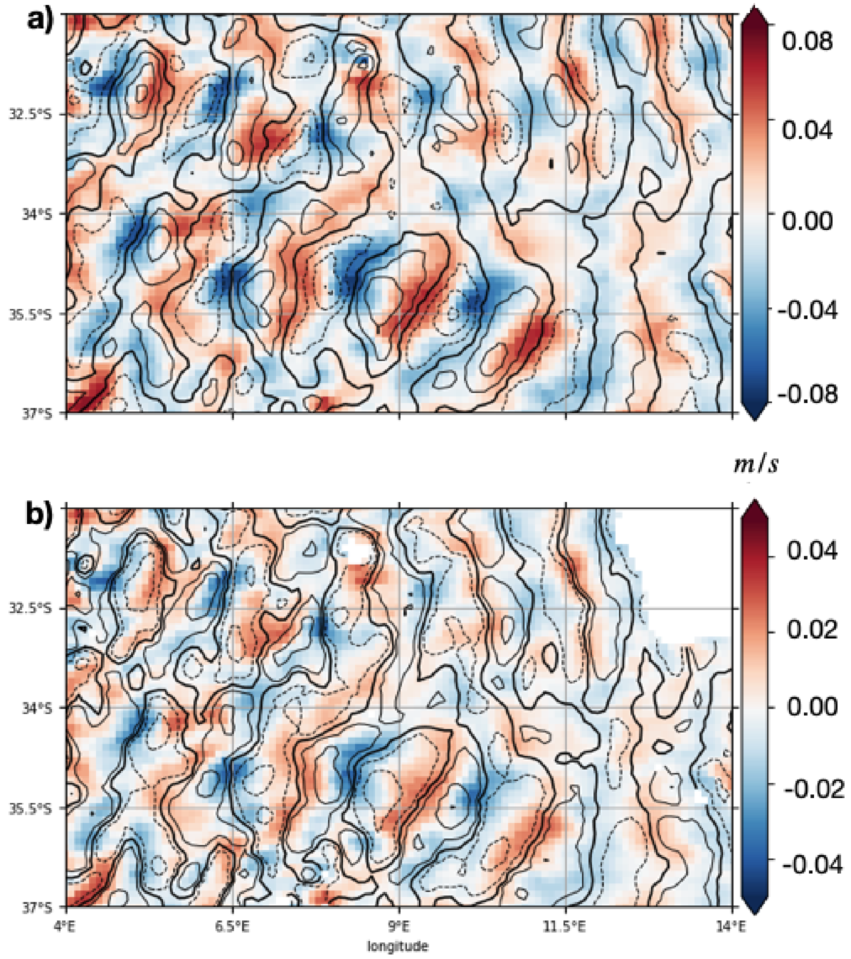

Figure 12: A snapshot of the internal-tide zonal (color shadings) and meridional velocities (contour lines) at the same timestep, a) as given in form of Eq.(2) and b) as reconstructed using EOF1 according to Eq.(13). The unit is m/s.

standard modal decomposition method, which consists of horizontally independent local plane waves. We do not claim that our EOF method is the most appropriate way to do the modal decomposition. Instead, we consider our method as being capable of capturing features that are more physically sound and more easily interpretable than those captured by the standard decomposition based on linear wave theory, since it directly extract the IT horizontal structure resulting from the spatially varying wave environment without including any assumptions on the structure of the IT waves.

3.3.1 *EOF modes of the M2 Internal Tide in the Walvis Region*

Following the modal decomposition based on spatial EOF analysis, the n-th mode is a standing wave that propagates horizontally with a horizontal structure determined by the n-th EOF $e_n(x, y)$ and a vertical structure determined by the corresponding principal component (PC) $\alpha_n(z)$. Two EOFs $e_1(x, y)$ and $e_5(x, y)$ are shown in Fig.13. The corresponding PCs, α_1 and α_5, together with α_3 and α_9 are shown in Fig.14. For the n-th PC, we observe n zero-crossings in the vertical. This corresponds to a decrease in vertical scale with increasing number of mode. The low-order EOFs represent hence low modes with larger vertical scales; and the high-order EOFs represent high modes with smaller vertical scales. The variances captured by the first 5 EOFs are listed in Tab.1. We find that the first EOF explains 74.4%, and the first 5 EOFs explain together 99.1% of the total variance. A similar result is found for the meridional internal-tide velocity. Thus, the M2 internal tide simulated by ICON-O is dominated by the lowest modes described by the leading EOFs.

EOF number	1	2	3	4	5
variance (%)	74.4	17.2	5.1	1.7	0.7
accumulated variance (%)	74.4	91.7	96.7	98.4	99.1

Table 1: Variance (second row) explained by and the accumulated variance (third row) explained up to the n-th EOF, with $n = 1, \cdots, 5$.

The horizontal structure of the low modes differ strongly from those of the high modes. As can be seen from Fig.13, both EOF1 and EOF5 reveal wave-like patterns that radiate away from the Walvis Ridge and are characterized by alternating positive and negative velocities. However, the wave structures associated with EOF1 have much larger scales than those associated with EOF5. Moreover, while the waves related to EOF1 can propagate over a distance of about 1000 km and reach the African continent, the waves related to EOF5 are only visible in the immediate proximity of the Walvis ridge and in several circular patches southeast of the ridge. It appears that ICON-O can simulate high-mode internal tides, but the horizontal propagation of these high modes is more strongly dissipated than that of the low modes. To what extent such a strong dissipation is realistic is unclear at this moment. Finally, further away from the Walvis ridge, the velocities associated with EOF5 tend to cluster into circular patches, a feature completely absent in EOF1. This relation between horizontal and vertical structures is in general consistent with internal gravity waves (Gerkema and Zimmerman, 2008). We will come back to the high-mode horizontal structures in the next chapter.

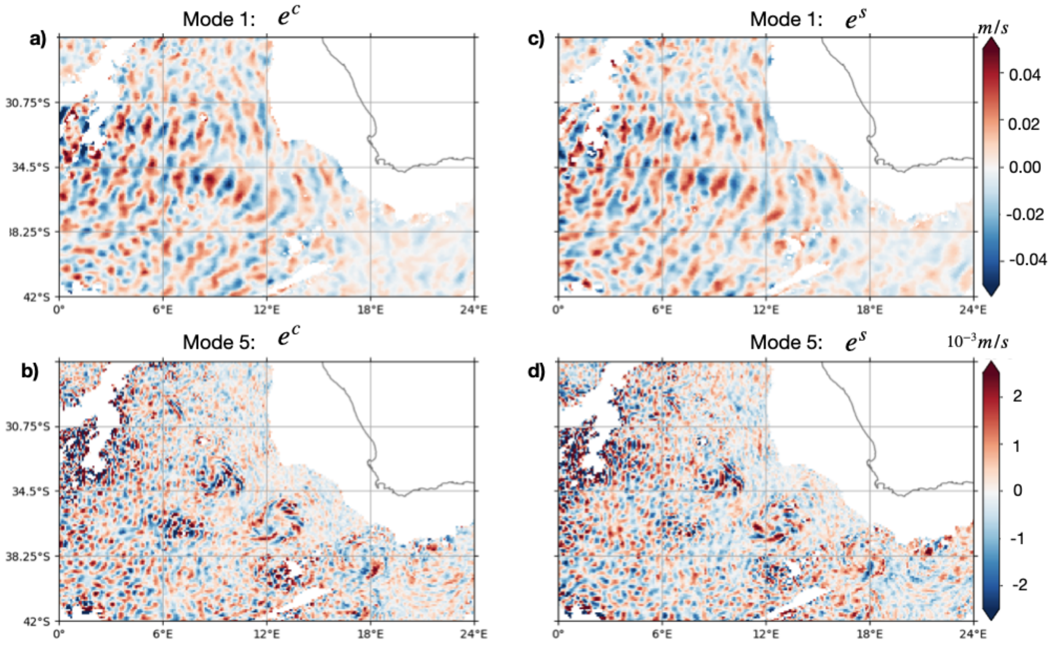

Figure 13: The two parts of the EOF decomposed data, e_n^c (left) and e_n^s (right), of EOF1 (top) and EOF5 (bottom), obtained by applying the EOF analysis to detrended internal-tide zonal velocity above 4000 m.

To quantify the horizontal scales of the modes, we estimate the wavelength λ_n according to Eq.(17) and Eq.(18). We consider area-averages of λ_n over a smaller area, rather than grid-point values of λ_n. Due to the strong spatial inhomogeneity of high modes, seen eg. for EOF5 in Fig. 13b and d, characterized by extremely small values outside circular patches relative to those inside the patches, we select the area to be comparable to one of those patches (see black box in Fig. 23). As will be discussed later, these patches are related to Agulhas rings. Due to the very weak signals outside these patches and hence the stronger horizontal gradients of the phase ϕ_n near the rim of the patches, calculating the wavelengths over the complete study area would introduce too many non-physical values. The resulting mean horizontal wavelengths per mode are shown in figure 25. In fact, we find that the mean horizontal wavelengths of our first five EOF modes, scaling from 137km for mode 1 to 60km for mode 5, are comparable to those obtained by solving the Sturm-Liouvile equation for conditions simulated by the HYCOM model with a comparable horizontal resolution of 4 km (Buijsman et al., 2020).

It remains unclear whether and to what extent the results of our EOF-based decomposition method, which take into account the full complex wave environment, compare well to the ones based on the standard decomposition method, which includes many additional assumptions, as explained in the introduction. We perform this comparison in the next section.

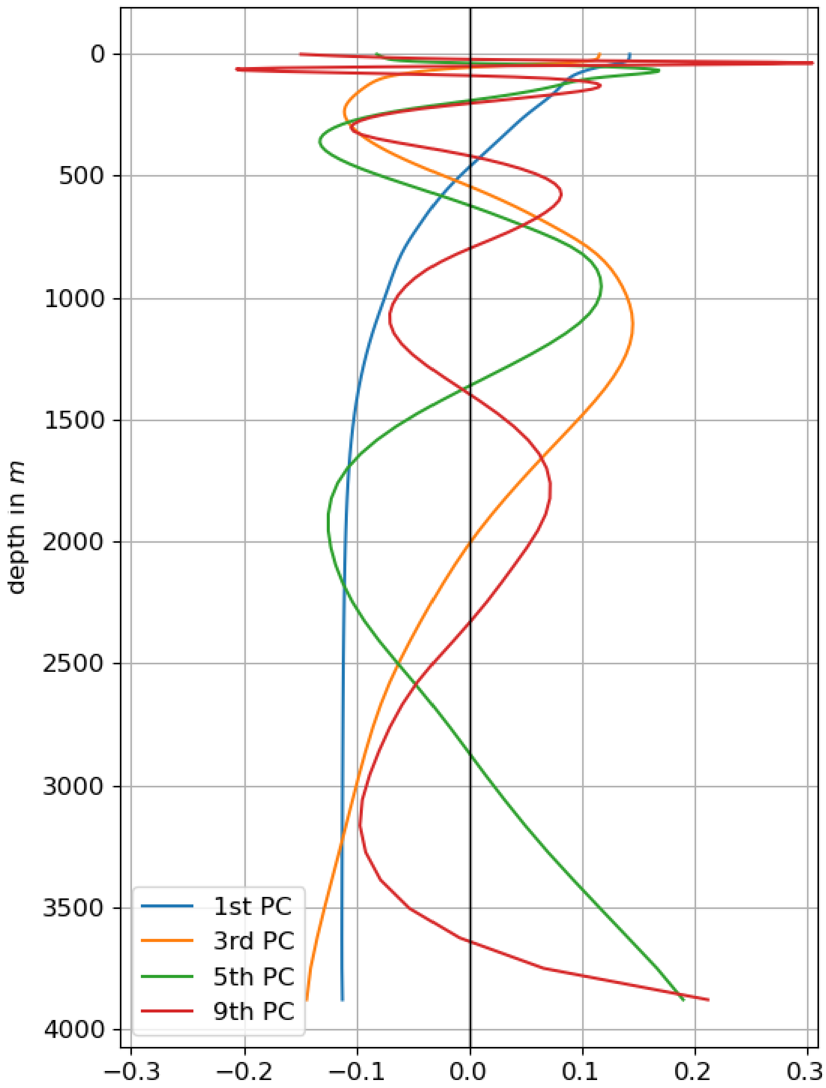

Figure 14: Principal components (PCs) α_n, for $n = 1, 3, 5, 9$, obtained by applying the EOF analysis to detrended internal-tide zonal velocity above 4000 m.

3.4 THE STURM-LIOUVILLE MODAL DECOMPOSITION METHOD

In this section, we compare our EOF modes with modes based on linear wave theory. These can be derived either as exact solutions of the Sturm-Liouville equation or as approximated solutions.

We derive the exact eigenvectors of Sturm-Liouville equation using the stratification at each grid point, as it has been done e.g. by Buijsman et al. (2020). This exact solution is presented in 3.4.1. Additionally, to enhance the compatibility with our method, we consider an alternative solution of the Sturm-Liouville equation using approximated eigenvectors. These are obtained using an area-averaged stratification, following Eden and Olbers (2017) (their Appendix B). This approximate solution is presented in 3.4.2

The standard method for modal decomposition is based on the linear wave theory, which describes the vertical structure of linear internal wave solutions in terms of eigenfunctions of the Sturm-Liouville (SL) equation

$$\frac{d}{dz}\Big(\frac{1}{N^2(z)}\frac{d}{dz}a(z)\Big) = \chi\, a(z)\,, \tag{19}$$

with the local stratification profile and water depth, yielding a discrete set of eigenfunctions $a_n(z)$ and associated eigenvalues χ_n.

3.4.1 *The exact solution*

To obtain the exact solutions of the SL eigenvalue problem, at each horizontal grid point (x_0, y_0) Eq. (19) is solved using the local stratification profile and water depth, yielding a discrete set of eigenfunctions $a_n(z)$ and associated eigenvalues χ_n. We use the time-averaged stratification profiles at each grid point to compute the normal modes, which we then normalize and project onto the internal tide zonal (meridional) velocity u' (v') to obtain the corresponding modal velocities. In this case we obtain 128 vertical modes, similar to the amount of vertical levels in our model. Due to the limitations of the horizontal resolution, we focus on the first ten for the analysis. A modal decomposition is then performed by projecting the internal tide velocity u', or its time-independent components C and S, onto these vertical eigenfunctions. The projection of u' onto the n-th eigenfunction $a_n(z)$ defines the velocity field of the n-th mode:

$$u'_n(x,y,z,t) = a_n(z)\, \beta_n(x,y,t), \tag{20}$$

where the modal amplitude β_n is a time series given by:

$$\beta_n(x,y,t) = \sum_z a_n(z) u'(x,y,z,t). \tag{21}$$

By collecting β_n across all horizontal locations, one can reconstruct the full three-dimensional structure of the n-th mode over the analysis domain.

Alternatively, the n-th mode can be represented using the modal components c_n and s_n of C and S respectively as

$$u'_n(z, x_0, y_0, t) = a_n(z)\, [c_n(x_0, y_0)\cos(\omega t) + s_n(x_0, y_0)\sin(\omega t)]\,, \tag{22}$$

with time-independent modal coefficients

$$c_n(x_0, y_0) = \sum_z a_n(z) C(x_0, y_0, z), \quad s_n(x_0, y_0) = \sum_z a_n(z) S(x_0, y_0, z). \tag{23}$$

While Eq.(20) and Eq. (22) are formally equivalent, an IT is reconstructed using time-independent coefficients c_n and s_n Eq.(22), but using a time series β in Eq.(20).

At first glance, Eq.(22) suggests that each mode may represent a horizontally propagating wave with a well-defined vertical structure. However, neither Eq.(20) nor Eq.(22) provide direct information about the mode's horizontal propagation. Being calculated using local stratification and local depth, the n-th eigenfunction

$a_n(z)$ vary from grid point to grid point. While this variation may reflect topographically induced horizontal variations in vertical structure, it complicates the interpretation of low modes. A low mode propagates over thousands of kilometers. Characterizing its 3-dimensional properties requires identifying its vertical structure at all grid points along its propagation path, which is highly impractical.

Regarding horizontal propagation, the linear dispersion relation:

$$k^2 + l^2 = \chi_n(\omega^2 - f^2), \tag{24}$$

relates the magnitude of the horizontal wavenumber vector (k, l) to the vertical eigenvalue χ_n, tidal frequency ω, and Coriolis parameter f. However, this relation only constrains the magnitude, not the individual components, of the horizontal wavenumber vector, and thus offers no insight into the direction of wave propagation.

An intuitive attempt to extract phase information is to rewrite Eq. (22) as:

$$u'_n(z, x_0, y_0, t) = a_n(z)\beta\left[\cos(\phi)\cos(\omega t) + \sin(\phi)\sin(\omega t)\right], \tag{25}$$

where $\beta = \sqrt{c_n^2 + s_n^2}$ and $\phi = \arccos(c_n/\beta)$. Assuming a plane wave form for the phase, such as $\phi = kx + ly$, one might estimate k and l by taking horizontal derivatives of ϕ. While such gradients can formally be computed, they are not physically meaningful, since ϕ lacks spatial coherence due to the independence between solutions of Sturm–Liouville equations at different grid points.

horizontal structures and scales

Figure 15 shows the mode 1 zonal velocity of the M2 internal tide derived using the EOF decomposition (a) and the exact solution of the SL decomposition (b). The horizontal structures of the zonal velocities as well as their magnitudes compare well. We also note that the wave properties discussed for the lowest EOF mode are also well represented by the lowest SL mode.

Figure 16 represents the 5th mode derived by the EOF (a) and exact SL (b) decomposition method. The main features of the high EOF modes are also revealed by the high SL modes. In particular, we observe again the presence of strong high-mode signals in the vicinity of the Walvis rigde and inside circular patches southeast of the ridge.

Deriving the horizontal wavelength of the SL modes from the dispersion relation (24) and computing the horizontal mean for the same area as previously discussed, we find that the SL wavelength clearly decreases with increasing mode number, similar to the EOF wavelengths. Additionally, we observe that the SL wavelength of 182km is about 40km (~ 25%) larger than that of the EOF mode 1. For all higher modes, the SL wavelengths are up to 40km shorter than the respective EOF wavelengths, with the shortening reaching about 35% for mode 9. We interpret this as a weakness of the SL method. Even though the decrease is consistent with the linear theory, quite a few assumptions must be made so that the eigenvalues, and with that the wavelengths, depend only on the local stratification and water depth. In contrast, the EOF decomposition captures the wavelength produced by the non-linear ICON model. We hence interpret the difference in the horizontal wavelength as reflecting the non-linear effects, which is ignored when applying the SL decomposition. Further investigation is needed to identify these non-linear effects.

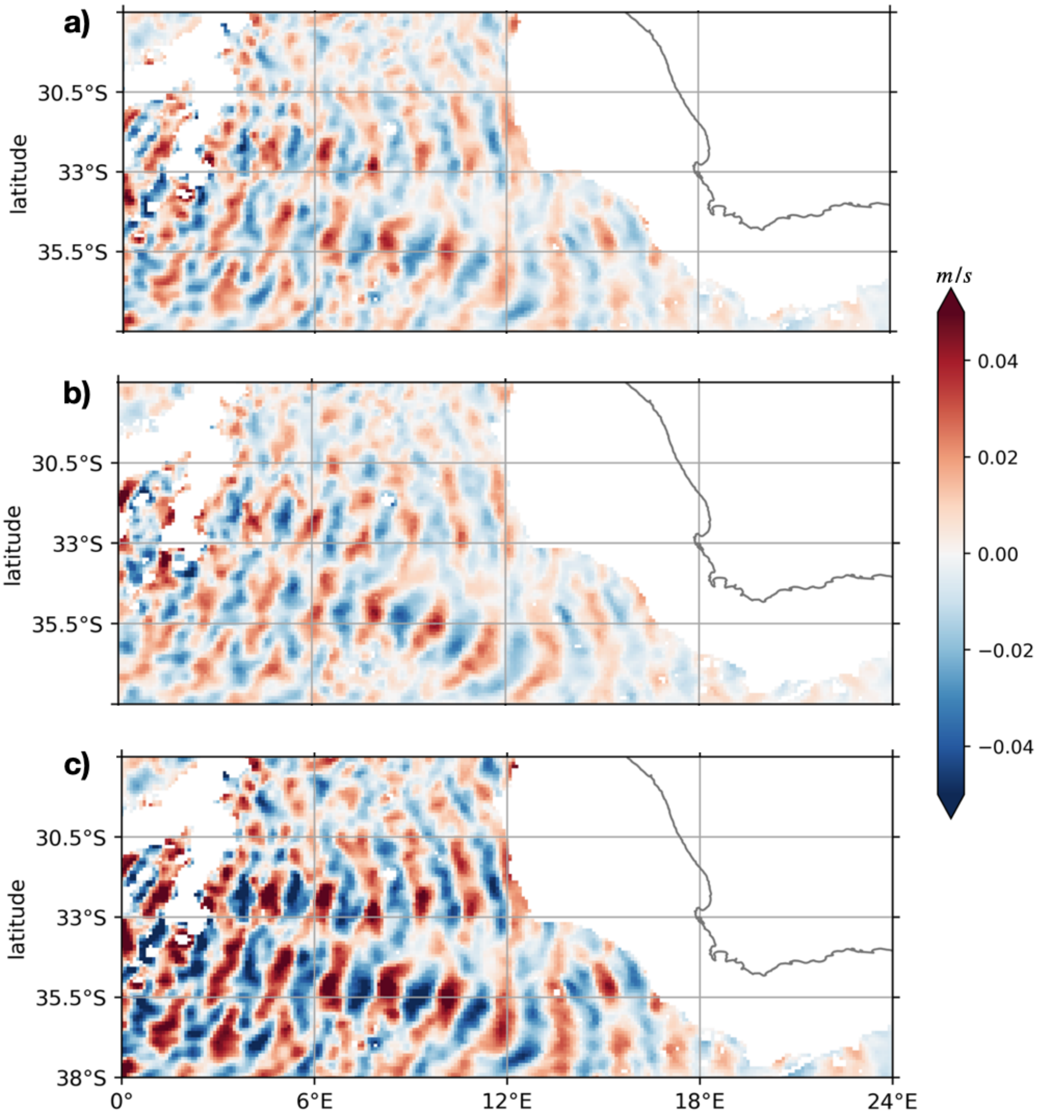

Figure 15: Mode 1 of the M2 zonal velocity using the a) EOF decomposition method, b) the exact solution of the SL decomposition method and c) the approximate solution of the SL decomposition method.

vertical structures and scales

The vertical structures (eigenvectors) of the SL modes are shown in Fig.17a, both in terms of an area-averaged eigenvectors (solid lines) and in terms of eigenvectors at three different grid points (dotted lines). We see that for mode 1, the vertical structure does not change much from grid-point to grid-point. Both the area-averaged (blue solid) and grid-point (blue dotted) eigenvector compare well with PC1 (blue dashed). Thus, mode 1 can be equally well identified by the SL and EOF decomposition as a horizontally propagating wave with a fixed vertical structure.
The situation is different for higher modes, as illustrated by the green lines for mode 5. The eigenvector changes from grid point to grid point (green dotted lines), and deviates clearly from the area-averaged eigenvector (green solid) as well as from PC5 (green dashed).

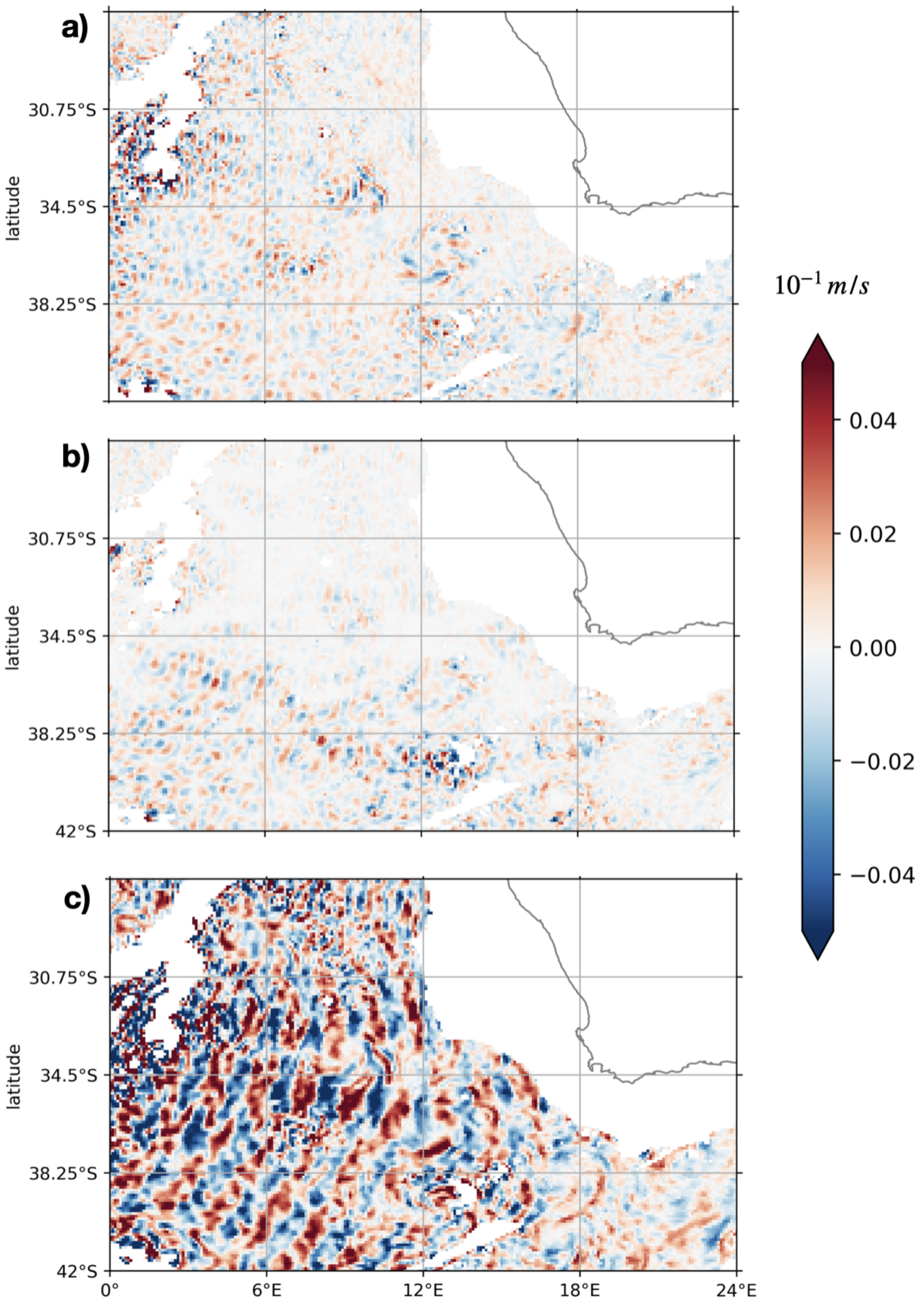

Figure 16: Mode 5 of the M2 zonal velocity using the a) EOF decomposition method, b) the exact solution of the SL decomposition method and c) the approximate solution of the SL decomposition method.

This variability implies a variability in the corresponding eigenvalue, and via dispersion relation, a variability in the horizontal wavelength. It appears that for a higher-order SL mode, both the horizontal wavelength and the vertical scale vary from grid point to grid point. Given that the SL modes cannot reflect the constraint on horizontal wavelength set by the model resolution, it is not clear which one of the two decomposition methods produces more realistic vertical structures. Further investigation is required to clarify this issue.

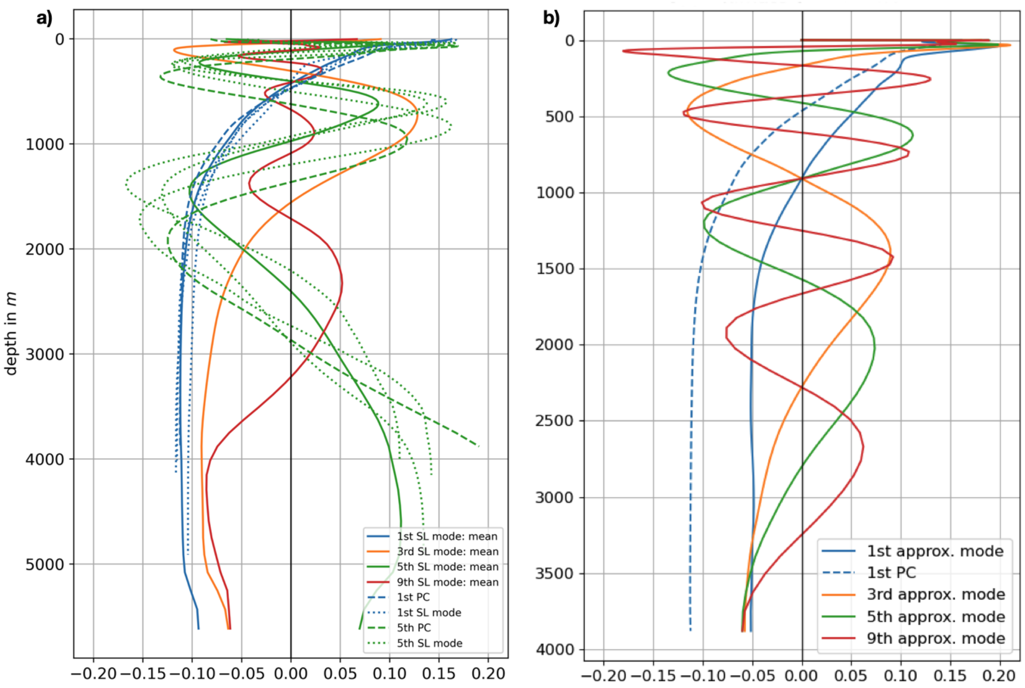

Figure 17: Eigenvectors of the Sturm-Liouville equation: a) for the exact solution and b) for the approximate solution. In a) solid lines are exact eigenvectors horizontally averaged over the study area, dotted lines indicate the first and the fifth eigenvector at three locations, and dashed lines indicate the first and fifth PC from the EOF decomposition method. In b) solid lines are the approximate eigenvectors and the dashed blue line is the first PC.

3.4.2 *The approximate vertical modes*

To enhance the compatibility to our method, we consider approximated eigenvectors of the Sturm-Liouville equation obtained using an area-averaged stratification, following Eden and Olbers (2017) (their Appendix B). The approximated n-th eigenvector is calculated as

$$a_{n,\mathrm{approx}}(z) = \sqrt{\frac{2N}{h\bar{N}}}\cos\left(\int_{-h}^{z} dz' n\pi \frac{N(z')}{h\bar{N}}\right) \tag{26}$$

with h being the total water depth, N being horizontally averaged over the study area, and

$$\bar{N} = \int_{d}^{h} dz\, N(z). \tag{27}$$

Here we also choose a fixed water depth of ~ 4000m, similar to the EOF method. Projecting the 3-dimensional internal tide velocity, i.e. $C(x, y, z)$ and $S(x, y, z)$ given in Eq.(2), onto $a_{n,\mathrm{approx}}(z)$, we obtain the corresponding horizontal structures for the n-th mode. Such a mode propagates horizontally with the same vertical structure, similar to our EOF modes.

horizontal structures and scales

The horizontal structures of zonal velocity obtained by projecting onto $a_{1,\mathrm{approx}}$ (Fig.15c) compares well with those described by EOF1 $e_1(x, y)$ (Fig.15a), both with respect to the horizontal wavelength and with respect to the positions of the IT beams. The main difference between the horizontal structures of mode 1 is that the former has slightly stronger magnitude than the latter.

However, higher modes, such as mode 5, appear to be incorrectly decomposed, as seen in Fig.16c. A significant portion of the low-mode energy is still projected onto the higher modes, resulting in unrealistic imprints of the low-mode beams in the high-mode structures. This is probably because the full three-dimensional and horizontally varying M2 velocity field used for the projection mostly contains mode 1 energy, which leads to energy leakage to higher modes. When projecting the three-dimensional data at one grid point onto $a_{n,\mathrm{approx}}$ with $n > 1$, the structure of mode 1, which is the dominant signal in the data, leaks into the n-th mode. The circular patches found in the high EOF modes can no longer be clearly identified using the approximated eigenvectors.

This is likely a consequence of the fact that $a_{n,\mathrm{approx}}$ satisfies an orthogonality condition with respect to area-averaged N, which differs from the exact eigenvectors a_n that satisfy an orthogonality condition at each grid point. This problem does not show up in the EOF analysis. An EOF analysis requires that the eigenvectors $e_n(x, y)$, which describe the horizontal structures, are orthogonal to each other, and derives the PCs $\alpha_n(z)$ by projecting 3-dimensional data onto EOFs $e_n(x, y)$.

vertical structures and scales

In general, the vertical structures of $a_{n,\mathrm{approx}}(z)$ (Fig.17b) are comparable to those of the PCs $\alpha_n(z)$ (Fig.14). In both cases, the n-th mode has n zero-crossings. A closer comparison reveals that the positions of zero-crossings in $a_{n,\mathrm{approx}}(z)$ differ from those in $a_{n,\mathrm{approx}}(z)$. For instance the zero-crossing in $a_{1,\mathrm{approx}}(z)$ (blue line in Fig.17b) is located about 500m deeper than that in $\alpha_1(z)$ (blue dashed in Fig.17b). Also, the magnitudes in the deep ocean are larger for $\alpha_n(z)$ than for $a_{n,\mathrm{approx}}(z)$, likely because $\alpha_n(z)$ are derived from vertically detrended data. Hence, even though the reconstructed IT based on the approximate vertical mode decomposition fits ours in terms of structure, we conclude that this method is not appropriate to study eddy-IT interactions, since it oversimplifies the background of the interaction by using a vertically smooth and horizontally non-varying stratification and lacks the ability to correctly decompose higher modes.

3.5 SUMMARY AND DISCUSSION OF CHAPTER 3

In this chapter, we recognized the unsuitability of the widely used decomposition method based on linear wave theory to study the impact of eddies on different modes of the diagnosed internal tides. This motivated us to develop a novel modal decomposition method based on spatial EOF analysis, a data-driven method which does not rely on any assumptions of the linear wave theory. Here, we present a summary of the key results and the conclusions derived from them.

First, the new method directly extracts the horizontal structure of internal tides from the model simulation without involving any wave assumptions. The resulting modes satisfy the polarisation relation and represent waves that propagate horizontally with a fixed vertical structure but a varying horizontal wavelength. The vertical structure of the n-th mode is characterized by n zero-crossings. The variation of horizontal wavelength is interpreted as a response of an internal tide to spatially varying wave environment. The modes identified by our method are dominated by mode 1, which alone explains over 70% of the total variance and has the form of wave beams that radiate from the Walvis Ridge. Both low and high modes are present in our focus area. However, while mode 1 can propagate over about 1000 km, high modes are quickly damped and have only large magnitudes in the immediate proximity of the ridge. The EOF modes have a mean wavelength that decreases with increasing mode number from around 150 km for mode 1 to about 60 km for mode 9. The decrease is strongest for low mode numbers. For mode number larger than 5, the decrease is hardly noticeable, possibly due to the fact that the model resolution is not sufficient to fully resolve the high modes.

Then, we compared our results with the ones obtained by both the exact and an approximate solution of the SL equation. A mode obtained by exactly solving the SL equation at every grid point consists of independent local plane waves. The three-dimensional structure of a SL mode is obtained by combining the solutions at all grid points, albeit the SL equation does not provide any information about how the results at different grid points are linked to each other. The EOF method however, extracts the spatial structure of IT directly from model simulations without relying on the assumptions needed for deriving the SL equation.

An EOF mode represents horizontally propagating waves that has a fixed vertical structure but varying horizontal wavelength.

Alternatively, we also looked at the approximate modes obtained using area-averaged stratification for the whole study area. Such a mode has a fixed horizontal wavenumber vector and a fixed vertical structure and can be more easily interpreted as a horizontally propagating plane wave. The wavenumber vector can be considered as representative for the averaged stratification. However, we found that the method tends to produce high modes that are contaminated by the low mode signals, which makes it not appropriate to study eddy-IT interactions.

Comparing the EOF modes with the SL modes reveals both similarities and differences. Regarding the wave properties, two differences stand out. First, the wavelength of SL mode 1 is longer and those of higher SL modes shorter than the corresponding EOF modes. The difference can be as large as 25 to 35%. Secondly, the SL high modes have vertical structures that vary strongly from grid point to grid point, whereas all EOF modes have a fixed vertical structure by construction.

To conclude, we consider our EOF method as a novel approach that captures not only the key features regarding the scales (i.e. horizontal wavelength and number of zero-crossings in the vertical), but also extracts propagating properties as simulated by the model without involving any wave assumptions. By doing so, our method is automatically taking the spatially varying wave environment into account. With this, our method overcomes some of the problems of the modal decomposition method based on linear wave theory. Additionally, the EOF method is computationally less demanding than the SL method. Here we'd like to note that the SL decomposition method can still be a very usefull and probably the most adequate tool to study such interactions in observational data, which usually include individual moorings to resolve the internal tide, or also idealized numerical models, which neglect the complex wave environment. However, as computational power and model resolution continue to advance, this data-driven approach may prove more effective for diagnosing and quantifying complex nonlinear processes than theoretical methods, which often rely on strong simplifying assumptions. Such a modal decomposition method, which directly extracts these realistic but complex features from model simulations without relying on wave assumptions, is essential for studying wave-eddy interaction under a realistic setting, which we do in the following chapter.

In this chapter we highlighted the need for a modal decomposition method which does not rely on linear wave theory and is thus more appropriate for the output of a non-linear GCM. We presented a novel method based on spatial EOF analysis, assessed its ability to reconstruct the original wave field and compared it with two conventional decomposition methods. Finally, we discussed the advantages and disadvantages of each method.

4

EFFECTS OF MESOSCALE EDDIES ON THE M2 INTERNAL TIDE AND ITS MODES IN DIFFERENT SEASONS

ABSTRACT

One of the processes which are thought to significantly contribute to diapycnal mixing induced by the low-mode IT dissipation is its interaction with mesoscale eddies, as suggested by observational and idealized numerical studies. To the best of our knowledge there is no study yet analysing these interactions using a complex, realistically simulated ocean. We use the ocean-only ICON model at 5 km resolution to investigate these interactions near the Walvis Ridge during a summer and a winter season. The impact of seasonality on the IT and the interactions with eddies is also studied in this chapter. To extract the IT modes, we apply both the SL and our novel EOF decomposition method. The latter does not rely on linear assumptions and is capable of identifying features resulting from nonlinear processes simulated by ICON. Despite methodological differences, both methods lead to similar results, suggesting that nonlinear effects are weak or negligible. An Agulhas ring that crosses a beam of M2 mode-1 IT is causing the beam to refract, characterized by a southward horizontal shift of the beam and an essentially unchanged vertical structure, indicating that the Agulhas ring does not scatter the mode-1 IT into higher modes. Additionally, higher IT modes are found to be trapped within the Agulhas rings before the interaction with mode-1 beams, implying that they do not arise from this interaction. This study offers new insights into IT-eddy interactions in a realistic setting and introduces a framework for analyzing internal tides beyond linear wave assumptions.

4.1 INTRODUCTION

Evidence suggesting eddy-IT interactions has been found from direct observations (Löb et al., 2020; Huang et al., 2018; Li et al., 2016). Löb et al. (2020) detect a damped energy flux in the first and second mode, which could be explained by scattering to higher modes. However, they can not conclusively prove this by using their mooring data. Huang et al. (2018) observe a weakening of low modes and a change in the propagation speed of the IT due to two eddies in the South China Sea. Yet, observations are still too sparse in time and space to be sufficient for describing the details of the interactions. To get more insight into this process, theoretical and numerical approaches have been considered. Several studies focussing on these interactions have been carried out following numerical approaches (Dunphy et al., 2017; Dunphy and Lamb, 2014; Wang and Legg, 2023; Guo et al., 2023). There, the wave-eddy interaction is examined using numerical models, although only configured for idealized conditions. Both theoretical and numerical approaches suggest that an eddy can scatter an incident wave into waves with higher wavenumbers.

Savva, Kafiabad, and Vanneste (2021b) show that eddy-wave interaction can be considered as a triad interaction, during which the internal gravity wave frequency remains unchanged and the wavenumber spreads over the constant-frequency cone associated with internal gravity waves, leading to a cascade of energy across scales. Recently, Wang and Legg (2023) showed that a homogeneous incident mode-1 IT is refracted into convergent energy beams after interacting with stationary baroclinic eddies. They also show that high-mode ITs are trapped in strongly baroclinic eddies, in fact the higher the mode the longer the trapping.

Studies combining numerical models with observational data in the South China Sea (Li et al., 2016; Park and Farmer, 2013) suggest that mesoscale eddies affect internal tides by changing the local stratification and inducing additional background currents, which in turn causes the propagation direction of the beams to shift and the amplitude of the generated M2 internal tides to change. Most recently, the process in that an eddy scatters an incident low-mode IT into high modes with higher wavenumbers, has drawn attention of researchers (Wang and Legg, 2025) in a study that combines Argo data and numerical simulations. This process has a great physical significance, as it produces a possible dissipation pathway of the low-mode IT.

However, it still remains unclear how exactly this scattering process occurs in a realistic setting, since - to the best of our knowledge - there exists no study using a high resolution general circulation model (GCM) to investigate these interactions in a realistic setup. Do the high modes trapped inside an eddy, as reported by several previous studies, indeed result from the scattering of a low mode IT? Also the influence of seasonality, which is strongly present in a complex model like ours, on the internal tide and its interaction with eddies, suggested by observational studies (Liu et al., 2019) is of great interest for complete understanding.

In order to achieve these objectives, we first use our novel modal decomposition method presented in chapter 3 and then compare the results with the ones obtained from the standard method. We do so to assess the degree by which the non-linear interactions between eddies and ITs alter the structures of ITs.
In particular, in case the two methods produce comparable results, the compatibility could indicate a minor role of non-linear processes in altering the wave structures obtained from linear wave theory.

The chapter is organized as follows: section 4.2 explains the experimental setup of the study. In 4.3 we study the influence of Agulhas eddies on the M2 internal tidal frequency followed by their influence of horizontal and vertical scales of the low (4.4) and high modes (4.5) derived by our novel EOF based decomposition method. In 4.7 we compare our results to those obtained when applying the exact and approximate SL decomposition method. Section 4.6 focusses on the effects of seasonality on the eddy-IT interactions. Lastly, in 4.8 we provide a summary and discussion of the complete chapter.

4.2 EXPERIMENTAL SET-UP AND RESEARCH APPROACH

To study the eddy-internal tide interactions, we need a global ocean which is spun up and which possesses a quasi-stationary eddy field on short timescales (days to weeks) with equilibrated total kinetic energy. We do so by first performing a spin-up run. This run starts from an ocean state at rest with a 3-dimensional temperature and salinity distribution interpreted from the Polar Science Center Hydrographic Climatology (Steele, Morley, and Ermold, 2001). The model is then forced by fluxes of momentum, heat and fresh water diagnosed from ERA5 reanalysis, as described in (Korn et al., 2022) and integrated over the period from 2010 to 2021. The globally averaged kinetic energy, shown in figure 18 becomes essentially stationary after ≈ 2 years. Starting from the end state in 2021 (light grey area in Fig. 18), ICON-O is then forced not only by surface fluxes but also by the lunisolar tidal forcing for about ≈ 1.5 years. This run forms the basis of the present study.

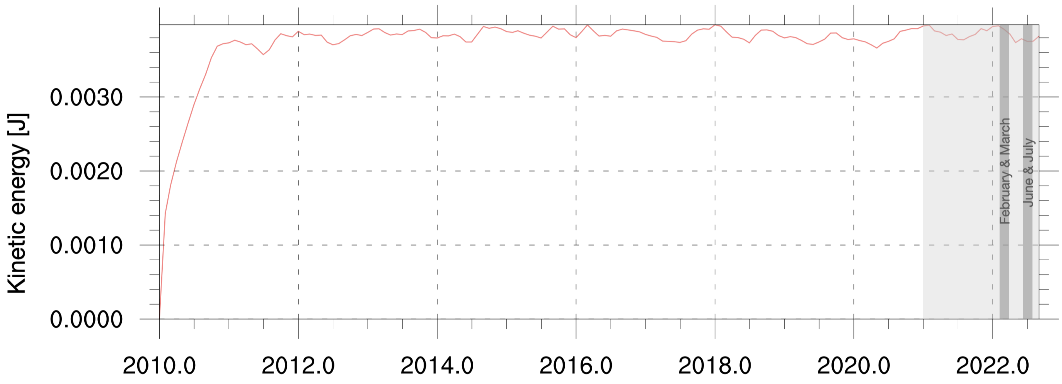

Figure 18: Timeseries of the total kinetic energy. The light grey area represents the run including tidal forcing upon which this study is based. Darker grey areas represent the two seasons, for which high-frequency out is used to analyse the interactions.

In order to properly identify the influence of Agulhas rings on the ITs, we compare ITs at a time when they are not in contact with an Agulhas ring with ITs at a time when they are in contact with an Agulhas ring. Finding such situations from high frequency output of a high-resolution GCM simulation is a challenging task. The difficulty originates from the different timescales of the M2 internal tide and the Agulhas Rings, with the timescales of the latter being much longer than the tidal period. To study eddy-internal tide interactions we need on the one hand high-frequency output to properly resolve and describe the M2 internal tide. Previous studies using numerical models (Li, Storch, and Mueller, 2015; Li and Storch, 2020) and Argo floats (Wang et al., 2023; Hennon, Riser, and Alford, 2014) suggest that hourly output is a good choice. On the other hand, Agulhas rings remain predominantly stationary throughout the M2 period and exhibit minimal movement over time intervals shorter than a week. Hence, daily data are sufficient to describe their propagation. Since we are unable to store hourly 3-dimensional fields for the entire simulation period of 1.5 years, due to the limited storage capacity, the following procedure is developed to overcome the storage problem.

We first run the whole simulation with daily output, storing the instantaneous three-dimensional ocean state at the beginning of every month. These states serve as initial states to be used to rerun the model with hourly output over short designated time periods. We consider two pairs of one-month periods. The first pair consists of February and March of 2022, and the second consists of June and July of 2022 (dark grey areas in figure 18). They are identified by following the propagation of Agulhas rings using animations of horizontal velocity speed over the whole simulation of 1.5 years. During the first month of a pair, our particular beam is free or almost free of any Agulhas rings. During the second month of a pair, there is an Agulhas ring crossing our beam. Such an IT beam is shown in figure 6: The one that is generated at the Walvis Ridge near 32.45°S and propagates mostly zonally toward the African coast, can be most easily crossed by an Agulhas ring. Moreover, due to the reflection off the continental shelf (at around 14°E), the position of this beam appears to be rather stationary throughout the simulation period. In this chapter, we will focus on this particular beam. The effect of eddies on ITs will be studied by quantifying how Agulhas rings alter this beam. The effects of the internal tides on the eddies are assumed to be of less importance and will be ignored in this study. There is another beam south of our beam at 32.45°S. Although somewhat stronger, this beam is not considered, since the Agulhas rings tend to cross this beam further downstream near the end of the beam, leaving little room for quantifying the effect of Agulhas rings on this beam.

The hourly output of the four months is regridded from the unstructured ICON grid onto an 1/10° longitude-latitude grid to reduce overall data size and speed up post-processing. We recognize that regridding results in the loss of fine-scale details and reduces accuracy for small-scale phenomena. However, this is acceptable for our purposes, as we are primarily focused on low-mode internal tides and mesoscale eddies, which have horizontal scales of approximately 100 km.

This study extends the previous numerical studies on the effect of mesoscale eddies on ITs. Our approach differs from the previous numerical studies with respect to the following two aspects. First, we consider realistic simulations performed with the newly developed ocean GCM — ICON-O (Korn, 2017; Korn et al., 2022) — at a horizontal resolution of 5 km forced by surface fluxes derived from the ERA5 reanalysis (Hersbach et al., 2020). This means that the background wave environment, i.e. stratification, eddying circulation, and bottom topography (Becker et al., 2009), in which the wave-eddy interaction takes place, is realistic. This means also that the way how ITs encounter eddies is realistic. In particular, as will be explained later, we consider the situation where a wave beam is naturally crossed by a *travelling* eddy, rather than the situation where an incident IT made to artificially encounter a *stationary* eddy at a fixed location. Secondly, we explicitly identify the low and high modes and the eddies. By doing so, we aim to find out whether the high modes trapped in an eddy result from scattering of which low mode. With these differences in mind, we aim to quantify the impact of eddies on the low-mode internal tides, especially the significance of the scattering process and the relevance of other processes, such as refraction. We are also interested in the eddy impact on the high modes and the influence of seasonality on the IT in general and on the IT-eddy interactions.

4.3 FREQUENCY STABILITY OF THE M2 INTERNAL TIDE IN THE PRESENCE OF AGULHAS RINGS

Internal gravity waves propagate through the ocean (or atmosphere) with a well-defined intrinsic frequency ω_{IGW} in a motionless background. In a more realistic scenario, when there's a background flow propagating with a horizontal velocity **U**, such as a mesoscale eddy, the frequency experienced by an observer ω_{obs} in the moving fluid frame is Doppler shifted by $\pm \mathbf{k} \cdot \mathbf{U}$, ie. increase or decrease depending on whether the wave propagates with (+) or against (-) the eddy flow (D.Olbers, C.Eden, and J.Willebrand, 2012). This may affect analysis methods like spectral filtering or harmonic analysis, especially if the background flow isn't accounted for.

We investigate whether the M2 frequency is measurably Doppler-shifted due to its interaction with the Agulhas rings, which propagate with a horizontal velocity of approximately $0.1\mathrm{m/s}$, as estimated in chapter 2. Given the typical IT wavelengths (≈ 100km) we can expect a Doppler shift on the order of $0.001\ \mathrm{h}^{-1}$. We compute frequency spectra of both barotropic and baroclinic zonal velocities at fixed spatial locations along our focus beam before (February) and after (March) the IT-eddy interaction using the 1-hourly output over these one-month intervals.

We observe no significant shift in the M2 tidal frequency in either the barotropic or the baroclinic energy. Figure 19 shows the mean frequency spectrum for each group of locations for the baroclinic zonal velocity. Given our time window ($\approx$ 30 days per month) and the sampling rate (1h), the spectral resolution is only marginally sufficient to detect such subtle shifts.

We conclude that for the currently available simulations, the possible Doppler shift of the M2 frequency peak can be neglected. In the future, to reduce aliasing and capture possible short-timescale modulations, a higher temporal resolution (eg. 30 min) should be considered.

4.4 IMPACT OF AGULHAS RINGS ON THE LOW MODES

In order to quantify the impact of Agulhas Rings on the vertical structure of the mode-1 IT, the EOF decomposition is carried out in three different ways. First, we perform the EOF decomposition on the combined data set consisting of both the month with and the month without an Agulhas ring on the wave beam, as it is done in subsection 4.4. The resulting mode 1 has, by construction, the same vertical structure in both months. By projecting the February and March (or June and July) data onto α_1 from Eq. (12), we can explore how the horizontal structure related to the same mode 1 vertical structure changes when the beam is crossed by an Agulhas ring. The results of this approach are presented here.

The major impact of an Agulhas Ring on the mode 1 internal tide is a significant change of the propagation direction of the mode, observed as a shift of the associated wave beam. Since an EOF mode propagates with wavenumber vector given in Eq.(17), the wave beam associated with the n-th EOF mode can be identified by wavenumber vector (k_n, l_n) at grid points with maximum velocity of the n-th mode.

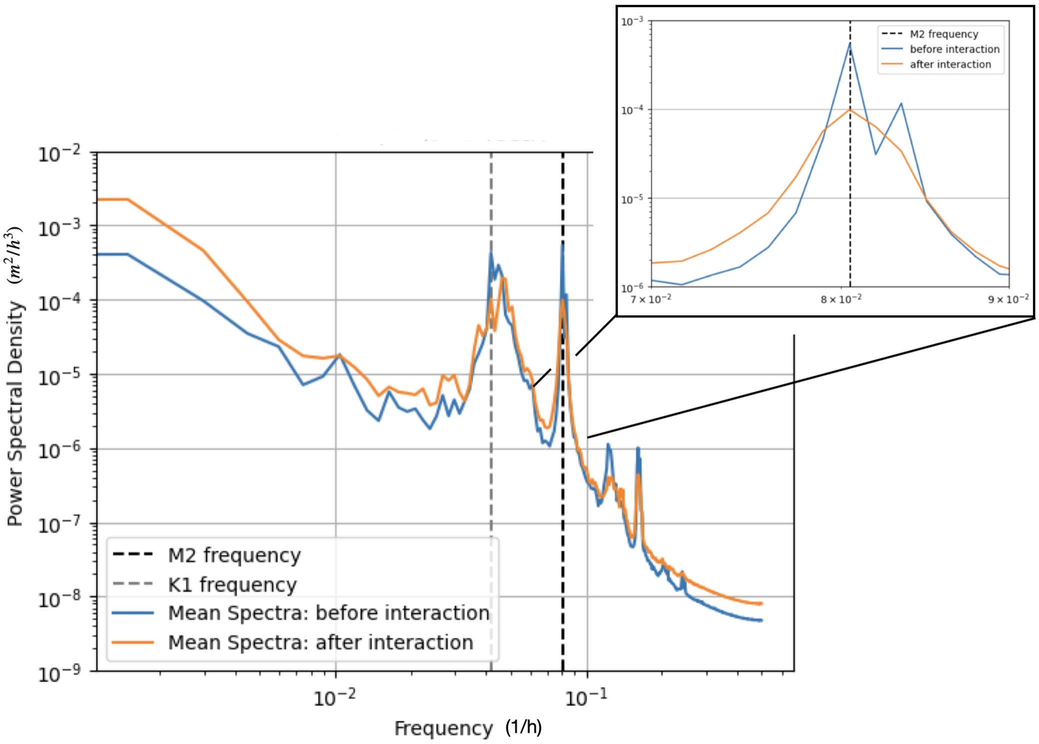

Figure 19: Mean frequency spectra of the baroclinic zonal velocity averaged over 20 fixed locations along the beam during February 2022, ie. before the interaction with the eddy (blue line) and during March, ie. after the interaction (orange line). In the zoomed-in plot we observe no significant shift of the M2 frequency.

During February the beam that is described by the blue wavenumber vectors in Fig.20a, is essentially free of Agulhas rings (black contours). This beam runs almost zonally north of 33°S. When crossed by an Agulhas Ring in March, the beam, now described by the red wavenumber vectors in Fig.20b), is displaced further southward and located mostly south of 33°S. A similar redirection of internal-tide beam is also observed during June and July shown in Fig.21. In June the beam that is described by the blue wavenumber vectors in Fig.21a), is essentially free of Agulhas rings. When crossed by an Agulhas ring in July, the beam, now described by the red wavenumber vectors in Fig.21b), is displaced further southward. We hence conclude that the main impact of an Agulhas ring is to redirect the beam of mode 1 internal tide. Huang et al. (2018) using observations in the South China Sea also find evidence of IT energy refraction caused by an anticyclonic eddy.

Löb et al. (2020) reported enhanced weakening of the energy fluxes of mode 1 and mode 2 in the Azores coinciding with the passing of two eddies during their observational campaign. Since the weakening is observed at a fixed location using mooring data, the observation of Löb et al. (2020) can indicate three possible ways, through which an eddy can impact internal tides. First, if the eddy redirects the wave beam, the weakening could be a result of a spatial shift of the beam. As the beam is moved away from the mooring, the energy flux measured at the mooring decreases. Second, if the eddy does not redirect the beam, the weakening could be a result of energy exchange between the eddy and the beam.

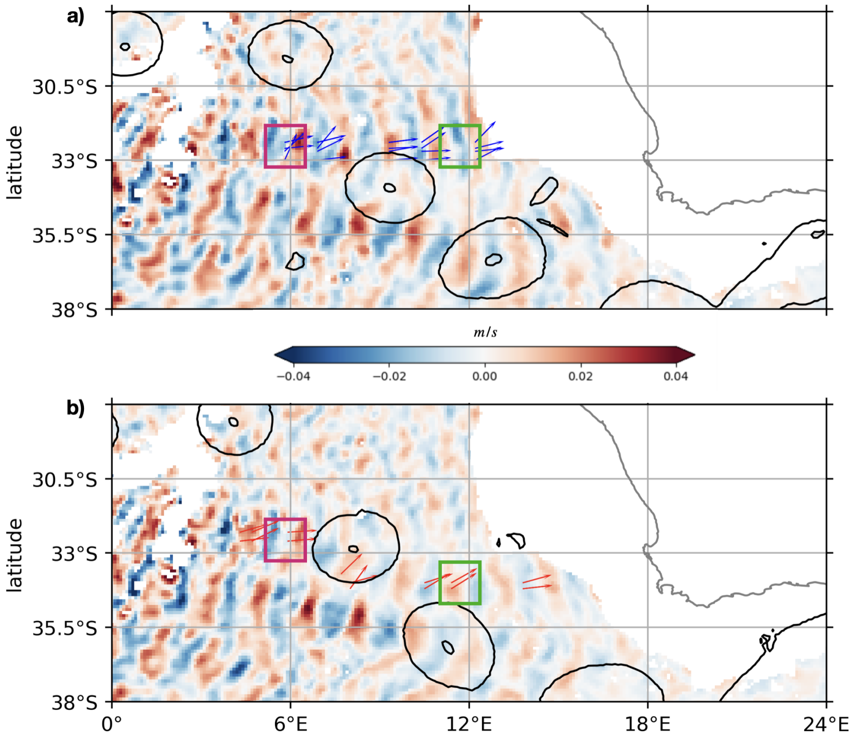

Figure 20: A snapshot of the reconstructed mode 1 zonal velocity of M2 IT during the reference month (a) and the comparison month (b) of our simulation during summer. The coloured arrows are the quivers of the wavenumber vector **K** during each month of the simulation and indicate the propagation pathways. Black contours indicate the eddies.

In this case, the observation of Löb et al. (2020) indicates that the interaction with eddy damps the energy of the low mode. Finally, the eddy can both redirect and damp the low modes of internal tides. Our result that an Agulhas ring redirects the beam is not inconsistent with the observation. Below, we go one step further to quantity how the energy inside the beam of the lowest mode is changed when the beam is crossed by an Agulhas ring.

Whether or not an Agulhas ring can lead to dissipation of the IT can be quantified by comparing the IT kinetic energy E_{kin} obtained from February's data, during which our beam is essentially free of Agulhas rings, with E_{kin} obtained from March' data, during which our beam is crossed by an Agulhas ring, and a similar comparison for E_{kin} in June and July.

To reduce noise, we consider box-averaged E_{kin}, rather than grid-point values of E_{kin}. We focus on boxes that are located near the onset of our beam, which are indicated by the magenta boxes in Fig.20 and Fig.21. E_{kin} averaged over such a box is referred to as E_{os}, and is used to quantify the strength of the internal tide near the generation site of our beam. The values of E_{os} in different months indicate the impact of seasonality on the strength of internal tides. We focus also on boxes that are located downstream of our beam, and in case when the beam is crossed by an Agulhas ring, downstream of the Agulhas Ring. These boxes are indicated by the green boxes in Fig.20 and Fig.21. E_{kin} averaged over such a box is referred to as E_{ds}.

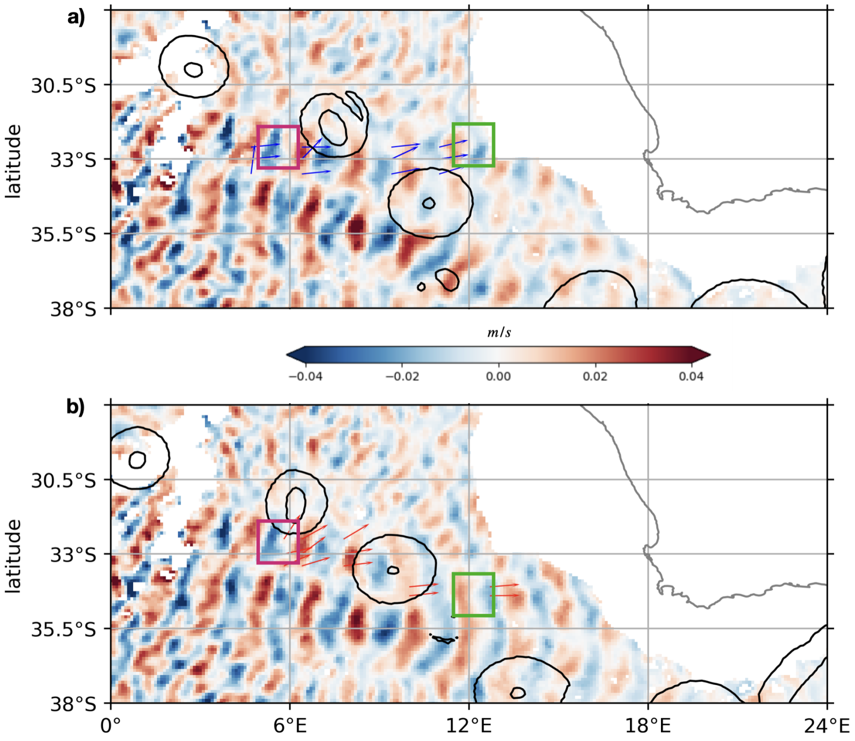

Figure 21: Same as in 20 but for season 2 (June-July)

The ratio E_{ds}/E_{os} on a beam indicates the dissipation of internal tide along the beam. The impact of an Agulhas ring on our beam can be quantified by comparing E_{ds}/E_{os} in a month when our beam is essentially free of Agulhas rings with E_{ds}/E_{os} in a month when our beam is crossed by an Agulhas ring. The result is listed in Table 2.

	FEB (no eddy)	MAR (eddy)	JUN (no eddy)	JUL (eddy)
total	33%	25%	21%	40%
mode 1	33%	21%	18%	44%

Table 2: Ratio E_{ds}/E_{os} of internal tide kinetic energy averaged over a box near the onset of the beam to that downstream of the beam, obtained for four months from the full and mode 1 internal tide velocity. Each box contains 30 grid points. The location of the boxes are indicated in Fig.20 and 21.

Generally, the internal tide loses its kinetic energy as it is propagated along the beam, both for E_{ds}/E_{os} derived from the full internal tide velocity and for E_{ds}/E_{os} derived from the mode-1 velocity. The loss ranges from about 20% to 40%. The impact of Agulhas ring on E_{ds}/E_{os} is different in different seasons. When crossed by an Agulhas ring in summer, the energy loss is stronger, indicated by a smaller value of E_{ds}/E_{os} in March than in February, when the beam is essentially free of Agulhas rings. This is true for E_{ds}/E_{os} obtained both from the full and from the mode-1 velocity, indicating that there is a damping of low mode wave energy due to Agulhas ring. However, the situation is different in winter. The ratio E_{os}/E_{ds} is higher in July when the beam is crossed by an Agulhas ring than in June when the beam is free of any Agulhas rings.

Tab.2 suggests that we cannot clearly conclude that Agulhas Rings damp low mode internal tides. Generally, we cannot rule out the possibility that waves with somewhat different wave properties in different seasons make the behavior of E_{ds}/E_{os} in February/March be different from that in June/July. Our efforts to address this problem by analyzing kinetic energy maps for each simulated month (not shown here), and by comparing the kinetic energy along the February (June) beam with that along the March (July) beam, have not significantly improved our understanding of the energetics of the interaction. Likewise, calculating the frequency spectra of the internal velocities along the beams and comparing the spectral energy at the M2 frequency before and after the interaction (not shown here) has provided limited insight. We conclude that for a more solid quantification of the impact of Agulhas Rings on the wave energy and a better understanding of the energetics of eddy-IT interactions, one should consider a more complete energy budget of the Walvis Ridge region, which is the content of the next chapter.

In order to study the possible effect of an Agulhas eddy on the vertical structure of mode 1 IT, we perform the EOF decomposition on each simulated month separately so that both the horizontal and the vertical structure of the mode 1 are allowed to change due to interaction with an Agulhas Ring. In this case, the EOF analysis is first carried out over the whole study domain, namely that shown e.g. in Fig. 6, which was chosen to allow tracing the origin of the high modes. The resulting PC1 should be considered as representative for the vertical structure averaged over the entire domain. To rule out the possibility that such an average may obscure small changes associated with a particular wave beam, we also repeat the computation, only considering data in a small area that contains essentially only velocities on and near the eddy in question for each month separately, as shown in Fig. 22.

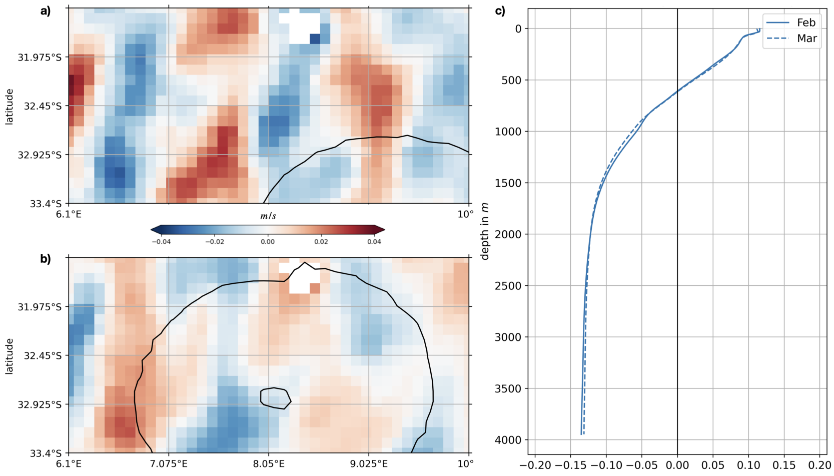

Figure 22: Smaller area chosen for EOF analysis covering only the part of the IT beam on focus being almost eddy-free during February (a) and covered by an eddy during March (b). The correspoinding PCs of mode 1 are shown in (c).

The result of the different EOF decompositions show a PC1 that has essentially the same vertical structure. Thus, we conclude that the vertical structure of mode 1 is unchanged by an crossing Agulhas ring. Below we concentrate on the horizontal structure. We examine how this structure changes from a month during which a mode-1 beam is free of Agulhas ring to a month during which the mode-1 beam is crossed an Agulhas ring. We have in total two cases, namely the case February versus March and the case June versus July.

4.5 IMPACT OF AGULHAS RINGS ON HIGH MODES

The high modes (mode 5 to 10) account together for $\approx 1.4\%$ of the total variance in the data. Despite this small amount of explained variance, and even though they may not be fully resolved by ICON-O with our 5km resolution, the high modes reveal two interesting features, as already presented in chapter 3. First, they are strong in the immediate proximity of the Walvis Ridge. Secondly, they cluster into circular patches with large velocities further away from the Walvis Ridge.

As discussed earlier, we interpret the large values near the Walvis Ridge as the high modes generated at the Walvis Ridge that are quickly damped. When overlayed with the mean flow velocity (see e.g. Fig.23 for EOF 5), we see that the circular patches collocate very well with the Agulhas rings. Thus, we consider these patches as high modes trapped inside the Agulhas rings.

It is tempting to interpret the presence of high modes inside the Agulhas Rings as a result of scattering of a low mode to high modes due to the eddy-wave interaction, as discussed using idealized settings in e.g. Wang and Legg (2023). However, figure 23 shows that the large velocity inside circular patches do not originate from the low mode internal tides, at least not those generated at the Walvis Ridge, but rather they are carried by the Agulhas rings with the Agulhas current around the southern tip of South Africa. These high-mode structures can also possibly be generated through interaction with topography (eg. the coast or the small seamount between 12°E and 16°E), suggested in eg. Johnston, Merrifield, and Holloway (2003) and Klymak, Pinkel, and Rainville (2008). They can even be a result of instabilities or even slaved modes (Chouksey, Eden, and Olbers, 2022).

Thus, we conclude that there is no clear indication that when crossed by an Agulhas ring, the low modes generated at the Walvis Ridge are scattered into high modes. A much longer simulation at higher resolution would be necessary to identify the generation site and propagation pathway of the high modes found trapped in the eddies and conclude whether or not they might result from scattering of low mode tidal beams by a travelling eddy.

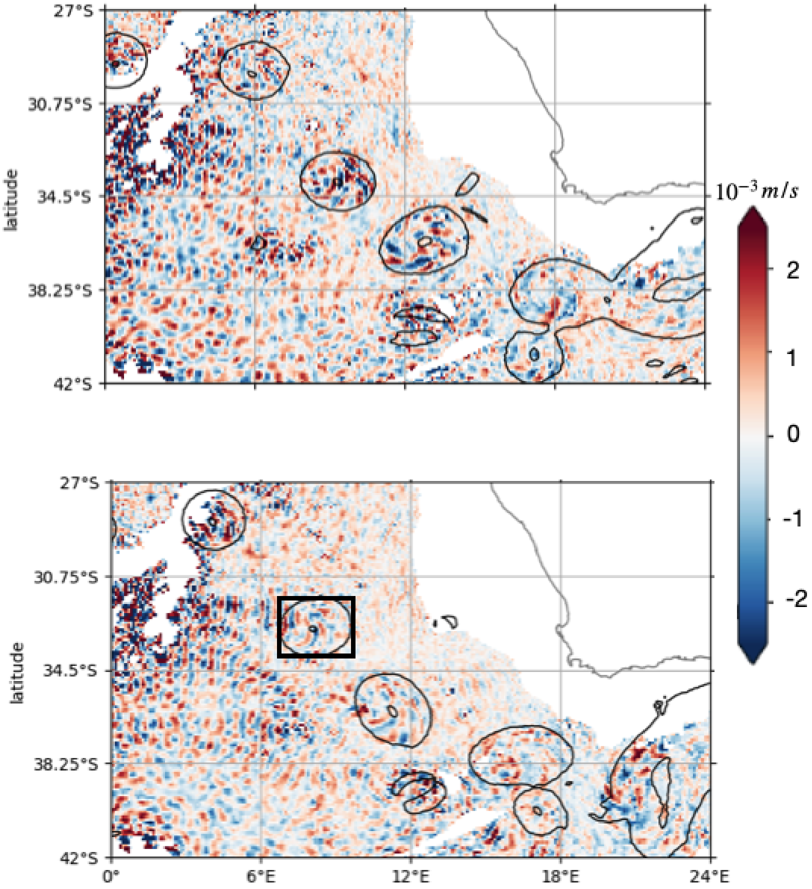

Figure 23: High mode (5) internal tides during the first season (shadings) during reference (a) and comparison month (b) based on our EOF decomposition. Black contour lines indicate the mean magnitude of horizontal velocity during the corresponding month. The black box indicates the area A used to estimate the mean horizontal wavelengths for all modes.

Looking at the two terms of the EOF decomposition e_5^s and e_5^c similar to figure 11b and recalling that they occur with a shift of a quarter of a M2 period, we can see in the upper right insert in Fig.24 that the trapped high modes in the Agulhas rings are also horizontally propagating waves.

However, as noted in the previous chapter, not all patches of high modes are clearly associated with Agulhas rings. This is the case for the patch in the vicinity of a small seamount near 36.5°S between 6°E and 9°E Fig.23. The lower left insert in Fig.24 shows the two parts of EOF5, e_5^c in colors and e_5^s in contours, essentially overlapping with each other, indicating a horizontally standing wave. These standing waves may represent lee waves resulting from the interaction of the IT with the nearby topography (small white spot inside the lower left insert) (MacKinnon et al., 2017).

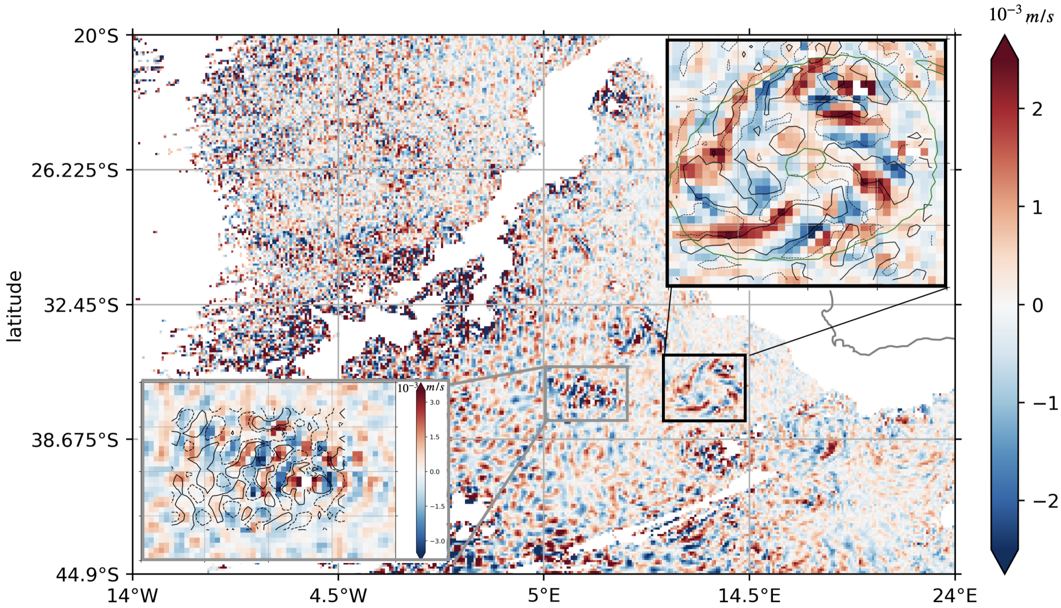

Figure 24: Same as Fig.11b, but for EOF5 and with two enlarged inserts. The thin green contour in the upper right insert indicates an Agulhas ring. The small white spot in the lower left insert indicates a sea mount.

4.6 EFFECTS OF SEASONALITY ON THE INTERACTIONS

In this section we aim to investigate the possible influence of seasonality on the diagnosed M2 internal tide, its modes and the effects of eddies on them. For this we analyse the output of the same two time periods: February and March 2022 (local summer) and June and July 2022 (local winter). As shown in figure 10, the mean stratification of two seasons vary a lot, which introduces a further complexity into the wave environment. We start by comparing the horizontal wavelengths as a function of mode number during the two seasons. For this we use the area-averaged wavelengths for the area shown in 25.

Two features are observed from the area-averaged wavelengths shown in Fig.25. The first one is a decrease in horizontal wavelength with increasing number of EOF, from approximately 137 km in summer and 157 km in winter for the first mode to approximately 56 km in summer and 63 km in winter for the ninth mode. The decrease of horizontal structures with decreasing vertical structures is also in general consistent with internal gravity waves (Gerkema and Zimmerman, 2008). This decrease is most prominent for the low modes, but weakens for higher modes. For $n > 5$, the decrease becomes hardly recognizable, and the wavelength becomes by and large independent of the mode number. We speculate that this may be a consequence that ICON-O in 5km resolution can only resolve the first 3 to 4 modes fully. The situation may change when the horizontal resolution is increased.

The second feature is the notable dependence of the mean wavelength on season: the mean wavelength λ_n during summer is shorter than that during winter, especially for mode 1. The difference in wavelength is likely caused by the strong seasonality in stratification. According to Fig.10, the buoyancy frequency N in the average area (boxes in Fig.13) increases from about 10^{-3} in winter to about 10^{-2}

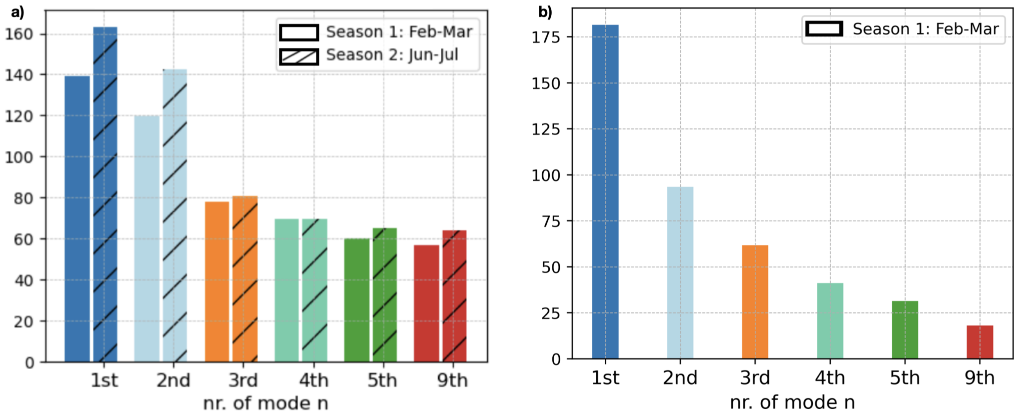

Figure 25: Area-averaged wavelength λ_n as defined in Eq.(18), for the two cases: a) EOF decomposed modes, derived for summer (non hatched) and winter (hatched) in km. and b) SL decomposed modes. The area used for the averaging is indicated in Fig. 23.

in summer, by almost one order of magnitude. Fig. 25a suggests that stronger stratification leads to waves with shorter wavelength. A more in-depth analysis of the seasonal variability of wavelengths and a clearer determination of whether this is a consistent seasonal effect would require a much longer simulation spanning multiple winters and summers. From the current simulations, we consider this a strong indication.

The seasonality in stratification impacts not only the wavelength, but also the wave intensity. In terms of wave energy E_{kin} near the onset of the beam, table 3 shows that the internal tide is stronger in summer than in winter. We conclude that stronger stratification leads to stronger and shorter internal tides. A similar seasonal impact on wavelength is also found by Liu et al. (2019) who compared the IT wavelengths in the Yellow Sea between November and May combining numerical modeling and observations.

	FEB (no eddy)	MAR (eddy)	JUN (no eddy)	JUL (eddy)
total	18	16	14	10
mode 1	0.98	0.92	0.77	0.5

Table 3: Mean kinetic energy averaged over a box near the onset of our internal tide beam, E_{os}, derived from the full and mode-1 internal tide velocity in each of the four considered months. The unit is cm^2/s^2. Each box contains 30 grid points. The location of the boxes is displayed in Fig.20 and 21.

Accompanied by an increase in horizontal wavelength is an increase in vertical scale in winter relative to that in summer. Comparing the vertical structures of the low modes (1 to 3), we observe a deepening of the low-mode nodes during winter (dashed lines in Fig. 26), likely also caused by the seasonal stratification differences. This change in vertical scale is in line with observations using mooring data in the South China Sea (Yang, Li, and Feng, 2023).

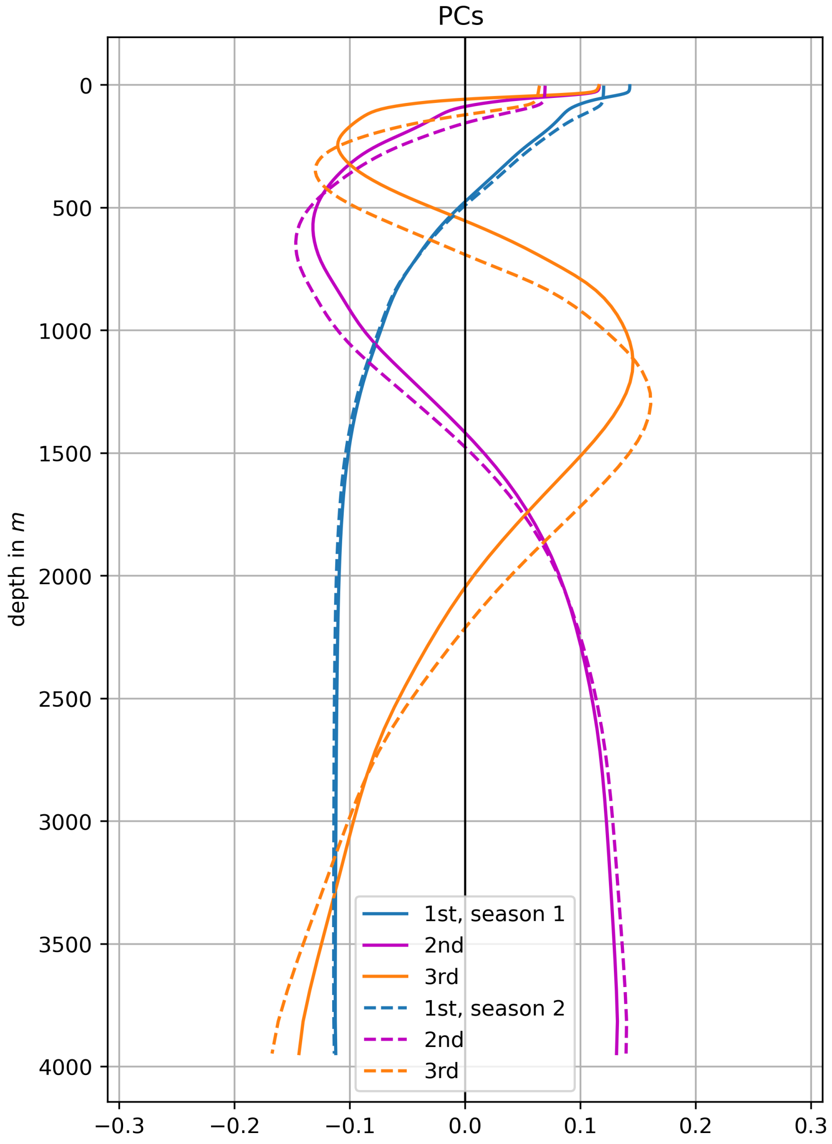

Figure 26: Principal components PC1 (blue), PC2 (magenta), and PC3 (orange) in summer (February/March, solid lines) and in winter (June/July, dashed lines).

4.7 REPRESENTATION OF EDDY EFFECTS BY ALTERNATIVE DECOMPOSITION METHODS

In this section we expand the results obtained by our novel EOF modal decomposition method by adding the ones obtained by the standard modal decomposition method, discussed in chapter 3. We compare both with the exact solution of the Sturm-Liouville eigenvalue problem from 3.4 and the approximate solution from 3.4.2.

If a feature is identified by both decomposition methods, this is considered to be generated without involving strong non-linear processes. This consideration is valuable, as we cannot a priori rule out the possibility that the interaction between eddies and ITs is nonlinear. However, if a feature is described differently by the two different methods, we interpret it as an indication that nonlinear processes are involved in shaping this feature, even though further investigations are required to diagnose and understand these processes.

4.7.1 *Exact SL solution*

Figure 27 shows the resulting mode 1 IT and figure 28 shows mode 5 during February (a) and March (b). We observe that the southward shift of the mode 1 beam following the interaction with the eddy - as previously recognized using our EOF decomposition method - is clearly visible. Additionally, the trapping of the higher modes (here again mode 5 shown) inside the eddies, revealed by the EOF method, is visible.

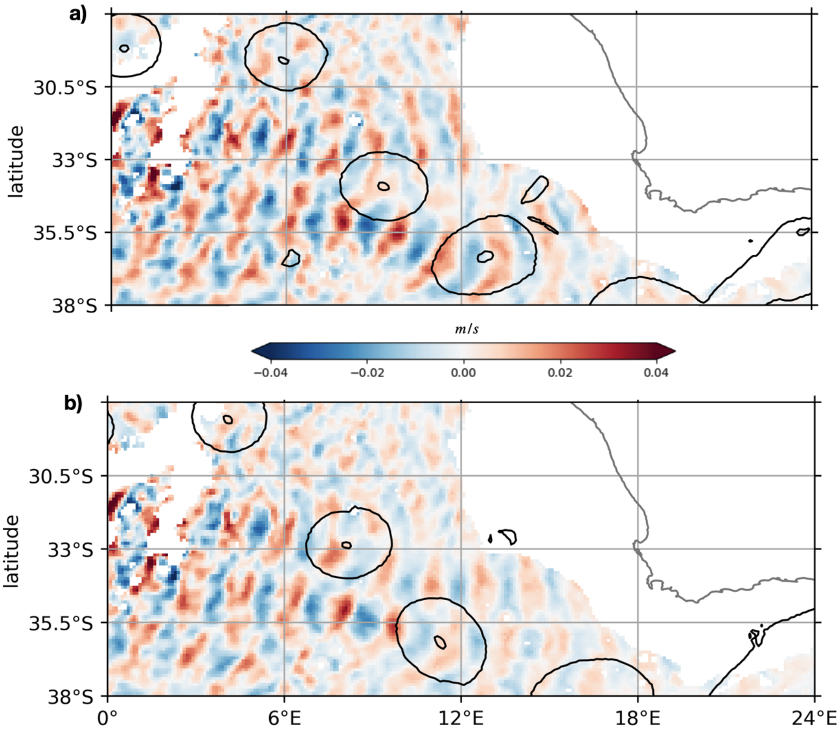

Figure 27: A snapshot of the reconstructed SL mode 1 zonal velocity in m/s following Eq.(22) with $t = 1$ for February (a) and March (b) 2022. Black contours indicate the eddies.

4.7.2 *Approximate SL solution*

We find that mode 1 derived from the approximate method captures well the original IT (prior to decomposition). Most importantly, the southward shift of the beam after being crossed by an Agulhas ring is clearly visible in both cases. The main difference between the horizontal structures shown in Fig.29 and Fig.20 is that the former has somewhat stronger magnitude than the latter.

Figure 30 shows mode 5 decomposed by the approximate solution of SL. The incorrectness of the high-mode representation was discussed in chapter 3 and creates doubts of whether or not the representation of the low modes using the approximate solution can be trusted. We conclude that this method is not appropriate for studying the effects of eddies on the different modes of the IT.

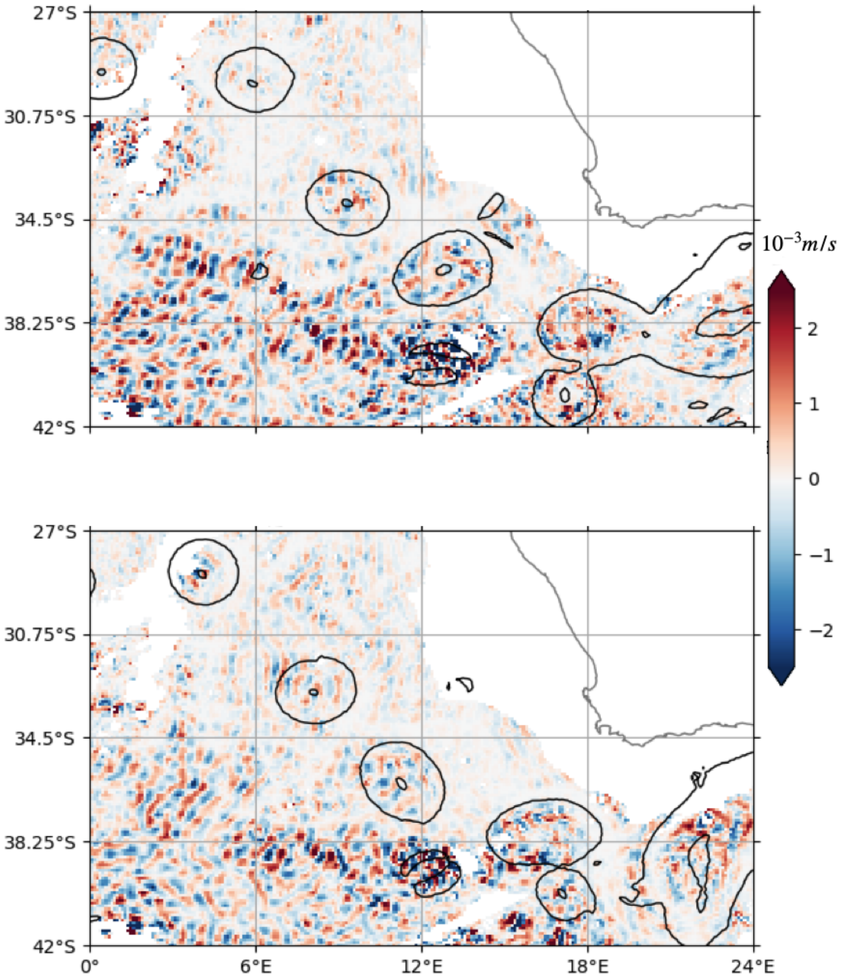

Figure 28: High mode (5) internal tides during the first season (shadings) during reference (a) and comparison month (b) based on the exact solution of the Sturm-Liouville decomposition method. Black contour lines indicate the mean magnitude of horizontal velocity during the corresponding month.

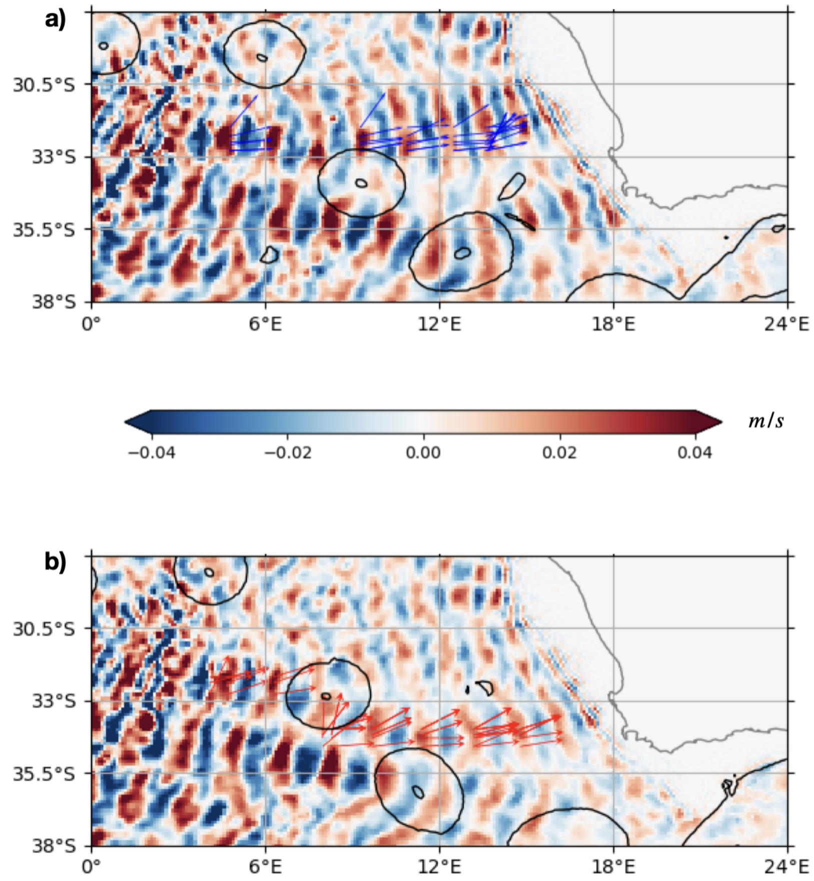

Figure 29: Same as Fig.20, but for mode 1 zonal velocity obtained by projecting $C(x, y, z)$ and $S(x, y, z)$ onto $a_{1,\text{approx}}$.

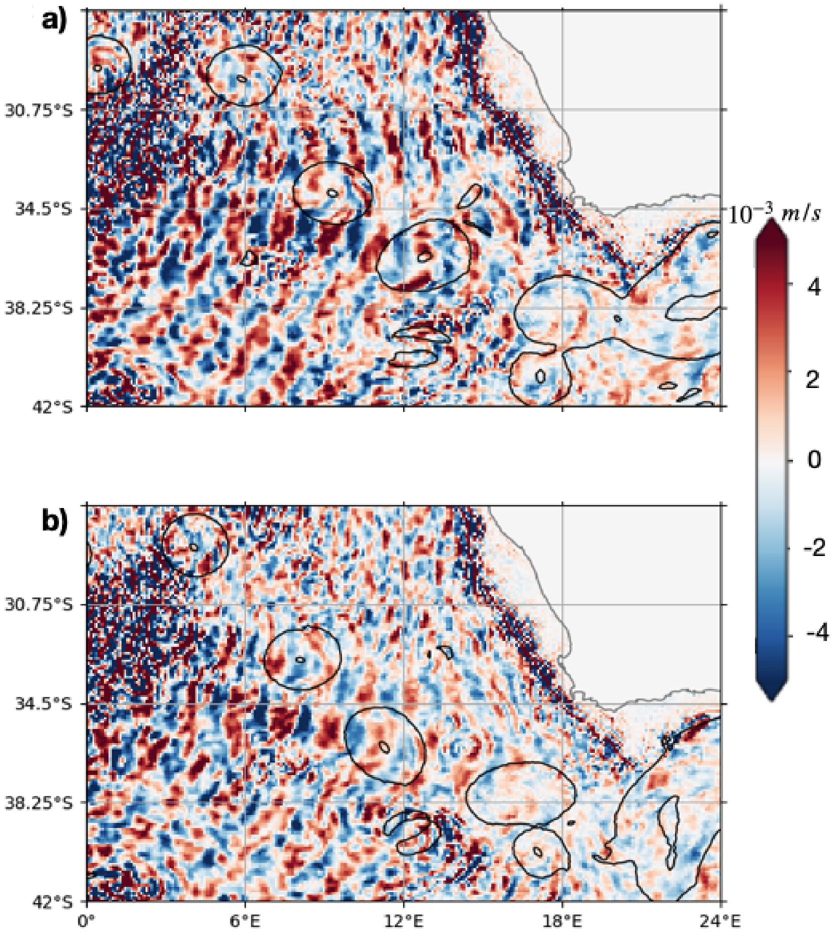

Figure 30: Same as Fig.23, but for mode 5 zonal velocity obtained by projecting the full zonal velocity onto $a_{5,\mathrm{approx}}$.

4.8 SUMMARY AND DISCUSSION OF CHAPTER 4

In this chapter, we studied the eddy-induced changes in M2 internal tides using the global general circulation ocean model ICON-O at 5km horizontal resolution with 128 vertical layers. This is, to our knowledge, the first study addressing this topic based on a high-resolution GCM. We focused on the Walvis Ridge region where both features are strongly present and the internal tides are embedded in a spatially and temporally varying wave environment.

To investigate the impact of eddies on different modes of the IT we employed two decomposition methods: both the standard decomposition based on solving the SL equation and a new data-driven EOF decomposition. The former is performed at each grid point. The 3-dimensional structure of a SL mode is obtained by combining the solutions at all grid points, albeit the SL equation does not provide any information about how the results at different grid points are linked to each other. In contrast, the latter extracts the spatial structure of the IT directly from model simulations without relying on assumptions underlying linear wave theory. Each EOF mode represents horizontally propagating (or standing) waves that has a fixed vertical structure and variable horizontal wavelength. When both methods identify the same wave feature, it suggests that linear theory is sufficient to describe the dynamics, indicating a minor role of non-linear processes.
However, when the results differ, it may signal the presence of non-linear interactions, though further investigation would be needed to confirm this.

Our analysis of the EOF modes revealed that the ITs in the Walvis Ridge region are dominated by mode 1, which explains over 70% of the total vertical variance and travels all the way from the ridge to the coast of African continent. Higher modes tend to have large magnitudes in the direct vicinity of the Ridge, or in form of patches. These patches often represent waves trapped inside Agulhas rings, but occasionally also lee waves arising near small sea mounts without involving strong eddies. The mean horizontal wavelength decreases with increasing mode number from around 150 km for mode 1 to about 60 km for mode 9, even though the decrease is hardly noticeable for mode number larger than three, possibly due to the fact that the model resolution is not sufficient to fully resolve the high modes. Seasonal differences in stratification also influence modal properties: stronger stratification in summer than in winter amplifies the modes, shortens the horizontal wavelengths, and raises the zero-crossing points in the vertical modal structures. Regarding the role of Agulhas rings, we find that the main effect of Agulhas rings on internal tides is a refraction of mode 1 that makes its beam to shift southwards. The same southward shift is found in both months when a mode-1 beam is crossed by an Agulhas ring. The refraction concerns only the propagation path, without noticeably altering the vertical structure of mode 1. The high modes are trapped and carried by Agulhas rings as they enter the Atlantic from Agulhas retroflection region. As such, these modes cannot be considered as resulting from scattering of mode 1 generated at the Walvis Ridge by eddies.

Comparing the EOF modes with the SL modes reveals both similarities and differences. Regarding the role of Agulhas rings, their effect is identified by both decomposition methods as a refraction of mode 1, characterized by a southward shift of the beam without noticeable change in vertical structure.

This result suggests that the interaction between eddy and IT, at least that occurring in the Walvis region, does not involve strong nonlinear processes capable of producing waves that are strongly different from those described by linear wave theory. However, notable differences exist in wave properties: SL mode 1 wavelengths are longer and those of higher SL modes shorter than the corresponding EOF modes. The difference can be as large as 25 to 35%. Furthermore, SL high modes have vertical structures that vary strongly from grid point to grid point, whereas all EOF modes have a fixed vertical structure by construction. We also briefly looked at the IT energetics before and after interacting with an Agulhas ring. Our findings on the eddy-induced change of the kinetic energy E_{kin} suggest weakening of the full and mode 1 E_{kin} during summer (Feb-Mar). However, during winter (Jun-Jul) we observe a counter-intuitive strengthening of the IT kinetic energy. A possible explanation could be the seasonal variability of the IT properties. While our findings offer new insight into wave-eddy interactions, the detailed energetics remain unresolved. A full energy budget for this region should be conducted. This will allow for a deeper understanding of the energy transfer between modes and/or between the internal tide and eddies. This is the topic of the next chapter.

This study marks an important step toward quantifying the wave-eddy interactions in realistic global general circulation model simulations. Our results are likely more representative of real-world ocean dynamics due to both the more realistic encounter of waves with eddies and spatially varying environment simulated by the model.

In this chapter the novel decomposition method based on EOF spatial analysis was used to study the effects of a mesoscale eddy on the different IT modes in two seasons. We find that the low modes are refracted southwards while the high modes get trapped and transported by the eddies. Seasonality doesn't influence the eddy effects, but affects the mean horizontal wavelength and the wave intensity. The similarity of our results to the ones derived using linear wave theory is a strong indication that non-linear effects might be negligible.

5

ENERGETICS OF THE EDDY - INTERNAL TIDE INTERACTIONS

ABSTRACT

The energetics of the eddy - internal tide interactions still remain an open question among researchers. Studies based on observations and idealized numerical simulations suggest that eddies can dampen the energy flux of low-mode IT. It remains unclear whether this is the case in a realistically simulated ocean. In this study we aim to first answer whether and to what extent the overall energetics in the study area are altered due to the presence of eddies. Secondly, we are interested in whether or not the low mode of the M2 IT is more strongly damped in the presence of eddies. We utilize a novel configuration of the ICON-O model, which is capable of sufficiently resolving the high modes of the internal tide due to its gradually refined horizontal grid in the study area. Using our novel modal decomposition method we can study the energy fluxes of low and high modes of the IT in regions with and without strong mesoscale eddies and conclude on their importance when it comes to energy dissipation eg. through scattering of the low-mode waves into waves with higher wavenumbers possibly caused by an eddy.

5.1 INTRODUCTION

A key aspect of understanding the eddy-internal tide interactions lies in analyzing their energy exchange. Current and past research suggest that as ITs propagate through mesoscale eddies, energy exchange between them may also happen. Both observational and numerical studies have been conducted to shed light on this complex interaction. In a study based on direct observations in the Azores by Löb et al. (2020) the characteristics of the internal tide beam changed considerably after the passing of two eddies. In fact they observed an enhanced weakening of mode 1 (31%) and mode 2 (61%) energy flux compared to the values prior to the interaction. Huang et al. (2018) computed the depth-integrated mode-1 energy at a line of moorings during eddy and no-eddy periods for reference. They report a large decrease in mode-1 semidiurnal IT energy in the eddy period, from which the magnitude of depth-integrated mode-2 energy was increased by more than 5 times compared to that during the eddy-free period. This suggests that, through interacting with mesoscale eddies, the mode-1 IT is a possible energy source for the intensified higher-mode ITs. However, mooring data cannot sufficiently resolve baroclinic modes larger than 3, which are the ones that can potentially contribute to dissipation, wave breaking and mixing due to their very small horizontal structures and high vertical shear. Additionally, the formation of higher-mode ITs due to eddies still needs to be confirmed by observations. In general, observational data are still sparse in space and time and cannot provide full understanding.

Idealized numerical simulations performed by Dunphy and Lamb (2014) showed that a mode-1 baroclinic eddy could result in the scattering of energy from the incident mode-1 ITs to modes two and higher. They also found that energy is transfered from low to high modes through the eddy-IT interaction. Wang and Legg (2023) reported enhanced internal tide dissipation caused by a mesoscale eddy using an idealized setting. They also find that higher modes are trapped inside the eddy, with this trapped high-mode energy potentially being responsible for the enhanced dissipation. Most recently the same authors show that Agulhas rings are hotspots for internal tide dissipation (Wang and Legg, 2025). By quantifying the internal tide dissipation using model simulations and estimating dissipation rates from Argo floats, they suggest that the enhanced dissipation inside Agulhas rings is due to the transfer of internal tide energy from stable low wave numbers to less stable high wave numbers.

On the other hand, evidence suggesting the influence of internal tides on the eddy energetics has also been found. Observations by Cusack et al. (2020) using a mooring array over an abyssal hill in the Scotia Sea show that eddies gain energy of around $1 \text{mW}/\text{m}^2$ from the internal tide, suggesting that the eddy-IT interactions may play a significant role in modifying the Southern Ocean mesoscale eddy field. Based on this, Shakespeare (2023) uses a simple theoretical model and finds that internal tides can accelerate the eddies by increasing the eddy kinetic energy and reduce their lifetimes, in the presence of a critical level.

These studies demonstrate that internal tide–eddy interactions can significantly alter the energy distribution among the two features, often resulting in enhanced higher-mode energy and dissipation. What is still lacking is a detailed and spatially explicit assessment of internal tide energetics in a realistic ocean environment, especially regarding how mesoscale eddies might redistribute energy between modes or influence local dissipation. Most importantly, it remains unclear whether the energetics signatures identified in simplified or localized studies are also found in global high-resolution ocean simulations.

In this study we aim to overcome these difficulties and gain a deeper understanding on the eddy-IT energetics. We utilize a novel configuration of ICON-O with the unprecedented horizontal resolution of approx. 600 m in the focus area, which allows us to accurately simulate the dynamics of the area, resolve the high modes of the IT (we focus on mode numbers up to ten) and diagnose the energy fluxes at each grid point. We are interested in the energetics of the area, in particular the possible differences arising from the presence of a strong eddying background field. To gain a more general understanding on the energetics of this simulation, we first look at the total depth-integrated energy fluxes, as well as the ones corresponding only to superinertial or subinertial frequencies. Moving on to the M2 internal tide, we compare the ratios of outgoing versus incoming energy fluxes across corridors with different background eddy activity. Finally, using our novel modal decomposition based on EOF analysis, we investigate the ratios of low and high modes across the corridors. Our preliminary results suggest that eddies tend to increase the ratio of outgoing versus incoming energy flux, which mainly occurs along their propagation direction. The strongest downstream increase is the one of mode 5 IT energy flux.

The chapter is organized as follows: Section 5.2 introduces the new simulation and explains the experimental setup of the study and the research approach. In 5.3 we present first insights of the new simulation regarding the presence of high-mode waves and in 5.4 we show preliminary results of the energetics in the research region and the possible influence of eddies. Lastly, in 5.5 we provide a summary and discussion of the chapter.

5.2 THE SMT SIMULATION AND EXPERIMENTAL APPROACH

We use the eddy-resolving global GCM ICON with a global horizontal resolution of 5km which is gradually refined to ca. 600 m in the region of interest (Korn et al., 2022; Hohenegger et al., 2023). Additionally, we have high vertical (128 levels) resolution and hourly frequency output. For the analysis we use the output of one simulated month. The structure-preserving discretization of the primitive equations, as described in detail in Korn et al. (2022), allows for a continuous refinement. The horizontal resolution of this configuration amounts to 5km globally and is then being gradually refined to approximately 600m in the focus area, as shown in figure 31.

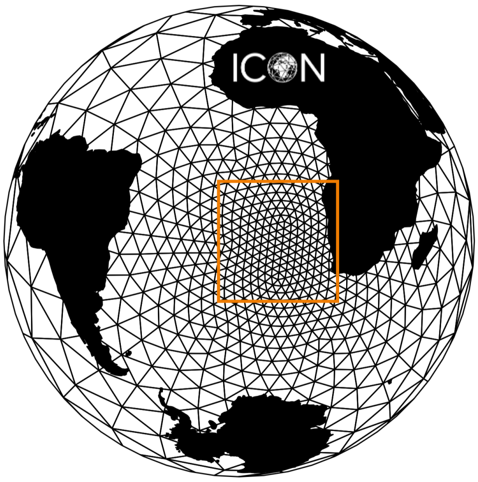

Figure 31: The global unstructured grid of our SMT simulation. The horizontal resolution is gradually refined from 5km to approximately 600m in the study region in the south-east Atlantic ocean, indicated by the orange box. (credits: Nils Brüggemann)

This novel configuration of the ocean component of ICON (in the following abbreviated as SMT, short for *Sub-Mesoscale Telescope*) makes it possible to simulate submesoscale dynamics in the focus area, depending on the seasonal variation of the mixed layer thickness (Dong et al., 2020). We initialize ICON-SMT by interpolating data from a coarser ICON simulation with 5km grid spacing (ICON-R2B9) that ran for seven years (2015-2022) forced with ERA5 reanalysis data (Hersbach et al., 2020). Traditionally, the advent of a new model necessitates a model evaluation, for ICON-SMT this was conducted in Epke and Brueggemann (2025) for a similar configuration with focus in the North Atlantic and is currently under review.

In order to study the energetics of the Walvis ridge area where the eddy-IT interactions take place, we use the described novel configuration ICON-SMT. Since such a simulation is computationally very demanding, we have to restrict to a shorter period for the data analysis, which in this case only includes one month, February 2022. The vertical and temporal resolution of the new run remains the same as in the previous chapters. The hourly output of the simulated month is regridded from the unstructured ICON grid onto an $1/50^{\circ}$ longitude-latitude grid to reduce the overall data size and speed up the post-processing.

5.3 HIGH MODE WAVES IN THE SMT SIMULATION

We start analysing this new simulation by diagnosing the M2 internal tide zonal velocity, as explained in Section 2 and decomposing it into the first ten modes using our newly developed method introduced in Chapter 3.

Table 4 presents the variance per mode and the accumulated variance up to the $n-$th mode for both simulations. Comparing the distribution of the variance in the SMT simulation to the R2B9 one, we observe that the total accumulated variance arising from all ten modes as well as the mode 1 variance are smaller in the higher resolution (SMT) run. On the other hand, the higher modes carry more variance in the SMT compared to R2B9 simulation, ie. the small-scale internal tides seem to be more energetic than the corresponding modes in the R2B9 simulation.

EOF number	1	2	3	4	5	6	7	8	9	10
SMT variance (%)	**61,4**	18,2	8,1	4,1	**2,5**	1,5	1	0,77	0,57	0,38
R2B9 variance (%)	**74,4**	17,2	5,1	1,7	**0,7**	0,3	0,2	0,1	0,06	0,04
SMT accum. var. (%)	61,4	79,6	87,7	91,8	94,2	95,7	96,7	97,47	98,04	**98,5**
R2B9 accum. var. (%)	74,4	91,7	96,7	98,4	99,1	99,4	99,6	99,7	99,76	**99,8**

Table 4: Variance per mode n (upper half) and accumulated variance up to the n-th mode (lower half) for the M2 IT zonal velocity for the new **SMT** simulation in comparison to the same values for our previous (R2B9) simulation.

This is something that we generally expect, since in a higher resolution dataset, the amount of grid points is higher, which leads to a larger covariance matrix and a higher number of spatial degrees of freedom. As a consequence, the total variance is more evenly distributed across all modes. Additionally, small-scale features are better resolved and the spatial complexity increases with increasing resolution, while the variance is dominated by large-scale low modes in the coarser resolution since finer scales cannot be resolved.

By comparing the horizontal distribution of the high mode 5 in the two simulations, as shown in figure 32, we observe something less expected. In fact the strong high-mode signals which were previously concentrated close to the generation site and trapped inside the eddies, are now visible in the complete area, as shown in figure 32b. Additionally, the mode 5 waves are stronger in SMT than in R2B9, indicating that the processes resolved with higher resolution, which increasingly resemble the dynamics of the real ocean, allow for more high-mode waves to be generated.

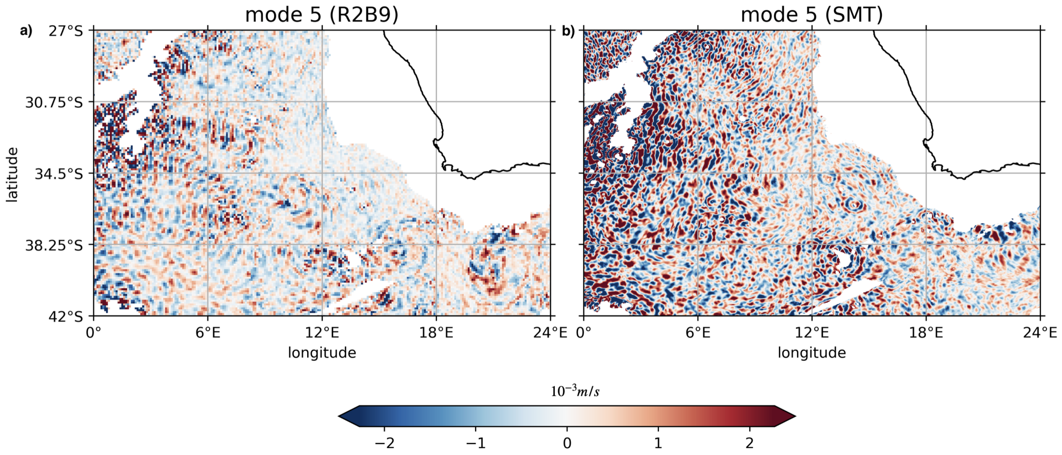

Figure 32: Mode 5 derived by the EOF decomposition method for the R2B9 simulation (a) and the SMT simulation (b) for comparison.

The observation that higher modes contribute more significantly to the variance and exhibit stronger signals across broader regions suggests that their role in the area's dynamical processes may be more substantial than previously assumed. This is in accordance to the study by Vic et al. (2019), who combined a semianalytical model of IT generation with in-situ measurements and satellite data and showed that the importance of such small-scale ITs on turbulent mixing accounts for more than 50% of the global IT generation, breaking and mixing, which was previously widely underestimated.

5.4 BAROCLINIC ENERGY FLUX RATIOS IN REGIONS WITH VARYING BACKGROUND EDDY ACTIVITY

5.4.1 *Super- and subinertial baroclinic energy fluxes*

To gain a more general understanding of the energetics of the research area, we first focus on the energy fluxes, which are mainly related to waves (superinertial band) and the ones mainly related to mesoscale eddies (subinertial band). To decompose the horizontal velocity and pressure terms into super- and subinertial domains, we choose a fixed cutoff Coriolis frequency which corresponds to the northernmost latitude of the study area (20°S). This ensures a clear separation and avoids the possible ambiguity of some frequencies considered *subinertial* in one place and *superinertial* in another, but might as well under- or overestimate some frequencies at the southernmost latitude. However, since we are most interested in the M2 frequency, we consider this filtering as useful. Figure 33 shows the filtered super- (in turquoise) and subinertial zonal velocity, as an example.

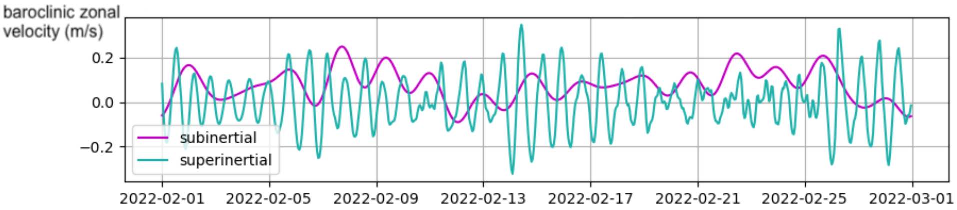

Figure 33: Timeseries of the filtered zonal velocity during February 2022: subinertial (purple) and superinertial band (turquoise).

5.4.2 *Energy fluxes across corridors*

To study the possible influence of mesoscale eddies on the energetics, we define domains with different degrees of eddy activity as three-dimensional corridors along the whole water column. These are marked in Fig. 34: black (white) corridor indicating strong (weak) eddy activity. Then we calculate the ratio of outgoing versus incoming energy fluxes along each side of the corridor. The domain with weaker background eddying activity is in this case considered as reference. By comparing those two, we aim to quantify the role of eddies on possible differences in the energy fluxes. We define the ratios of outgoing versus incoming energy fluxes as

$$\zeta = \frac{\mathbf{F}_{\mathrm{E,out}}}{\mathbf{F}_{\mathrm{E,in}}} \tag{28}$$

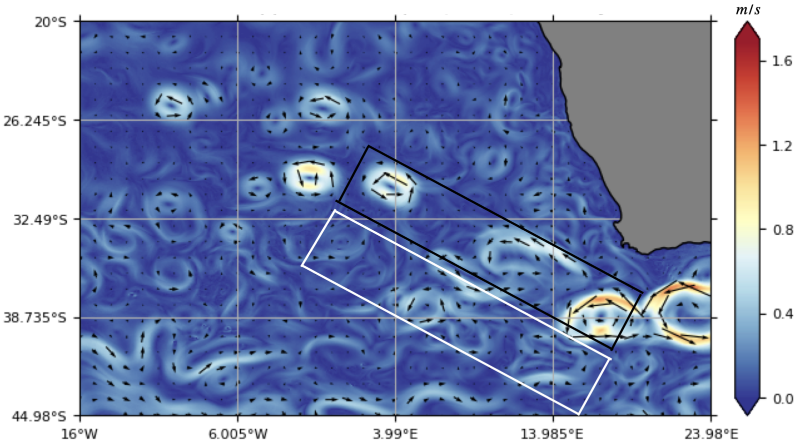

Figure 34: Mean horizontal current speed in m/s during February 2022, simulated by the SMT configuration with the corridors used for the analysis with strong (black corridor) and weak (white corridor) eddying background.

We first compute the full baroclinic energy fluxes $\mathbf{F}_{\mathrm{E}}$ using Eq.(9) as explained in chapter 2. The mean baroclinic energy flux $\mathbf{F}_{\mathrm{E}}$, derived as in Section 2.2.3, at one depth level is shown in Fig. 35a.

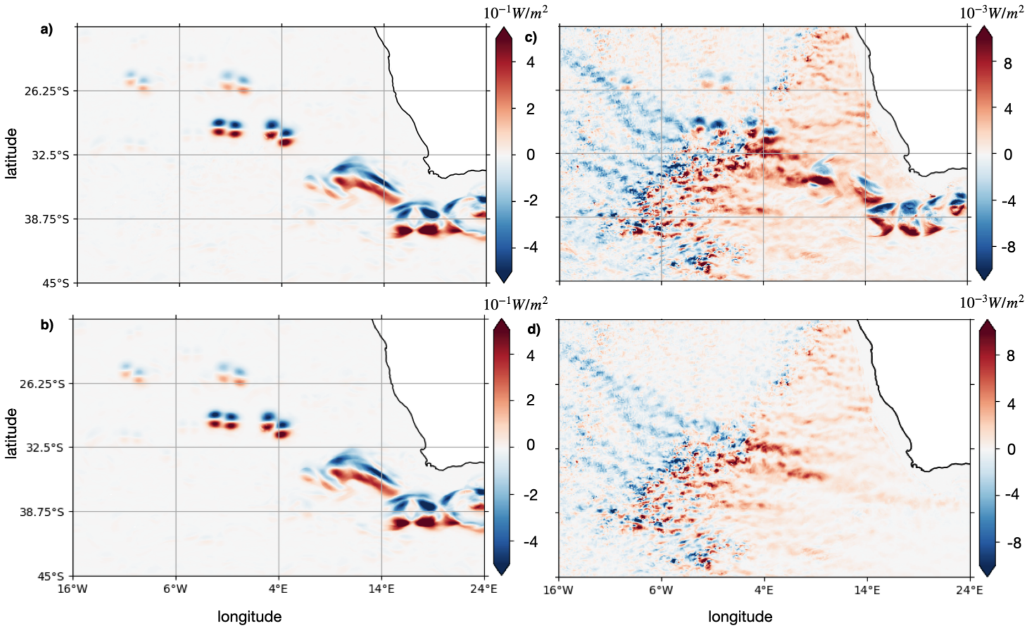

Figure 35: Monthly mean energy flux (W/m^2) in zonal direction at 100m depth for: a) baroclinic total flux b) subinertial component c) superinertial component and d) M2 internal tide. Note the different scales between plots a,b and c,d.

5.4.3 *Energy Flux Ratios in Domains with Varying Eddy Activity*

For the baroclinic energy fluxes defined in Eq. 9 we find that the ratio ζ_{bc} is larger than 1 in the corridor with a larger eddying background and slightly smaller than 1 in the corridor with weak eddy activity. The corresponding values [1] are shown in the first row of table 5 . This implies that in absence of strong eddies the baroclinic energy fluxes are close to balanced, while in presence of strong eddies the baroclinic energy flux increases, which at first seems rather counter-intuitive.

To better understand this relation and also the origin of these energy fluxes, we decompose the velocities and pressure related to the baroclinic energy fluxes into subinertial (related to eddies) and superinertial (related to internal waves) ones, both shown in Fig. 35. From the maps, we observe a larger scale difference between super- and subinertial energy flux. Compared to the total zonal baroclinic energy flux in Fig. 35a, it is clear that the subinertial component dominates. An interesting feature of the superinertial component, are the strong signals in locations which colocate with the Aguhlas rings. In this case, since all superinertial frequencies are included in this component, we assume that they could be near-inertial waves trapped by the anticyclonic eddies, as found eg. in Chen et al. (2023).

---

[1] For each value presented here as well as in table 6 we have repeated the corresponding calculation for the energy flux for three different slightly shifted time-windows within our simulation: 1st-26th, 2nd-27th and 3rd-28th of February. From this, we compute the mean value (presented here) and the corresponding uncertainty $\sigma = \sqrt{\frac{1}{N-1}\sum_{i=1}^{N}(F_i - \bar{F})^2}$. This assumes that the variation between windows is due to noise or sampling uncertainty, not physical changes (which is reasonable for such small shifts). With only 3 samples, this uncertainty estimate is rough but still meaningful.

For the two compontents, we calculate the ratios of outgoing versus incoming energy fluxes across the boundaries of each corridor. In both cases the ratios in the eddy corridors increase, as shown on the second and third row of table 5. The counter-intuitive increase of outgoing energy fluxes in the presence of eddies also remains unchanged. However, this doesn't necessarily mean that that the eddies tend to also increase rather than reduce the M2 internal tide energy flux, since the superinertial velocities and pressure also contain other internal wave frequencies.

Hence, we repeat the analysis for both corridors using only the M2 IT related velocities and pressure (diagnosed using harmonic analysis) in order to quantify the M2 contribution on the superinertial part of the energy fluxes. Figure 35d shows the corresponding map at one depth level and the third row of table 5 shows the corresponding ratios. Here, the EOF based decomposition is performed for the horizontal M2 baroclinic velocities u' and v' as well as for the baroclinic pressure p'_{bc}. Then, we reconstruct the modal velocities and pressure at all timesteps, compute the energy flux as a product of the two and finally the time-mean.

In this case we find that the ratios in both corridors are both very close to 1, implying balanced energy in both domains. Lastly, repeating the analysis for the first (low) and fifth (representative for high) EOF mode of the M2 IT (last row in table 5), we observe that mode 1 M2 fluxes are consistently damped in both corridors, while mode 5 fluxes increase in the eddy corridor, suggesting a strong generation of high modes in the eddy domain. This could imply that some of the incoming energy flux is trapped by the eddies and possibly scattered into high M2 modes. However the pathway of this energy is still unclear and needs to be investigated in more detail.

	no eddies (white box)	eddies (black box)
ζ_{bc}	0.94 ± 0.03	1.16 ± 0.06
ζ_{super}	0.951 ± 0.002	1.03 ± 0.02
ζ_{sub}	0.94 ± 0.04	1.17 ± 0.06
ζ_{M2}	0.98 ± 0.03	1.04 ± 0.04
$\zeta_{\text{mode 1 M2}}$	0.71 ± 0.01	0.82 ± 0.02
$\zeta_{\text{mode 5 M2}}$	0.44 ± 0.01	0.96 ± 0.02

Table 5: Ratios of outgoing versus incoming energy fluxes ζ in the corridor across the two boxes indicated in Fig. 34. Rows indicate the ratios derived for the baroclinic case with all frequencies (first row), the superinertial domain (super, second row), the subinertial domain (sub, thirs row), the M2 internal tide frequency (third row) and the first and fifth EOF mode of the M2 internal tide (last two rows). Ratios are dimensionless.

In general, in the eddy-free box, almost all flux ratios are ~ 1, indicating balance. Mode 1 and 5 are smaller than 1 in both cases. On the other hand, in the eddy-corridor we observe an increase for all energy components, indicating that eddies allow for more energy to leave than enter, which in turn suggests a net energy redistribution, not strong damping.

While the increased total and subinertial baroclinic energy flux in the eddy corridor may reflect eddy-induced redirection, it may also imply an energy transfer from internal tides to the eddy field. Such inverse energy pathways have been proposed in idealized studies and observed in regions with strong eddy–internal tide overlap (Shakespeare, 2023; Cusack et al., 2020).

The most striking increase that we observe is for mode 5. A possible, but still unconfirmed, explanation for this increase can be an eddy-induced scattering. Since the simulation used for this study is not as long as the one used previously, where we could more easily exclude the process of scattering, and since in this simulation the distribution of high modes is very different (see section 5.3), we cannot conclusively answer whether or not eddies scatter low-mode energy into higher mode energy.

Our results, showing enhanced subinertial flux and high-mode internal tide activity, suggest that mesoscale eddies may not only redistribute but extract energy from the internal tide field, contributing to mesoscale energetics.

5.4.4 *Directional Energy Fluxes Along and Across the Eddy Propagation*

To better understand the effect of eddies on the energetics of the area and help interpret our observations, we compute directional fluxes in the eddy-corridor. For this we define an *along* and *across* direction, with the *along* one being parallel to the propagation direction of the Agulhas eddies, ie. from southeast to northwest, and the *across* one being perpendicular to it, ie. from southwest to northeast. Then, we add the outgoing/incoming fluxes along each direction and compute new ratios.

The results of this calculation are presented in table 6. We observe that the ratios along the eddy propagation are almost consistently higher than across it, which reveals that eddies preferentially steer energy along their paths. Especially mode 5 shows a very strong downstream transport, rather than sideways leakage, which suggests that eddies act as directional modulators, guiding wave energy rather than dispersing it. This is consistent to our results from chapter 4, where we used a longer simulation and observed that high modes are trapped and transported downstream by the eddies.

	along eddies	across eddies
ζ_{bc}	1.28 ± 0.12	1.09 ± 0.03
ζ_{super}	1.37 ± 0.12	0.99 ± 0.03
ζ_{sub}	1.27 ± 0.12	1.10 ± 0.03
ζ_{M2}	0.95 ± 0.04	1.04 ± 0.04
$\zeta_{\mathrm{mode\ 1\ M2}}$	1.13 ± 0.12	0.69 ± 0.02
$\zeta_{\mathrm{mode\ 5\ M2}}$	1.85 ± 0.02	0.47 ± 0.02

Table 6: Ratios of directional energy fluxes: along and across the eddy propagation pathway in the eddy-corridor

5.5 SUMMARY AND DISCUSSION OF CHAPTER 5

This chapter is dedicated to the energetics of the Walvis Ridge area, with a specific focus on the potential effects of strong mesoscale eddies on the energetics. A novel simulation was used to more confidently resolve the high-mode waves.
To start with, we looked at the M2 modal distribution and the horizontal structures of these high modes and compared the results to the ones in the previous (coarser resolution) simulation. We observe a larger number of generated high modes in the SMT simulation, with these high-mode signals being significantly stronger than in the R2B9 simulation. While strong horizontal velocity signals, and the corresponding kinetic energy magnitudes, indicate a strong presence of high-mode M2 waves, they do not necessarily reflect energy transport or directionality. In contrast, energy fluxes offer a more complete and dynamically meaningful measure of wave activity, since they incorporate both pressure and velocity perturbations.

Moving to the energetics of the study area, we investigated the role of mesoscale eddies in modulating the baroclinic energy fluxes with a focus on internal tide (IT) energetics, particularly at the M2 frequency and modes 1 and 5. Energy fluxes were computed for full baroclinic signals, subinertial (mainly eddy), superinertial (mainly wave), and harmonically isolated M2 components, including EOF-based decompositions of mode 1 and mode 5. These fluxes were evaluated within two corridors: one strongly influenced by eddies, and one relatively eddy-free. In the eddy corridor, the ratios of outgoing versus incoming total and subinertial energy flux are larger than 1, indicating net energy export, while the eddy-free region showed near-balance. Superinertial and M2 energy flux ratios are also larger than 1 in the eddy domain. Directional decomposition of the fluxes revealed that the enhanced energy fluxes in the eddy region are preferentially aligned with the direction of eddy propagation.

These results indicate that eddies can modulate energy pathways and mode content of the IT in different manners. Two primary and not mutually exclusive interpretations emerge from these preliminary results. The first one is possible eddy-induced scattering and redistribution of high-mode energy along the eddy pathway: the strong increase of mode 5 energy flux in the eddy corridor compared to the reference corridor, accompanied by the strongest directional energy flux increase along the eddy propagation pathway, can indicate that eddies amplify the generation of high modes, potentially due to scattering. The second one is a possible energy transfer from internal tides to the eddy field: the increase of subinertial energy flux in the eddy corridor, which occurs both along and across the eddy pathway, combined with the fact that the modal M2 ratios are less than 1 (indicating more incoming than outgoing energy fluxes, ie. energy dissipation inside the corridor) can suggest that internal tide energy may also be nonlinearly transferred into the subinertial eddy field, as suggested by idealized and observational studies showing internal tide-driven eddy generation or strengthening (Shakespeare, 2023; Cusack et al., 2020). Together, these results hint that both scattering and energy transfer to eddies may co-exist, and that the eddy field acts as both a modulator and participant (gaining energy) in the energetics of the Walvis region.

The nearly conserved or only weakly dissipative M2 fluxes, despite changes in mode structure in both the total and directional energy flux calculation is possibly related to the fact that other modes which we don't consider here, balance the changes in mode 1 and 5, leaving the values for the full M2 energy fluxes unchanged.

Combining the two main sections of this study, we note that the broader spatial distribution and enhanced amplitude of high-mode internal tide velocity observed in section 5.3 are consistent with the energy redistribution patterns diagnosed in our flux analysis. As mentioned above, strong mode 5 horizontal velocity signals, hinting a stronger generation of high modes in the higher resolution run, do not necessarily reflect energy transport or directionality, which energy fluxes do. These interactions are likely underrepresented in coarser simulations, which lack the resolution necessary to capture the shear structures and topographic features that enable effective energy transfer from low to high modes. As a result, the enhanced high-mode activity and redistribution observed here can be understood as a direct consequence of both the eddy dynamics and the simulation's ability to resolve them.

However, we note that with this approach we only track boundary fluxes, not the internal sinks and sources of energy at each corridor. Additionally, with this approach and due to the short length of the simulation, we cannot quantify the temporal change of the energy density, which is a crucial term in the energy equation. Since we only focus on the baroclinic energy fluxes, terms like the barotropic-to baroclinic conversion are also ignored. We consider our method as a spatially integrated, frequency- and mode-resolved energy flux analysis, which is a key piece of the energy budget and can still provide useful insights, but not a complete energy budget, which, given the very high-resolution datasets we are considering, is a very expensive computation. Further limitations of this approach are of course the corridor definitions, as well as the filtering choices. Also the short length of the simulation doesn't allow for a thorough investigation of energy changes.

To overcome the limitations given by the corridor definitions, a next step can be selecting several smaller corridors or boxes, eg. including only one Agulhas ring and then selecting same-size boxes in areas further away from the Agulhas ring. Repeating the analysis on the energy fluxes will give us better statistics. Also, one can include dissipation diagnostics, such as computing the diapycnal mixing rates and/or finescale shear spectra to confirm whether mode-5 energy is lost locally downstream. As a further improvement, the analysis should extend to different modes of the M2 or other internal waves (eg. near-inertial waves, possibly trapped inside eddies, seen in Fig. 35c). In the long term, this analysis can be expanded towards a complete energy budget, by taking into account all the remaining terms.

In this chapter we tried to identify the role of mesoscale eddies in the energetics of the research area, by studying the energy fluxes across regions with strong/weak eddy activity. We find that eddies often increase the ratio of outgoing versus incoming energy fluxes. This increase is mostly happening along the propagation direction of the eddies, especially for mode 5 of the M2 IT. Two possible explanations were presented, with several improvement suggestions for future work.

6

CLOSING THOUGHTS

6.1 SUMMARY AND CONCLUSIONS

In my thesis "*Uncovering the effects of Agulhas eddies on low and high internal tide modes and their energetics in high-resolution ICON*", I studied the effects of mesoscale eddies on the M2 internal tide in the southeast Atlantic using the high-resolution ocean-only general circulation model ICON. In Chapter 1 I motivated my research by posing the overarching question *"How do the eddy-internal tide interactions look like in a realistically simulated ocean?"*. Answering this question does not only improve our current understanding on the eddy-IT interactions themselves, but can also advance our thinking on how to analyze the realistically simulated output from increasingly high resolution models. This divided the initial research question into three separate ones, which were the focus of Chapters 3-5 respectively:

To what extent is the standard normal mode decomposition, derived from linear wave theory, applicable for studying internal tides in a complex, realistically simulated ocean environment and what can we learn from comparing this method with a data-driven one?

I highlighted why the standard modal decomposition method based on linear wave theory might not be most appropriate for our study and proposed a novel decomposition method based on EOF spatial analysis. I compared the results with the ones based on the exact and approximate solutions of the standard method. Finally, I presented the similarities and differences of the methods as well as their implications in the study of eddy-internal tide interactions.

How do Agulhas rings modify the energetics in the Walvis ridge area, especially the energy flux of the internal tide?

I studied the impact of an Agulhas ring on the low and high modes of an M2 internal tide beam using both the novel and the standard decomposition method. The results revealed that for both methods the mode-1 internal tide is refracted and horizontally shifted southward by an Agulhas ring, while its vertical structure remains nearly unchanged. At the same time higher modes can be trapped within Agulhas rings and transported downstream of the eddy propagation pathways. These results indicate on the one hand that the interaction, at least in the Walvis region, does not involve strong nonlinear processes capable of producing waves that are strongly different from those described by linear wave theory. On the other hand, the trapped high modes may arise independently of low-mode scattering.

How do mesoscale eddies influence the energetics in the Walvis ridge area, especially the energy flux of the low-mode internal tide?

I aimed to identify the role of mesoscale eddies on the energetics of the research area by comparing the baroclinic energy fluxes across regions with stronger and weaker eddy activity. I found that across the region with strong eddying background the outgoing energy fluxes are larger than the incoming ones. This increase is mainly happening along the propagation direction of the Agulhas rings, suggesting a downstream energy transport. The large increase of the mode 5 energy flux at M2 frequency is an indication of scattering, while the enhancement of subinertial energy flux suggests that eddies can potentially gain energy.

This work offers a new perspective on eddy-IT interactions looking at them through the magnifying glass of a high-resolution complex GCM. It presents a framework for analyzing internal tides in a fully nonlinear, realistic ocean model without relying on linear wave assumptions. Moreover, it represents a significant step toward a more comprehensive understanding of internal wave dynamics in the presence of mesoscale variability in different seasons.

The novel modal decomposition method based on spatial EOF analysis, which was introduced here to study the M2 internal tidal modes, is capable of successfully capturing the key features of the three-dimensional waves regarding the horizontal and vertical structures as well as extracting their propagating properties without using linear wave assumptions. This makes the EOF method more appropriate for complex model output, which takes into account the spatially varying wave environment. Moreover, this method is computationally more efficient than the standard method, since it does not involve gridpoint-by-gridpoint solving of an eigenvalue problem, which is a big advantage as model resolution and data complexity constantly increase.

The application of the novel decomposition method in the topic of eddy-IT interactions produces results that are more comparable to the ones emerging from in-situ measurements and observations. Their additional similarity to the ones resulting from the standard decomposition method, which is based on linear wave assumptions, indicates the absence of strongly nonlinear processes. No clear example of scattering from low to high modes is found during our simulation periods, contrasting the findings of previous studies based on idealized models.

Seeking answers about whether or not eddies influence the energetics of the Walvis ridge region, I concluded that eddies often tend to increase the baroclinic energy fluxes along their propagation direction. I suggested two possible and not mutually exclusive interpretations. Further analysis is needed to obtain more conclusive results.

6.2 LOOKING AHEAD

In order to obtain a more complete picture of the the eddy-internal tide interactions and quantify their implications to energy dissipation and diapycnal mixing, it is essential to move from a local into a global perspective. As mentioned in Chapter 2, there are several regions worldwide where both oceanic features are strongly present and can possibly interact. A systematic approach, which takes into account all possible interaction sites will surely improve the statistical significance and help quantify the impact of the interactions on reforming the energy spectrum of the ocean.

From a modeling perspective, much longer simulations with equally high (or even higher) horizontal resolution can help quantify the impact of seasonality over several winter/summer periods, while confidently resolving the necessary scales. In a longer simulation, a higher amount of eddy-IT encounters is possible, which will also improve the statistics. Of course, this is a demanding and computationally very expensive task. High-resolution models showcase impressive capabilities, however as mentioned in the Introduction *"all models are wrong, but some are useful"* (Box, 1979). In this context this can also be interpreted as an encouragement for further improvement of theoretical and observational approaches to help completing the puzzle.

From a theoretical perspective, a crucial limitation of deeply understanding these interactions is the current lack of a coherent theoretical framework that clarifies the mechanisms through which eddies affect the dissipation of internal tides. Future theoretical work should aim to not only assume stationary backgrounds, WKB and linear wave–mean interactions or small eddy amplitudes, but rather try to explicitly capture both scattering and energy exchange processes between internal tides and evolving eddy fields, and link them to the spatial and modal structure of dissipation.

From an observational perspective, expanding research vessel campaigns, in-situ measurements, mooring deployment, satellite altimetry missions, eg. the SWOT mission, coordinated multi-platform measurement strategies and a combination of remote sensing with autonomous instruments, like gliders or Argo floats is essential to provide more detailed spatial and temporal information on both internal tides and mesoscale eddies. This information is currently limited due to the sparse observational data available. These data serve not only for validating and informing the models but also for providing constraints necessary to refine theoretical frameworks.

If and when the physical oceanography research community succeeds to establish one comprehensive framework for the eddy-internal tide interactions, incorporating all possible approaches, we can claim to understand the consequences of the eddy-IT interactions vastly better than before. With these important insights, we can include these dynamics into climate model parameterizations to make them more energy-consistent and improve their predictive capabilities. This thesis contributes a small piece to this puzzle: by highlighting the need for analysis techniques appropriate for complex model output ; identifying the main effects of mesoscale eddies on low and high modes of the M2 internal tide ; and revealing possible pathways of energy transport due to these interactions. Cheers.

TOOLS

The work for this dissertation heavily relied on open source software, some of which I would like to acknowledge explicitly:

- I primarily employed `Python` [1], with extensive use of the `numpy` [2], `xarray` [3] and `matplotlib` [4] packages.
- I employed CDO [5] to process large amounts of output efficiently, which is especially helpful for working with ICON output.
- ChatGPT [6] was utilized for improving the efficiency of my code and for linguistic purposes in the writing process, such as refining sentence structures and translation.
- This thesis was typeset using the `classicthesis` template developed by Andre Miede and Ivo Pletikosić [7].

---

[1] "Python Software Foundation", 2020, version 3.9, *python.org*

[2] "Array programming with NumPy." Harris Charles R. et al. Sept. 2020, (`https://doi.org/10.1038/s41586-020-2649-2.`)

[3] "xarray: N-D labeled Arrays and Datasets in Python", Hoyer Stephan and Joe Hamman Apr. 2017, `10.5334/jors.148.`

[4] "Matplotlib: A 2D graphics environment", Hunter, J. D. ,2007, (`10.1109/MCSE.2007.55.`)

[5] "CDO User Manual", Uwe Schulzweida, 2023, (`https://doi.org/10.5281/zenodo.10020800`)

[6] "ChatGPT: A Large-Scale Generative Model for Open-Domain Chat", OpenAI 2021, Ver- sion 3.5., (`https://github.com/openai/gpt-3.`)

[7] "classicthesis" template, A.Miede and I.Pletikosić, (`https://bitbucket.org/amiede/classicthesis/`)

APPENDIX

A

The attached manuscript is submitted in *Journal of Physical Oceanography*.

Kourkouraidou, Zoi, von Storch, Jin-Song, "The M2 internal tide and its interaction with eddies in the Walvis ridge area simulated by a 5km O-GCM".

AUTHOR CONTRIBUTIONS: Z.K. performed the simulations and data analysis, created the figures and drafted the manuscript. JS.vS. designed the research question, supported analysis and provided scientific guidance. Both authors contributed to editing and revising the manuscript.

The M2 internal tide and its interaction with eddies in the Walvis ridge area simulated by a 5km O-GCM

Zoi Kourkouraidou[1,2,3], Jin-Song von Storch [1,3]

[1] Max Planck Institute for Meteorology, Max Planck Society, Hamburg, Germany
[2] International Max Planck Research School for Earth System Modelling, Max Planck Society, Hamburg, Germany
[3] Universität Hamburg, Hamburg, Germany

ABSTRACT

The interaction between internal tides (IT) and mesoscale eddies, particularly their role in energy dissipation of low-mode IT via scattering by eddies, remains poorly understood. Using the ocean-only ICON model at 5 km resolution, we investigate these interactions near the Walvis Ridge. To extract IT modes, we apply both linear wave theory and a data-driven empirical orthogonal function (EOF) method. The latter does not rely on linear wave assumptions and is capable of identifying features resulting from nonlinear processes simulated by ICON. Despite methodological differences, both methods lead to similar results: the impact of an Agulhas ring that crosses a beam of M2 mode-1 IT is identified as a refraction of the beam, characterized by a southward shift of the beam and an essentially unchanged vertical structure, indicating that the Agulhas ring does not scatter the mode-1 IT into higher modes. Additionally, higher IT modes are found to be trapped within Agulhas rings before interacting with mode-1 beams, implying that they do not arise from interaction between the mode 1 beam with the Agulhas rings. The comparable outcomes from both approaches imply a limited influence of nonlinear effects. This study offers new insights into IT-eddy interactions in a realistic setting and introduces a framework for analyzing internal tides beyond linear wave assumptions.

A.1 INTRODUCTION

Internal tides (ITs) are internal gravity waves (IGWs) at tidal frequencies generated when ocean tidal currents impact rough topography, forcing stratified water to oscillate vertically (Garrett and Kunze, 2007). Diapycnal mixing induced by breaking of ITs contributes significantly to sustaining the global overturning circulation. In fact it was previously estimated to contribute with roughly 1 TW, which is approximately 50% of the total energy needed to sustain the circulation (Munk and Wunsch, 1998; Ferrari and Wunsch, 2009). The biggest part of the IT energy is carried by the low modes. The fate of these low modes and of the corresponding energy is not yet fully understood and will be addressed in this study. The lowest mode has horizontal scales of approximately 100 km and can propagate and be tracked for O(1000) km away from their generation site, as suggested by IT signatures extracted from altimetry (Ray and Mitchum, 1997; Zhao and Alford, 2009; Zhao et al., 2011; Cummins, Cherniawsky, and Foreman, 2001) in several regions worldwide. The higher modes, in contrast, have smaller vertical scales and larger vertical shear (Simmons and Alford., 2012), thus are more unstable and prone to break, thereby causing mixing near the generation sites (Vic, Naveira Garabato, and Green, 2019). The fate of low-mode ITs however, especially how they dissipate their energy, is not completely clear. There exist several processes that can lead to dissipation of low-mode ITs. Here we mention the most dominant ones. One is the interaction with topography, which has been the focus of several studies, using both numerical simulations (Johnston and Merrifield, 2003; Buijsman et al., 2020) and observational data (Klymak, Pinkel, and Rainville, 2008). The other is wave-wave interaction. For example non-linear interactions can transfer energy via the parametric subharmonic instability (MacKinnon et al., 2013) to subharmonic frequencies and higher wavenumbers near the critical latitude. Yet another process is the interaction between ITs and mesoscale eddies. Evidence suggesting IT-eddy interactions has been found from direct observations (Löb et al., 2020; Huang et al., 2018; Cusack et al., 2020). However, observations are still too sparse in time and space to be sufficient for describing the details of the interactions. To get more insight into this process, theoretical and numerical approaches have been considered. An example of a theoretical approach is the study by Savva, Kafiabad, and Vanneste (2021a) where the effect of geostrophically balanced turbulent flows on internal gravity waves is examined using a kinetic equation that governs the evolution of internal gravity wave energy density under certain assumptions about the quasi-geostrophic flows. Several studies have been carried out following numerical approaches (Dunphy et al., 2017; Dunphy and Lamb, 2014; Wang and Legg, 2023). There, the wave-eddy interaction is examined using a general circulation model configured for idealized conditions.

Recently, the process, in that an eddy scatters an incident low-mode IT into high modes with higher wavenumbers, has drawn attention of several researchers. This process has a great physical significance, as it produces a possible dissipation pathway of the low-mode IT. Dunphy and Lamb (2014) show in an idealized configuration that baroclinic eddies can scatter a portion of the incident wave to higher vertical modes with higher wavenumbers and energy is transferred from low modes to high modes through the IT–eddy interaction. Wang and Legg (2025) show that

Agulhas rings serve as hotspots for internal tide dissipation. By quantifying the internal tide dissipation using model simulations and estimating dissipation rate from Argo floats, they suggest that the enhanced dissipation inside Agulhas rings is due to the transfer of internal tide energy from stable low wave numbers to less stable high wave numbers. However, it remains still unclear how exactly this scattering process occurs in a realistic setting. Do the high modes trapped inside an eddy, as reported by several previous studies, indeed result from the scattering of a low mode IT beam?

This paper extends the previous numerical studies on the effect of mesoscale eddies on ITs. Our approach differs from the previous numerical studies with respect to the following two aspects. First, we consider realistic simulations performed with the newly developed ocean GCM *ICON-O* (Korn, 2017; Korn et al., 2022) at a horizontal resolution of 5 km forced by surface fluxes derived from the ERA5 reanalysis (Hersbach et al., 2020). This means that the background wave environment, i.e. stratification, eddying circulation, and bottom topography, in which the wave-eddy interaction takes place, is realistic. This also means that the way how ITs encounter eddies is realistic. In particular, as will be explain later, we consider the situation where a wave beam is naturally crossed by a *travelling* eddy, rather than the situation where an incident IT made to artificially encounter a *stationary* eddy at a fixed location. Secondly, we explicitly identify the low and high modes and the eddies. By doing so, we hope to find out whether the high modes trapped in an eddy result from scattering of which low mode. With these differences in mind, we aim to quantify a) the general properties of the ITs, including their seasonality, as they are simulated by our GCM, and b) the impact of eddies on the low-mode internal tides, especially the significance of the scattering process and the relevance of other processes, such as refraction.

In order to achieve these objectives, we need an adequate method, by which an IT can be decomposed into low and high modes. The standard approach is to perform a vertical mode decomposition by solving the Sturm-Liouville equation derived from linear wave theory (Gill, 1982; D.Olbers, C.Eden, and J.Willebrand, 2012; Gerkema and Zimmerman, 2008). However, this approach relies on assumptions, which may not be appropriate for studying non-linear interactions between eddies and ITs. To circumvent this problem, we develop a new decomposition method, by which the structures of ITs are empirically extracted from the model output without imposing any assumptions needed to derive linear wave theory. Furthermore, by comparing the result obtained from the standard method with our new method, the degree by which the non-linear interactions between eddies and ITs alter the structures of ITs can be assessed. In particular, in case the two methods produce comparable results, the compatibility could indicate a minor role of non-linear processes in altering the wave structures obtained from linear wave theory.

The structure of the paper is the following. In section A.2 we describe the ICON-O tidal model and the experimental set-up, the area of the focus of our analysis, and the IT environment simulated by the model. Section A.3 describes the methodology used to diagnose the M2 IT and to decompose an IT into modes with different vertical structures, and the strategy used to quantify the energy dissipation caused by wave-eddy interaction. There we discuss the methodological differences between our method and the standard modal decomposition method by formulating them is a comparable manner. In section A.4, the properties of M2 IT in ICON-O are diagnosed, the effect of mesoscale eddies on the different modes of the M2 IT are quantified. Also included in section A.4 is a comparison of the two decomposition methods. A summary is provided in section A.5.

A.2 ICON-O MODEL AND THE AREA OF FOCUS SIMULATED BY ICON-O

A.2.1 *ICON-O and Experimental Set-up*

The general circulation model used in this study is ICON-O (Korn, 2017; Korn, 2018; Korn et al., 2022), a primitive equation global ocean model recently developed at the Max-Planck-Institute for Meteorology. The model can be run with tides by enabling the luni-solar tidal potential in the momentum equation. ICON-O without being constrained by observations is able to realistically simulate the major features of barotropic tides (von Storch et al., 2023). In this study, we use the R2B9 grid, corresponding to a horizontal resolution of about 5 km globally. Some features of the R2B9 ICON-O coupled to the atmospheric component ICON-A at the same R2B9 grid can be found in Hohenegger et al. (2023), Gutjahr et al. (2022), and von Storch and Lüschow (2023). In the vertical, the z^* coordinate introduced by Adcroft and Campin (2004) is used. The vertical resolution is defined by 128 vertical levels and gradually varies between less than 10m in the upper 140m and 200m below 4544m of the water column. The parameterizations of mesoscale eddies, expressed as eddy induced diffusion and eddy induced advection, are deactivated. The turbulent vertical mixing is parameterized following Gaspar, Yves, and Lefevre (1990). ICON-O incorporates a sea ice model consisting of dynamic and thermodynamic component.

To study the IT - eddy interactions, we need a global ocean which is spun up and possesses a quasi-stationary eddy field. We do so by first performing a spin-up run. This run starts from an ocean state at rest with a 3-dimensional temperature and salinity distribution interpreted from the Polar Science Center Hydrographic Climatology (Steele, Morley, and Ermold, 2001). The model is then forced by fluxes of momentum, heat and fresh water diagnosed from ERA5 reanalysis, as described in Korn et al. (2022) and integrated over the period from 2010 to 2021. The globally averaged kinetic energy becomes essentially stationary after ≈ 2 years (not shown). Starting from the end state in 2021, ICON-O is then forced not only by surface fluxes but also by the lunisolar tidal forcing for about ≈ 1.5 years. This run forms the basis of the present study.

A.2.2 *The Area of Focus: the Internal Tide Generated at the Walvis Ridge and Agulhas Rings*

Seen from a global perspective, there is a small number of regions suitable for studying interactions between internal tides and eddies. These are regions where mesoscale eddies and strong internal tides coexist, among them the Walvis ridge area in the south-east Atlantic, the Tasman sea, the west of Madagascar, and the Kuroshio current area. We focus on the southeast Atlantic, where Agulhas Rings shed by the retroflection of the Agulhas currrent travel from the waters around the southern tip of the African continent northwestward and cross beams of internal tides generated at and emitted from the Walvis Ridge. These beams have been identified both using semi-analytical solutions (Garrett and Kunze, 2007; Nycander, 2005), numerical simulations (**i2020**) and Argo floats (Wang and Legg, 2025).

A typical situation in this region is depicted in figure A.1, which shows M2 IT u' (derivation in section A.3) at approximately 100 m depth obtained at one time instance, together with Aguhlas Rings. There are several beams of M2 IT, indicated by the trains with positive (red) and negative (blue) internal tide zonal velocity, which radiate from the Walvis Ridge. The propagation direction of the beams is shown by the purple arrows, which indicate the M2 energy flux averaged over the first month of our simulation (derivation in section A.3).

Agulhas rings (indicated by the black contours of the current velocity) propagate northwestward and cross the IT beams southeast of the ridge. A particular IT beam, the one that is generated at the Walvis Ridge near 32.45°S and propagates mostly zonally toward the African coast, can be most easily crossed by an Agulhas ring. Moreover, due to the reflection on the continental shelf (at around 14°E), the position of this beam appears to be rather stationary throughout the simulation period. Hereafter, we will focus on this particular beam. The effect of eddies on ITs will be studied by quantifying how Agulhas rings alter this beam. The effects of the ITs on the eddies will not be studied in this paper. There is another beam south of our beam at about 32.45°S. Although somewhat stronger, this beam is not considered, since the Agulhas rings tend to cross this beam further downstream near the end of the beam, leaving little room for quantifying the effect of Agulhas rings on this beam.

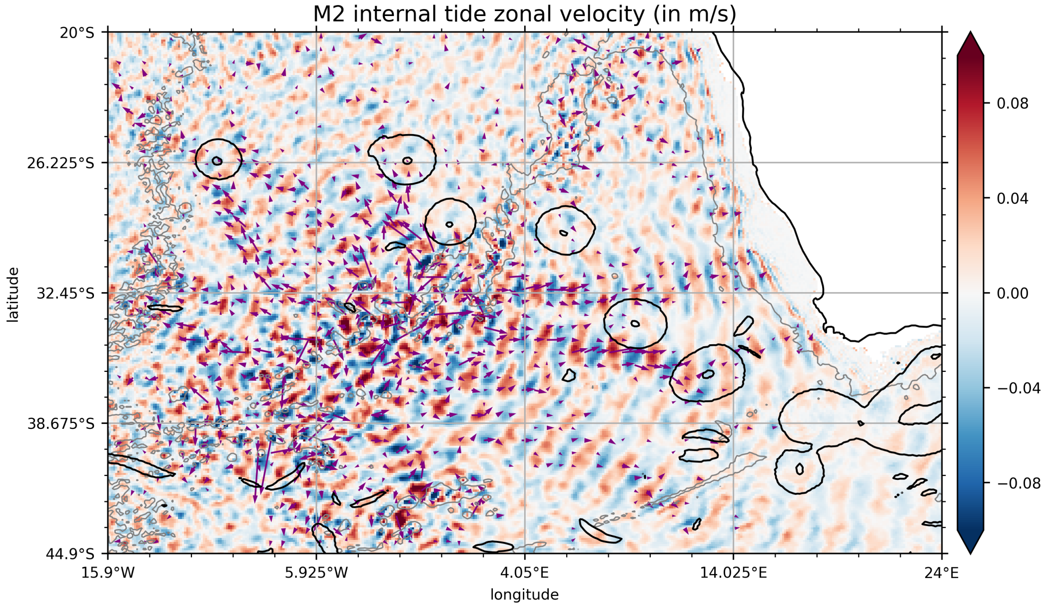

Figure A.1: A snapshot of the M2 internal tide zonal velocity (in m/s, colour shadings) at ca. 100m depth, together with topography at around 2500m depth (grey lines) and Agulhas Rings (black contours) simulated by ICON-O. The Agulhas Rings are described by the mean horizontal current speed (in m/s) and plotted here with a contour level at 0.4. Purple arrows indicate the baroclinic energy flux (in W/m^2) at M2 frequency.

The M2 IT zonal velocity (derivation in section A.3) shown in Figure A.1 is closely linked to the topography, here the Walvis Ridge. The waves propagate along beams away from the ridge, shown by the energy flux arrows. The wave amplitudes are stronger when they are close to the generation site and weaken the further away they propagate, possibly due to dissipation or redistribution of the energy. In some areas along the continental coast we observe slightly stronger values, which can be caused by reflection at the coast and subsequent constructive interference between the incoming and the reflected beam. Furthermore, we observe that the horizontal wavelength of the waves is spatially varying and doesn't remain constant across the complete region of interest, thus the diagnosed internal tidal waves are not plane waves.

In order to properly identify the influence of Agulhas rings on the ITs, we compare ITs at a time when they are not in contact with an Agulhas ring with ITs at a time when they are in contact with an Agulhas ring. Finding such cases from high frequency output of a high-resolution GCM simulation is a challenging task. The difficulty originates from the different timescales of the M2 internal tide and the Agulhas Rings, with the timescales of the latter being much longer than the tidal period. This causes on the one hand the need of high-frequency output to properly resolve and describe the M2 internal tide, which in turn increases the data size and space storage. Previous studies using numerical models (Li, Storch, and Mueller, 2015; Li and Storch, 2020) and Argo floats (Wang et al., 2023; Hennon, Riser, and Alford, 2014) suggest that hourly output is a good choice. On the other hand, Agulhas rings remain predominantly stationary throughout the M2 period and exhibit minimal movement over time intervals shorter than a week. Hence, daily data are sufficient to describe their propagation. Since we are unable to store hourly 3-dimensional fields for the entire simulation period of 1.5 years, due to the limited storage capacity, the following procedure is developed to overcome the storage problem.

We first run the whole simulation with daily output, thereby store the instantaneous 3-dimensional ocean state at the beginning of every month. These states serve as initial states to be used to rerun the model with hourly output over short designated time periods. We consider two pairs of one-month periods, each consisting of a month with and a month without Aguhlas Ring on the considered tidal beam. The first pair consists of February and March of 2022, and the second consists of June and July of 2022. For both pairs, the first month— February and June— are the months without an Aguhlas Ring, and the second month —March and July — are the months with an Agulhas Ring. These months are identified by following the propagation of Agulhas rings using animations of horizontal current velocity over the whole simulation of 1.5 years. During the first month of a pair, our particular beam is free or almost free of any Agulhas rings. During the second month of a pair, there is an Agulhas ring crossing our beam. The hourly output of the four months is regridded from the unstructured ICON grid onto an $1/10^{\circ}$ longitude-latitude grid to reduce the overall data size and speed up the post-processing. We recognize that regridding results in the loss of fine-scale details and reduces accuracy for small-scale phenomena. However, this is acceptable for our purposes, as we are primarily focused on low-mode internal tides and mesoscale eddies, which have horizontal scales of approximately 100 km.

A.2.3 *The Wave Environment*

This subsection describes the main features of the wave environment in our area of focus. These include the bathymetry shown in Figure A.2, the mean circulation shown in Figure A.3, and the mean stratification shown in Figure A.4. Both the bathymetry and the mean circulation reveal strong and complex spatial dependence, with the latter being characterized by Agulhas rings aligning from the Agulhas retroflection toward the Walvis Ridge. Agulhas rings are some of the strongest mesoscale eddies globally (Laxenaire et al., 2018).

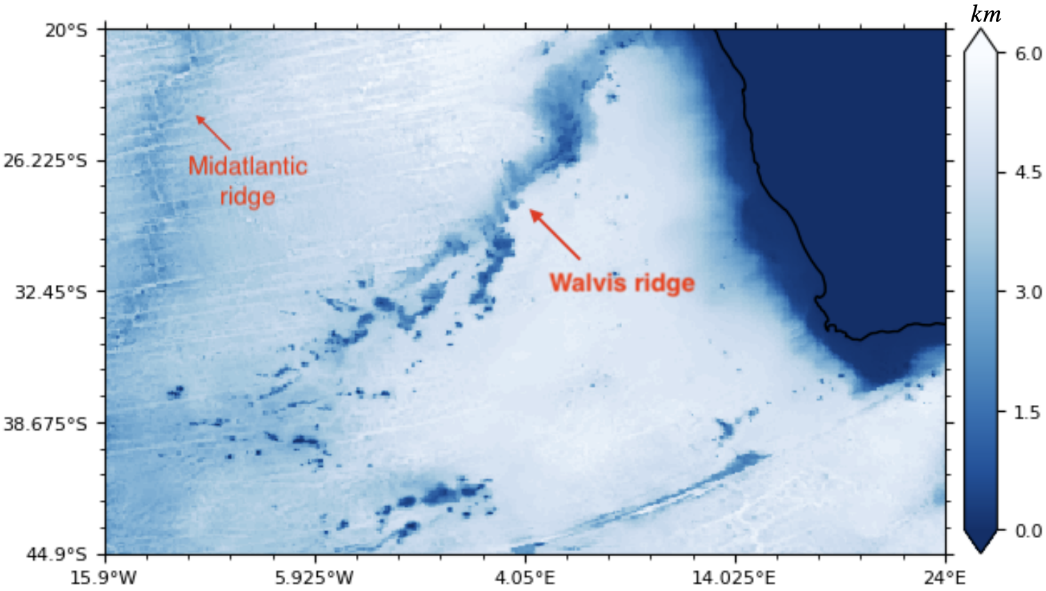

Figure A.2: Topography of the research area in the southeast Atlantic.

An Agulhas ring, as described by the composites in Figure A.5, is characterized by a velocity minimum at the center of the ring. The mean radius of the rings is about 115 km. At 100 m depth, the maximum velocity reaches nearly 1 m/s at the northern rim of the rings. All simulated rings are anticyclonic, surface intensified, and essentially confined in the upper 500 m. Their propagation speed is roughly estimated to be $0.1 m/s$.

The mean stratification varies horizontally and vertically, introducing a further complexity into the wave environment. These variations can influence the generation, propagation, energy dissipation of the waves, as well as the interaction of waves with the surrounding fluid medium. The mean stratification varies not only spatially but also with the season. We observe weaker stratification during the winter in June-July 2022 than during the late summer in Febuary-March 2022. In particular, N at a depth of about 70 m is about one order of magnitude weaker in winter than in summer in the southern part of the domain. In the vertical, the maximum of N is smaller and located deeper in winter than in summer. This is expected, as insolation is stronger, and winds, and with that the vertical mixing, are weaker in summer than in winter.

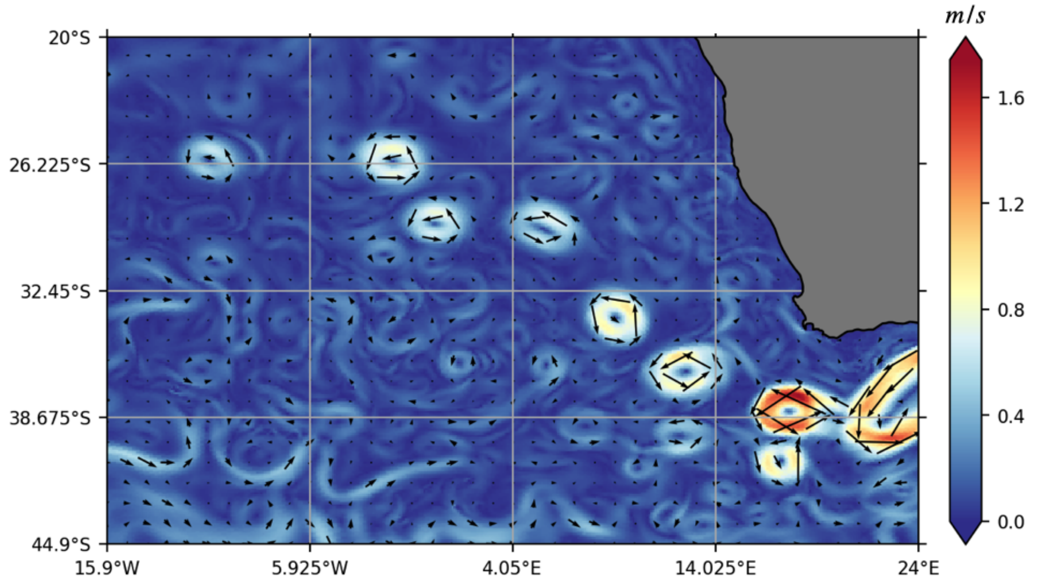

Figure A.3: Mean horizontal current speed during late summer in February 2022 at about 50m depth.

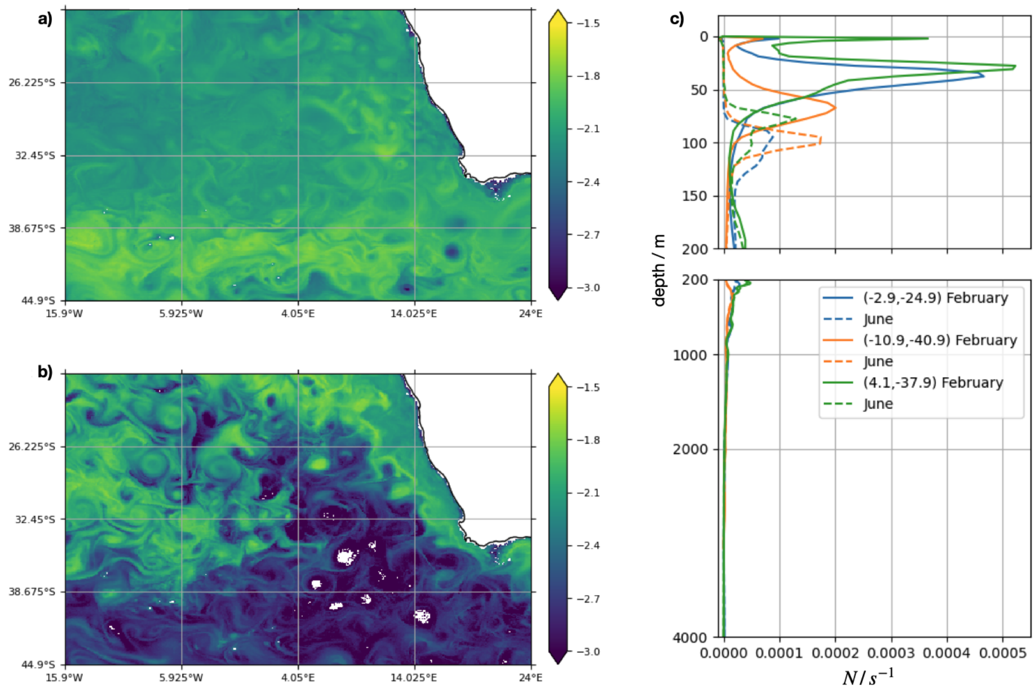

Figure A.4: Mean stratification, as described by the Brunt-Väisäla frequency N in logarithmic scale ($\log_{10} N$) at about 70 m for a) February and b) June 2022, and as c) vertical profiles of N^2 at three grid points for February (full lines) and June (dashed lines). N is derived from mean temperature and salinity in the respective month.

A.3 METHODOLOGY

A.3.1 *M2 Internal Tide in ICON-O*

To study the interaction of internal tides with eddies, we need to first identify the internal tide simulated by the ICON-O model. This is done by first calculating the baroclinic horizontal velocity $\mathbf{u}'$ from the full horizontal velocity $\mathbf{u} = (u, v)$ as

$$\mathbf{u}' = \mathbf{u} - \mathbf{U} \quad \text{with} \quad \mathbf{U} = \frac{1}{\eta + d} \int_d^{\eta} \mathbf{u}(x, y, z, t)\, dz \tag{A.1}$$

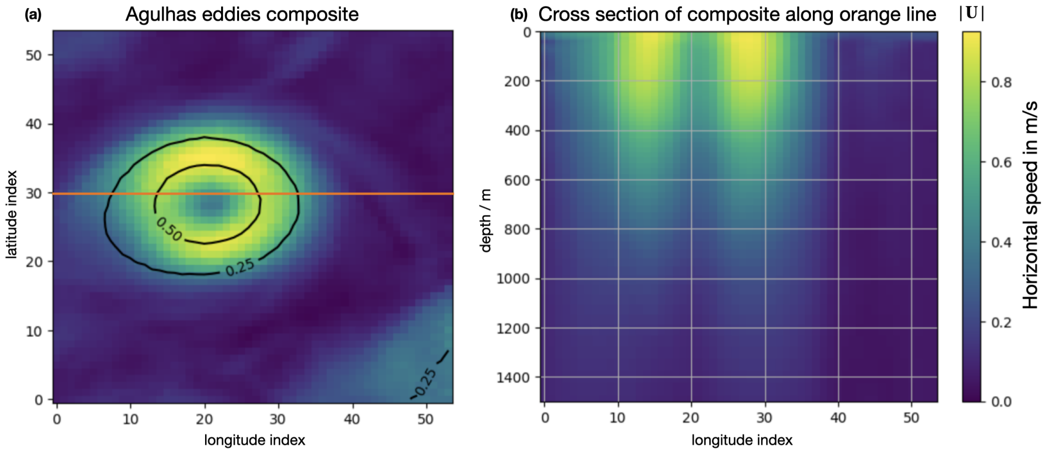

Figure A.5: Composites of a) horizontal current speed in m/s at 100 m (color shadings) and sea surface height in m (black contours) and b) current speed as a function of depth along the red line shown in a). The composites are obtained by averaging over the five largest Agulhas rings found in the 1.5 year long simulation.

where η is the surface elevation and d the bottom depth. The baroclinic velocity $\mathbf{u}'_{bcl}$ contains motions at all possible frequencies. We then apply harmonic analysis (Foreman, Cherniawsky, and Ballatyne, 2008) to $\mathbf{u}'_{bcl}$ at each grid point (x, y, z) to get the amplitudes $A(x, y, z)$ and phases $\phi(x, y, z)$ for different constituents of the internal tide at that grid point. The analysis is done for hourly data within one month. Below, we focus on the M2 internal tide. The full M2 internal tide zonal velocity is then given by (dropping the subscript M2)

$$\begin{aligned} u'(x,y,z,t) &= \mathbb{R}e\Big(A(x,y,z)e^{i(\omega t-\phi(x,y,z))}\Big) \\ &= A(x,y,z)\Big(\cos(\phi(x,y,z))\cos(\omega t)+\sin(\phi(x,y,z))\sin(\omega t)\Big) \\ &= C(x,y,z)\cos(\omega t)+S(x,y,z)\sin(\omega t) \end{aligned} \tag{A.2}$$

with

$$C(x,y,z) = A(x,y,z)\cos(\phi(x,y,z)), \quad S(x,y,z) = A(x,y,z)\sin(\phi(x,y,z)), \tag{A.3}$$

where $\mathbb{R}e(\cdot)$ indicates the real part of its argument, ω is the M2 angular frequency. A similar expression is obtained for the meridional velocity v'.

Harmonic analysis, while useful for identifying the frequency components of internal tides, does not reveal the nature of the wave — such as whether it propagates horizontally, vertically, or in a more complex manner in three-dimensional space. To understand the propagation characteristics of internal tides, one must examine the phase function ϕ as it varies with spatial coordinates.

If the phase ϕ depends solely on horizontal coordinates, for example $\phi = kx + ly$, where k and l represent the zonal and meridional angular wave numbers respectively, then the internal tide described by Eq. (A.2) corresponds to a horizontally propagating wave. In this case, the direction of propagation aligns with the horizontal wave vector (k, l). Conversely, if ϕ is a function only of the vertical coordinate, such as $\phi = mz$, with m being the vertical angular wave number, then the internal tide described by Eq. (A.2) represents a vertically propagating wave.

Generally and especially for short waves, the phase may depend on both horizontal and vertical components, indicating oblique wave propagation. Long waves, such as those simulated by the primitive-equation ICON model, are well described by vertically standing waves. In this case, the part of ϕ that depends on z does not contributes to the complex wave form and can be absorbed in amplitude A. The first line of Eq.(A.2) reduces to $\mathbb{R}e\Big(A(x,y,z)e^{i(\omega t-\phi(x,y))}\Big)$, describing a horizontally propagating wave with either a fixed or spatially varying vertical structure. The horizontal propagation is in the direction of the horizontal wave number vector (k,l), which can be described by horizontal gradients of ϕ, with $k=\partial\phi/\partial x$ and $l=\partial\phi/\partial y$.

To assess how an Agulhas ring influences a propagating low-mode internal tide, it is essential to quantify the mode's 3-dimensional structures, both before and after the mode encountering an Agulhas ring. This calls for a decomposition method that not only identifies the vertical structure of a mode but also quantifies the horizontal dependence of the phase ϕ of the mode.

A.3.2 *Mode Decomposition*

The standard method for modal decomposition (Gill, 1982; D.Olbers, C.Eden, and J.Willebrand, 2012; Gerkema and Zimmerman, 2008) is based on the linear wave theory, which describes the vertical structure of linear internal wave solutions in terms of eigenfunctions of the Sturm-Liouville (SL) equation

$$\frac{d}{dz}\Big(\frac{1}{N^2(z)}\frac{d}{dz}a(z)\Big)=\chi\, a(z). \tag{A.4}$$

At each horizontal grid point (x_0,y_0), the SL eigenvalue problem is solved using the local stratification profile and water depth, yielding a discrete set of eigenfunctions $a_n(z)$ and associated eigenvalues χ_n. A modal decomposition is then performed by projecting the internal tide velocity u'—or its time-independent components C and S—onto these vertical eigenfunctions. The projection of u' onto the n-the eigenfunction $a_n(z)$ defines the velocity field of the n-th mode:

$$u'_n(x,y,z,t)=a_n(z)\,\beta_n(x,y,t), \tag{A.5}$$

where the modal amplitude β_n is a time series given by:

$$\beta_n(x,y,t)=\sum_z a_n(z)u'(x,y,z,t). \tag{A.6}$$

By collecting β_n across all horizontal locations, one can reconstruct the full 3D structure of the n-th mode over the analysis domain.

Alternatively, the n-th mode can be represented using the modal components c_n and s_n of C and S respectively as

$$u'_n(z,x_0,y_0,t)=a_n(z)\left[c_n(x_0,y_0)\cos(\omega t)+s_n(x_0,y_0)\sin(\omega t)\right], \tag{A.7}$$

with time-independent modal coefficients

$$c_n(x_0,y_0)=\sum_z a_n(z)C(x_0,y_0,z),\quad s_n(x_0,y_0)=\sum_z a_n(z)S(x_0,y_0,z). \tag{A.8}$$

While Eq.(A.5) and Eq. (A.7) are formally equivalent, an IT is reconstructed using time-independent coefficients c_n and s_n Eq.(A.7), but using a time series β in Eq.(A.5).

At first glance, Eq.(A.7) suggests that each mode may represent a horizontally propagating wave with a well-defined vertical structure. However, neither Eq.(A.5) nor Eq. (A.7) provides direct information about the mode's horizontal propagation. Being calculated using local stratification and local depth, the n-th eigenfunction $a_n(z)$ vary from grid point to grid point. While this variation may reflect topographically induced horizontal variations in vertical structure, it complicates the interpretation of low modes. A low mode propagates over thousands of kilometers. Characterizing its 3-dimensional properties requires identifying its vertical structure at all grid points along its propagation path, which is highly impractical.

Regarding horizontal propagation, the linear dispersion relation:

$$k^2 + l^2 = \chi_n(\omega^2 - f^2), \tag{A.9}$$

relates the magnitude of the horizontal wavenumber vector (k, l) to the vertical eigenvalue χ_n, tidal frequency ω, and Coriolis parameter f. However, this relation only constrains the magnitude—not the individual components—of the horizontal wavenumber vector, and thus offers no insight into the direction of wave propagation.

An intuitive attempt to extract phase information is to rewrite Eq. (A.7) as:

$$u'_n(z, x_0, y_0, t) = a_n(z)\beta\left[\cos(\phi)\cos(\omega t) + \sin(\phi)\sin(\omega t)\right], \tag{A.10}$$

where $\beta = \sqrt{c_n^2 + s_n^2}$ and $\phi = \arccos(c_n/\beta)$. Assuming a plane wave form for the phase, such as $\phi = kx + ly$, one might estimate k and l by taking horizontal derivatives of ϕ. While such gradients can formally be computed, they are not physically meaningful, since ϕ lacks spatial coherence due to the independence between solutions of Sturm–Liouville equations at different grid points.

In summary, while the standard SL method successfully separates modes according to their vertical structures, it does not provide any information about the horizontal propagation of these modes, thereby limiting our ability to accurately and concisely quantify propagation properties of the modes, especially those of the low modes.

This motivates us to consider a new modal decomposition based on EOF analysis, a well-known method used to extract structures that maximize the total variance in a high-dimensional data set (Thomson and Emery, 2014; Storch and Zwiers, 1999). Different from the usual practice, which considers the variance with respect to time and a covariance matrix describing the spatial covariability averaged over time, we consider the variance with respect to depth and a covariance matrix that describes horizontal covariability averaged over depth. To avoid the land points associated with topographic features in the deep ocean, only data in the upper $\sim$ 4000 m are used. Since trends can deteriorate the result of an EOF analysis, the linear tendency for velocity magnitude to decrease with increasing depth is removed prior to the EOF analysis. The EOF analysis is performed for the vector consisting of $C(x, y, z)$ and $S(x, y, z)$ in Eq.(A.2).

The EOFs, e_n with $n = 1, 2, \cdots$, are eigenvectors of the covariance matrix. Each eigenvector consists of two parts,

$$e_n(x, y) = \begin{pmatrix} e^c_n(x, y) \\ e^s_n(x, y) \end{pmatrix}, \tag{A.11}$$

corresponding to $C(x, y, z)$ and $S(x, y, z)$ in Eq.(A.2), respectively. Both e^c_n and e^s_n are functions of horizontal coordinates x and y. The principle component (PC) α_n associated to the n-th EOF e_n is a function of the depth z. It is obtained by projecting the vector consisting of $C(x, y, z)$ and $S(x, y, z)$ on to $e_n(x, y)$,

$$\alpha_n(z) = \nu \sum_{x,y} \Big(e^c_n(x, y) C(x, y, z) + e^s_n(x, y) S(x, y, z)) \Big), \tag{A.12}$$

where $\sum_{x,y}$ indicates the summation over all grid points (x, y) at depth z. The normalization factor ν is defined such that the amplitude of the n-th EOF mode is determined by the EOF patterns, e^c_n and e^s_n.

Using the n-th EOF and its associated PC, the velocity of the n-th EOF mode is given by

$$u'_n(x, y, z, t) = \alpha_n(z) \Big(e^c_n(x, y) \cos(\omega t) + e^s_n(x, y) \sin(\omega t) \Big). \tag{A.13}$$

As time progresses, $\sin(\omega t)$ reaches its maximum a quarter of wave period later than $\cos(\omega t)$, and with that, the pattern described by e^s_n occurs a quarter of wave period later than that described by e^c_n. The n-th EOF mode can be equivalently described by

$$u'_n(x, y, z, t) = \alpha_n(z) A_n \Big(\cos(\phi_n) \cos(\omega t) + \sin(\phi_n) \sin(\omega t) \Big) \tag{A.14}$$

with amplitude

$$A^2_n = \big(e^c_n(x, y) \big)^2 + \big(e^s_n(x, y) \big)^2 \tag{A.15}$$

and phase

$$\phi_n(x, y) = \arccos \left(\frac{e^c_n(x, y)}{A_n} \right). \tag{A.16}$$

Different from ϕ in Eq.(A.10), ϕ_n in Eq.(A.14) is a function of horizontal coordinates, x and y. As such, spatial differentiation is a well-defined operation. By assuming $\phi_n \simeq k_n x + l_n y$, the horizontal angular wave number k_n and l_n can be obtained from

$$k_n = \frac{\partial \phi_n}{\partial x}, \;\; l_n = \frac{\partial \phi_n}{\partial y}. \tag{A.17}$$

The associated horizontal wavelength is then given by

$$L_n = \frac{2\pi}{\sqrt{k^2_n + l^2_n}}. \tag{A.18}$$

Both the amplitude and the direction of the wave number vector (k_n, l_n) can vary horizontally. This variation can be interpreted as resulting from linear or non-linear interaction of internal tides with its environment as simulated by the ICON model.

Since the EOF analysis aims at maximizing the total variance with respect to the vertical coordinate, it is not clear whether it can capture the wave properties imprinted in the full internal tide velocity u' prior the EOF analysis. We show below that this is the case. Fig.A.6a depicts the characteristic associated with the horizontal propagation that u' at one time is 90° out of phase with u' a quarter of period later: The maxima and minima (red and blue shadings) at one time are replaced by zeros (thick black lines) a quarter of period later. Fig.A.6b shows that this feature is captured by the mode-1 velocity reconstructed according to Eq.(A.13). A similar picture is obtained for the meridional velocity (not shown). Fig.A.7a depicts the other property that zonal and meridional internal tide velocity, u' and v', are 90° out of phase. Fig.A.7b shows that this property is also retained by the mode-1 obtained from the EOF modal decomposition. Fig.A.6 and Fig.A.7 also show the full velocities are dominated by mode-1 velocities.

In summary, the EOF decomposition captures the basic wave properties in the full internal tide velocities. The reconstructed n-th EOF mode, as given by Eq.(A.13), describes a 3-dimensional wave that propagates horizontally with a fixed vertical structure but horizontally varying wavenumber vector (k_n, l_n). Thus, the EOF method not only decomposes an IT into modes. It also provides concise information about these modes propagate in space. With this method, we are equipped for quantifying how a mode, especially mode 1, changes when interacting with an Agulhas ring.

A.3.3 *M2 energy flux*

The M2 energy flux is calculated using M2 internal tide velocity u' and pressure p'. The former is given in Eq.(A.2). The latter is obtained following Li and Storch, 2020 and expressed in terms of amplitude A_p and phase ϕ_p in a way similar to u' in Eq.(A.2). The time-mean energy flux is then given by the expression

$$< \mathbf{u}'p' >= \frac{1}{2}A(x,y,z)A_p(x,y,z)(\cos(\phi(x,y,z) - \phi_p(x,y,z))). \tag{A.19}$$

The resulting M2 baroclinic energy flux is shown in Fig.A.1 in form of purple arrows. They show the expected propagation of the IT beams away from the Walvis ridge (grey contours), where they are generated.

A.3.4 *Kinetic Energy*

We quantify the strength of M2 internal tides in terms of the time-mean kinetic energy

$$E_{kin}(x,y,z) = \frac{A_u^2(x,y,z) + A_v^2(x,y,z)}{2}, \tag{A.20}$$

where A_u and A_v are, respectively, the amplitudes of the zonal and meridional IT velocity. They can be either the amplitudes of the full IT velocity given in Eq.(A.2), or the amplitudes of the IT velocity associated with the n-th mode. In the latter case, $E_{kin,n}$ indicates the strength of the n-th mode.

To reduce noises, we consider box-averaged E_{kin}, rather than grid-point values of E_{kin}. We focus on boxes that are located near the *onset* of our beam, which are

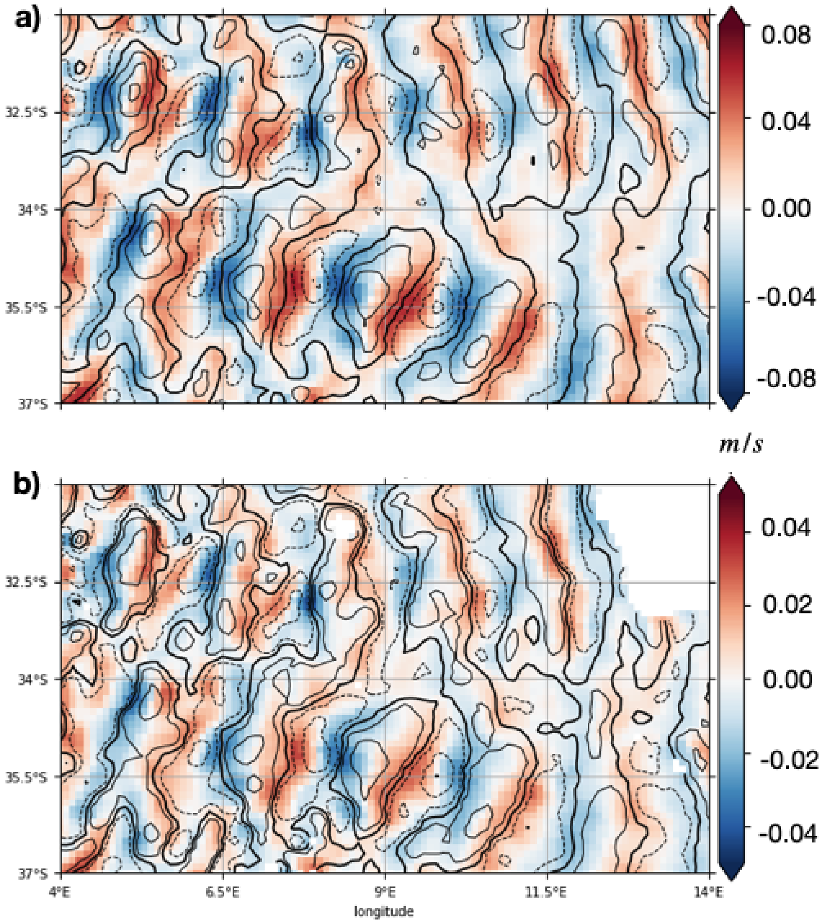

Figure A.6: A snapshot of M2 internal-tide zonal velocity in m/s at time $t = t_0$ (contour lines) and a quarter of a period later (color shadings) a) as given in Eq.(A.2) and b) as reconstructed using EOF1 according to Eq.(A.14).

indicated by the magenta boxes in Fig.A.13 and Fig.A.14. E_{kin} averaged over such a box is referred to as E_{os}, and is used to quantify the strength of internal tide near the generation site of our beam. We consider also boxes that are located *downstream* of our beam, in particular downstream of an Agulhas ring in case when our beam is crossed by an Agulhas ring. These boxes are indicated by the green boxes in Fig.A.13 and Fig.A.14. E_{kin} averaged over such a box is referred to as E_{ds}. The ratio E_{ds}/E_{os} on a beam indicates the dissipation of internal tide along the beam.

Whether or not an Agulhas ring can lead to dissipation of IT can be quantified by comparing E_{ds}/E_{os} in a month when our beam is essentially free of Agulhas rings with E_{ds}/E_{os} in a month when our beam is crossed by an Agulhas ring. Certainly this quantification method is very crude. An improvement of the method is needed, but will be retained for future studies.

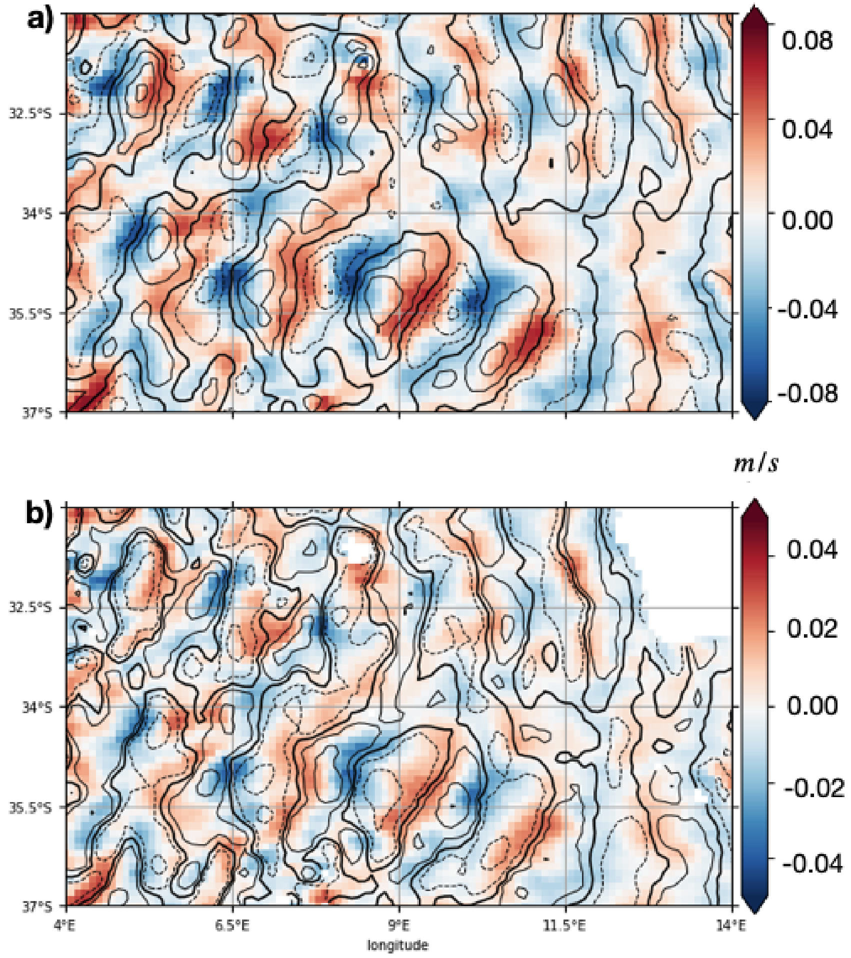

Figure A.7: A snapshot of the internal-tide zonal (color shadings) and meridional velocities (contour lines) at the same timestep, a) as given in form of Eq.(A.2) and b) as reconstructed using EOF1 according to Eq.(A.14).

A.4 RESULTS

A.4.1 *Modes of the M2 Internal Tide in the Walvis Region*

This subsection examines the general properties of the modes, focusing on their spatial structures, horizontal scales, and their seasonality. For this purpose, we apply the EOF decomposition method to a combined data set made of amplitudes and phases obtained by harmonic analyzing the data from February and March for the summer season and June and July for the winter season.

Following the EOF decomposition method, the n-th mode is a mode that propagates horizontally with its horizontal structure and scale determined by the n-th EOF $e_n(x,y)$ and its vertical structure determined by the corresponding PC $\alpha_n(z)$. Two EOFs, $e_1(x,y)$ and $e_5(x,y)$, are shown in Fig.A.8 and A.9 respectively. The corresponding PCs, i.e the vertical structures, α_1 and α_5, together with α_3 and α_9 are shown in Fig.A.10. For the n-th PC, we observe n zero-crossings in the vertical. This corresponds to a decrease in vertical scale with increasing number of

EOF Number	1	2	3	4	5
variance	74.4%	17.2%	5.1%	1.7%	0.7%
accumulated variance	74.4%	91.7%	96.7%	98.4%	99.1%

Table A.1: Variance (second row) explained by and the accumulated variance (third row) explained up to the n-th EOF, with $n = 1, \cdots, 5$, derived for the summer season.

mode. The low-order EOFs represent hence low modes with larger vertical scales; and the high-order EOFs represent high modes with smaller vertical scales. The vertical variances captured by the first 5 EOFs are listed in Tab.A.1. We find that the first EOF explains 74.4%, and the first 5 EOFs explain together 99.1% of the total variance. Thus, the M2 internal tide simulated by ICON-O is dominated by the lowest modes described by the leading EOFs.

The horizontal structures of the low modes differ strongly from those of the high modes. As can be seen from Fig.A.8 and A.9, both EOF1 and EOF5 reveal wave-like patterns that radiate away from the Walvis Ridge and are characterized by alternating positive and negative velocities. However, the wave structures associated with EOF1 have much larger scales than those associated with EOF5. Moreover, while the waves related to EOF1 can propagate over a distance of about 1000 km and reach the African continent, the waves related to EOF5 are most intense in the immediate proximity of the Walvis ridge. It appears that ICON-O can simulate high-mode internal tides, but the horizontal propagation of these high modes is more strongly dissipated than that of the low modes. Finally, further away from the Walvis ridge, the velocities associated with EOF5 tend to cluster into circular patches, a feature completely absent in EOF1. We will come back to the high-mode horizontal structures later.

To quantify the horizontal scales of the modes, we estimate the wavelength L_n according to Eq.(A.17) and Eq.(A.18). We consider averages of L_n over an area, rather than grid-point values of L_n. Due to the strong spatial inhomogeneity of high modes, seen e.g. for EOF5 in Fig. A.9, characterized by extremely small values outside circular patches relative to those inside the patches, large gradients of the phase ϕ_n can arise across the rims of patches. As these large gradients are difficult to interpret, we select the area to be comparable to one of those patches (see black box in Fig. A.15), rather than taking the entire study domain into account.

Two features are observed from the area-averaged wavelengths shown in the top panel of Fig.A.11. The first one is a decrease in horizontal wavelength with increasing number of EOF, from approximately 137 km in summer and 157 km in winter for the first mode to approximately 56 km in summer and 63 km in winter for the ninth mode (Fig.A.11). This decrease is most prominent for the low modes, but weakens for higher modes. For $n > 5$, the decrease is nearly absent, and the wavelength becomes essentially independent of the mode number. We speculate that this may be a consequence that ICON-O in 5km resolution cannot fully resolve high modes. The situation may be improved when further increasing the horizontal resolution.

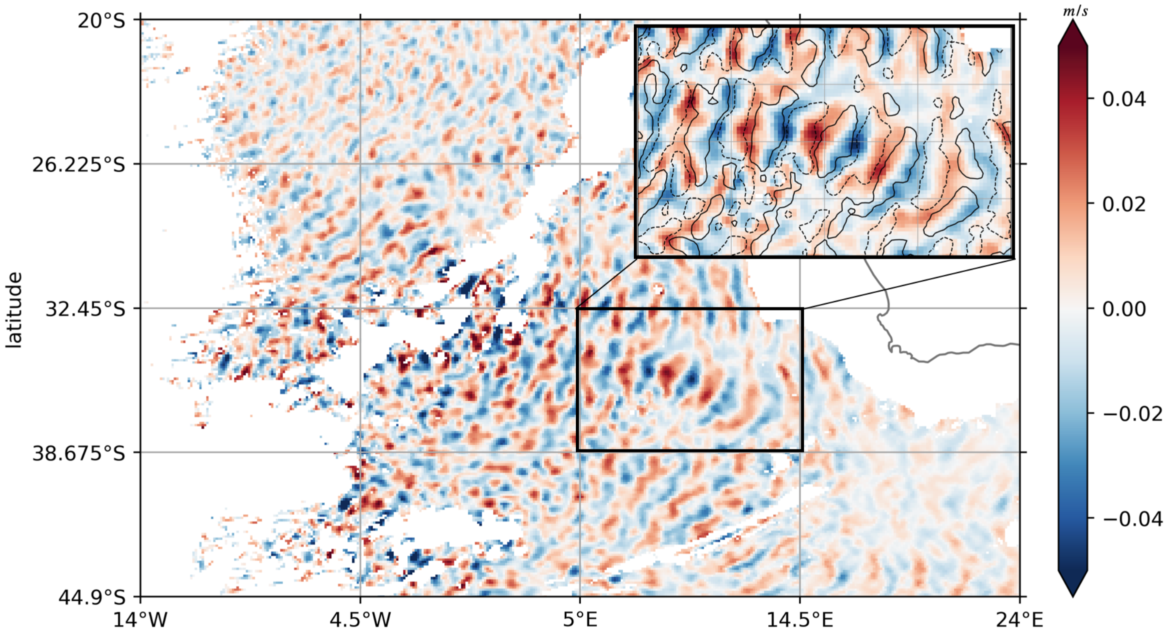

Figure A.8: The e^c part of the EOF-decomposed mode 1, as derived for the summer season. The insert is an enlarged picture showing e^c in colors and e^s in contours (positive solid, negative dashed).

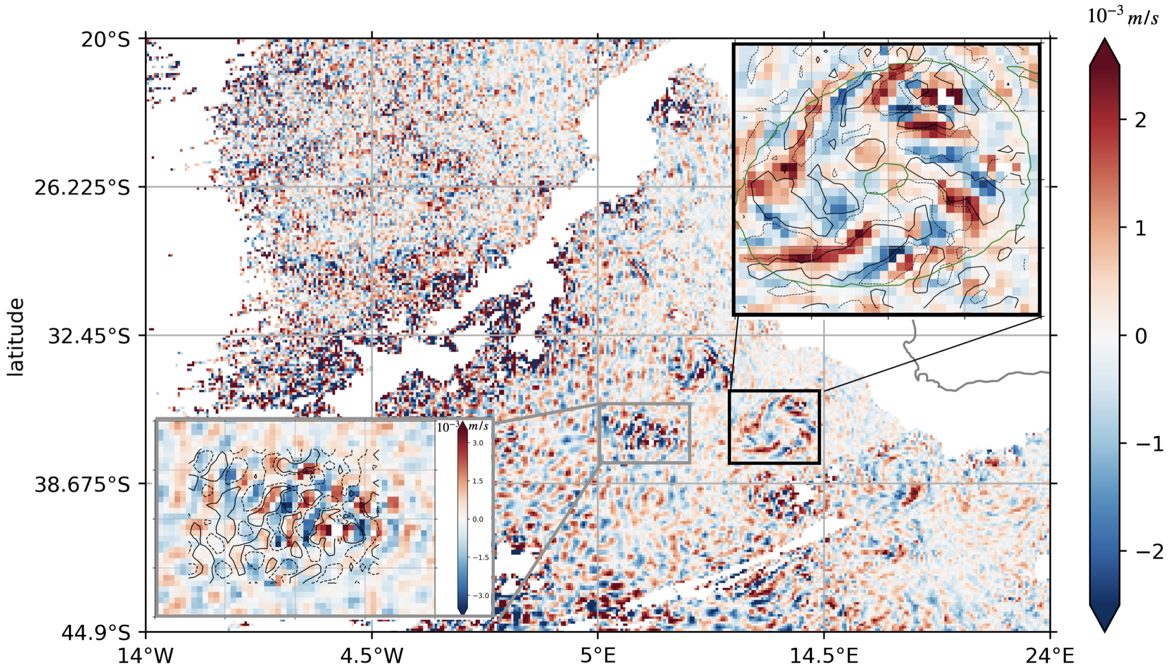

Figure A.9: Same as Fig.A.8, but for EOF5 and with two enlarged inserts. The thin green contour in the upper right insert indicates an Agulhas ring. The small white spot in the lower left insert indicates a sea mount.

The second feature is the notable dependence of the mean wavelength on season: the mean wavelength L_n during summer is shorter than that during winter, especially for mode 1 and 2. The difference in wavelength is likely caused by the strong seasonality in stratification. According to Fig.A.4, the buoyancy frequency

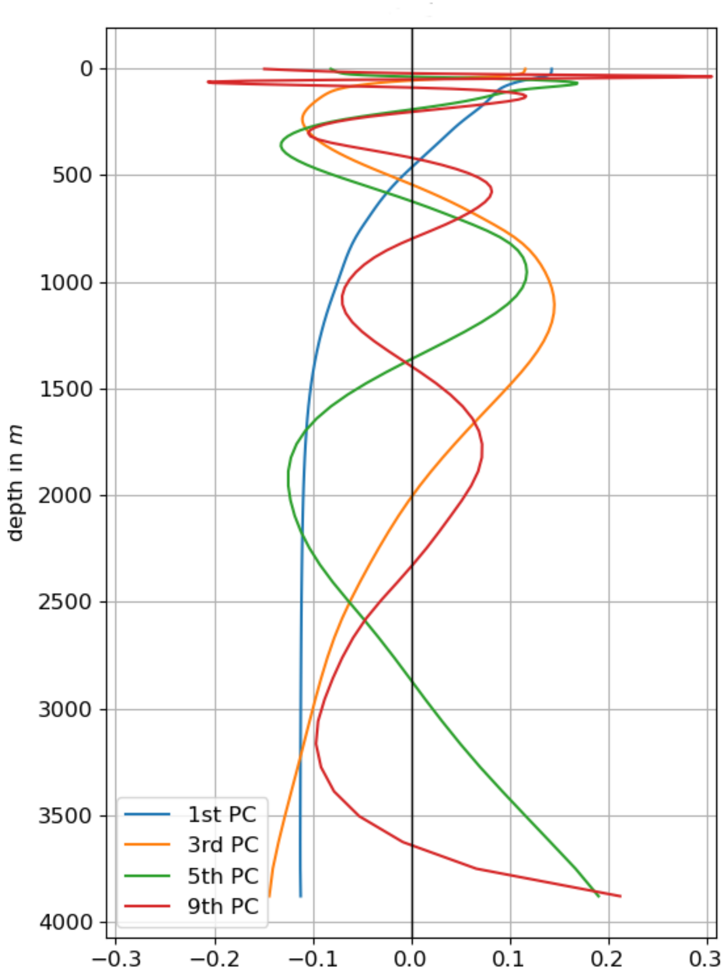

Figure A.10: Principal components α_n, for $n = 1, 3, 5, 9$, obtained by projecting the detrended internal-tide zonal velocity (more precisely C and S in Eq.(A.3)) above 4000 m onto the respective EOFs.

N increases from about 10^{-3} in winter to about 10^{-2} in summer, by almost one order of magnitude in some areas. Fig.(A.11) suggests that stronger stratification leads to waves with shorter wavelength. Accompanied by an increase in horizontal wavelength is an increase in vertical scale in winter relative to that in summer. Comparing the vertical structures of the low modes (1 to 3), we observe a deepening of the low-mode nodes during winter (dashed lines in Fig. A.12), likely also caused by the seasonal stratification differences. This change in vertical scale is in line with observations using mooring data in the South China Sea (Yang, Li, and Feng, 2023).

The seasonality in stratification impacts not only the wavelength, but also the wave intensity. In terms of wave energy E_{kin} near the onset of the beam, Table A.2 shows that the IT is stronger in summer than in winter. We conclude that stronger stratification leads to stronger and shorter internal tides, raises the zero-crossing positions in the vertical structures. A similar seasonal impact on wavelength is also found by Liu et al. (2019) who compared the IT wavelengths in the Yellow Sea between November and May combining numerical modeling and observations.

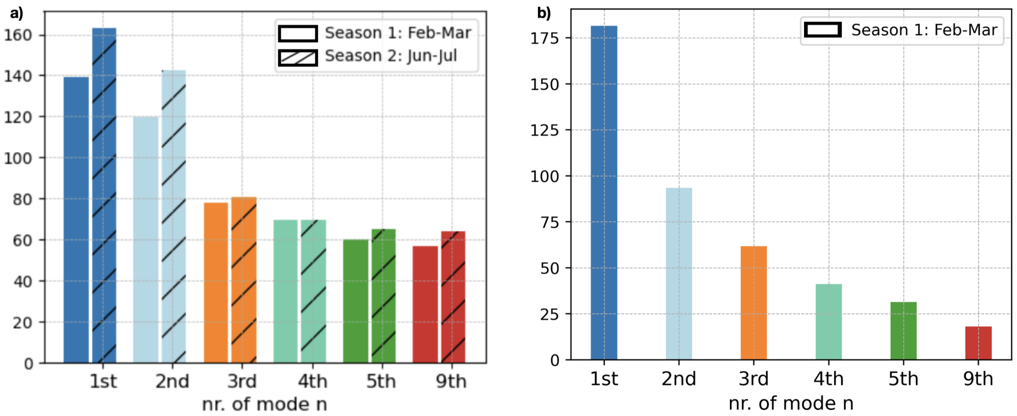

Figure A.11: Area-averaged wavelength λ_n as defined in Eq.(A.18), for the two cases: a) EOF decomposed modes, derived for summer (non hatched) and winter (hatched) in km. and b) SL decomposed modes. The area used for the averaging is indicated in Fig. A.15.

	FEB (no eddy)	MAR (eddy)	JUN (no eddy)	JUL (eddy)
total	18	16	14	10
mode 1	0.98	0.92	0.77	0.5

Table A.2: Mean kinetic energy averaged over a box near the onset of our internal tide beam, E_{os}, derived from the full and mode-1 internal tide velocity in each of the four considered months. The unit is cm^2/s^2. Each box contains 30 grid points. The location of the boxes is displayed in Fig.A.13 and A.14.

A.4.2 *Impact of Agulhas Rings on the Mode 1*

In order to quantify the impact of Agulhas Rings on the exact vertical structure of the mode-1 IT, the EOF decomposition is carried out in three different ways. First, we perform the EOF decomposition on the combined data set consisting of both the month with and the month without an Agulhas ring on the wave beam, as it is done in subsection 4a. The resulting mode 1 has, by construction, the same vertical structure in both months. By projecting the February and March (or June and July) data onto α_1, we can explore how the horizontal structure related to the same mode 1 vertical structure changes when the beam is crossed by an Agulhas ring. Secondly, we perform the EOF decomposition on each month separately so that both the horizontal and the vertical structure of the mode 1 are allowed to change due to interaction with an Agulhas Ring. In both cases, the EOF analysis is carried out over a large domain, namely that shown e.g. in Fig.A.1 or in Fig.A.8. With such a domain, which was chosen to allow tracing the origin of the high modes (see subsection 4c), the resulting PC1 should be considered as representative for the vertical structure averaged over the entire domain. To rule out the possibility that such an average may obscure small changes associated with a particular wave

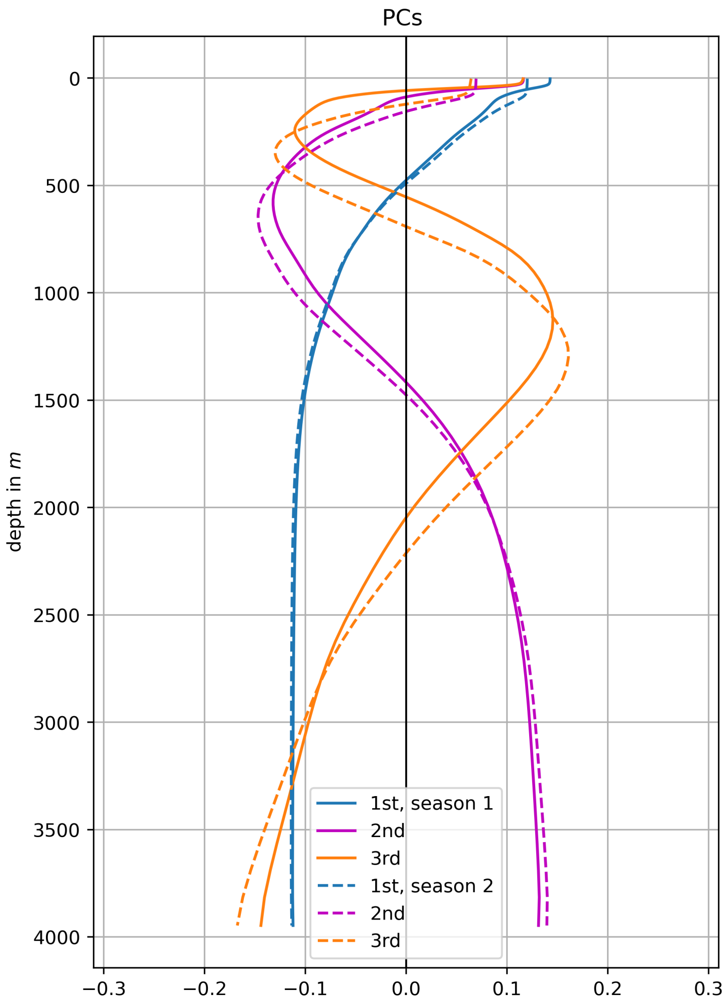

Figure A.12: Principal components PC1 (blue), PC2 (magenta), and PC3 (orange) in summer (February/March, solid lines) and in winter (June/July, dashed lines).

beam, we consider also a smaller area that contains essentially only data on and near the beam in question. As a third way, the EOF decomposition is perform on data in this small area for each month separately.

The result of the three EOF decompositions show a PC1 that has essentially the same vertical structure. Thus, we conclude that the vertical structure of mode 1 is unchanged by an crossing Agulhas ring. Below we concentrate on the horizontal structure. We examine how this structure changes from a month when a mode-1 beam is free of Agulhas ring to a month when the mode-1 beam is crossed an Agulhas ring. We have in total two cases, namely the case February versus March and the case June versus July.

The major impact of an Agulhas Ring on mode 1 horizontal structure is a change of the propagation direction of the mode, characterized by a southward shift of the associated wave beam. In February the wave train that is described by the blue wavenumber vectors in Fig.A.13a), is essentially free of Agulhas rings (black contours). This wave train runs almost zonally north of 33°S. When crossed by an Agulhas Ring in March, the beam, now described by the red wavenumber vectors in Fig.A.13b), is displaced further southward and located mostly south of 33°S. A similar redirection of internal-tide beam is also observed during June and July shown in Fig.A.14. In June, the beam that is described by the blue wavenumber vectors in Fig.A.14a, is essentially free of Agulhas rings. When crossed by an Agulhas ring in July, the beam, now described by the red wavenumber vectors in Fig.A.14b, is displaced further southward. We hence conclude that the main impact of an Agulhas ring is a southward redirection of the beam of mode 1 internal tide. Evidence of IT refraction caused by an anticyclonic eddy was also found in observations (Huang et al., 2018).

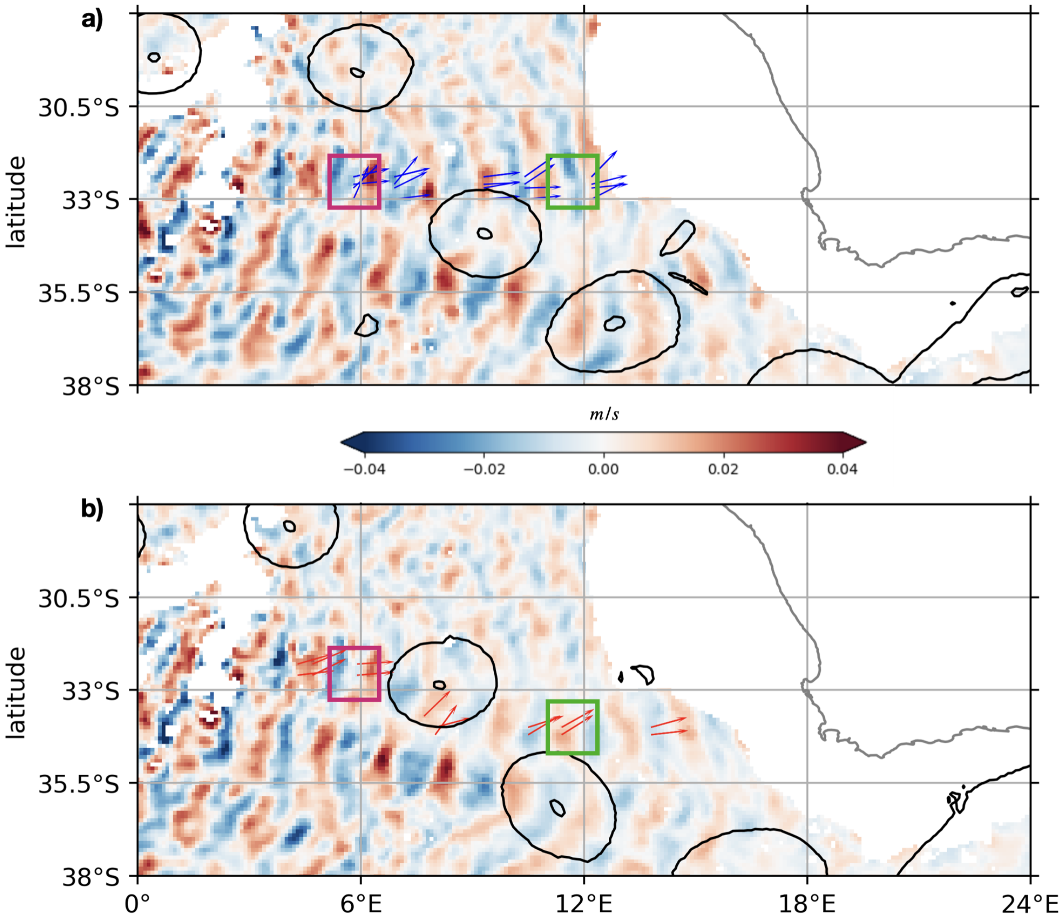

Figure A.13: A snapshot of the mode-1 zonal velocity in a) February and b) Match, reconstructed according to Eq.(A.13) for $t = 1$. The arrows are the wavenumber vectors (k_n, l_n) calculated at grid points with local velocity extrema at the considered time. Eddies are outlined by black contours representing contours of total horizontal current speed at 0.4 m/s

Löb et al., 2020 reported enhanced weakening of the energy fluxes of mode 1 and mode 2 in the Azores coinciding with the passing of two eddies during their observational campaign. Since the weakening is observed at a fixed location using mooring data, the observations by Löb et al. (2020) can indicate three possible ways, through which an eddy can impact internal tides. First, if the eddy redirects the wave beam, the weakening could be a result of a spatial shift of the beam. As the beam moves away from the mooring, the energy flux measured at the mooring decreases. Second, if the eddy does not redirect the beam, the weakening could

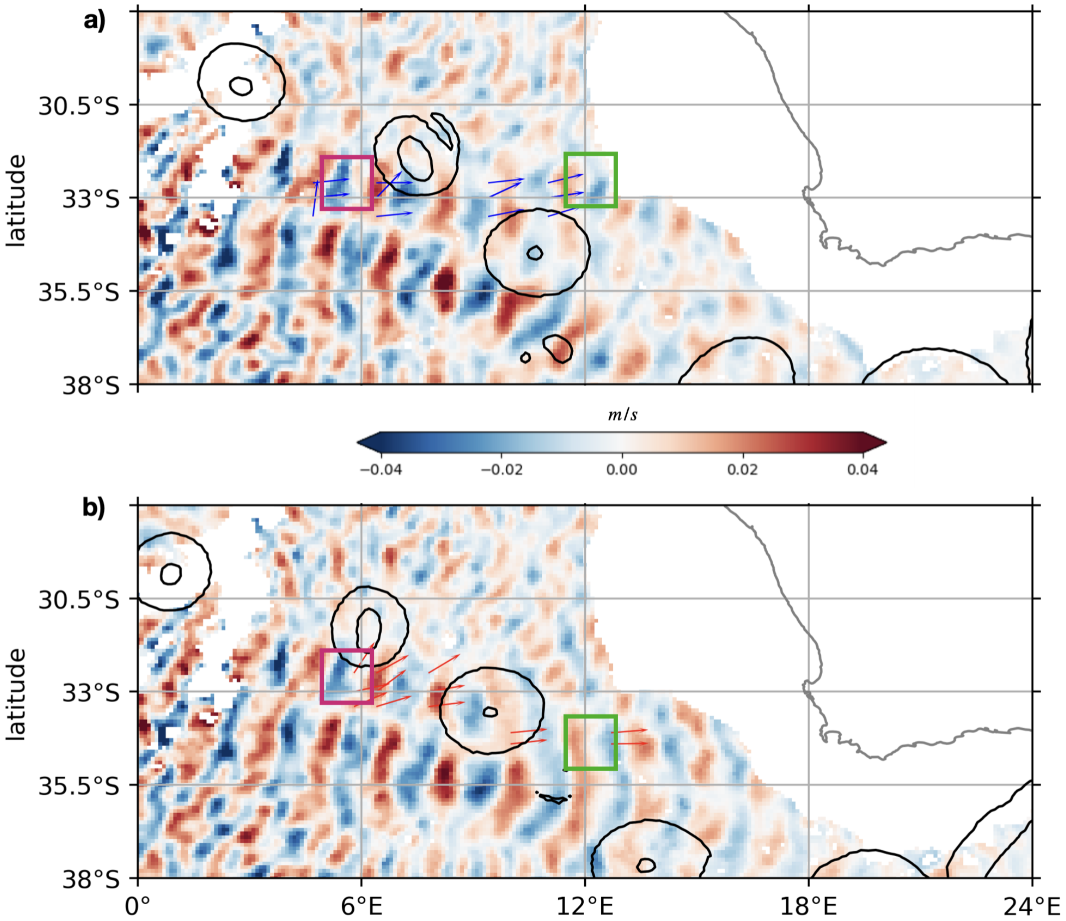

Figure A.14: Same as in Fig.A.13 but for the case June and July.

be a result of energy exchange between the eddy and the beam. In this case, the observations by Löb et al. (2020) indicates that the interaction with aneddy damps the energy of the low mode. Finally, the eddy can both redirect and damp the low modes of internal tides. Our result that an Agulhas ring redirects the beam is not inconsistent with the observational studies.

To quantify whether and how the wave energy is modified due to the refraction by an Agulhas ring, we calculate the wave energy along a wave train. For that we calculate E_{ds}/E_{os}, which characterizes the wave energy downstream of a beam, E_{ds}, relative to the wave energy near the onset of the beam, E_{os}, for both the month without and the month with an Agulhas ring crossing the beam in question. The result is listed in Table A.3. Generally, the internal tide loses its kinetic energy as it is propagated along the beam, both for E_{ds}/E_{os} derived from the full internal tide velocity and for E_{ds}/E_{os} derived from the mode-1 velocity, independent whether the wave train is crossed by an Aguhlas Ring or not. The loss ranges from about 20% to 40%. We observe that the impact of an Agulhas ring on E_{ds}/E_{os} is different in the two cases we have. When crossed by an Agulhas ring in March, the energy loss is stronger, indicated by a smaller value of E_{ds}/E_{os} in March than in February, when the beam is essentially free of Agulhas rings. This is true for E_{ds}/E_{os} obtained both from the full and from the mode-1 velocity, indicating that there is a damping of low mode wave energy due to Agulhas Ring. However, the situation is different for June and July. The ratio E_{os}/E_{ds} is higher in July when the beam is crossed by an Agulhas ring than in June when the beam is free of any Agulhas rings.

	FEB (no eddy)	MAR (eddy)	JUN (no eddy)	JUL (eddy)
total	33%	25%	21%	40%
mode 1	33%	21%	18%	44%

Table A.3: Ratio E_{ds}/E_{os} of internal tide kinetic energy averaged over a box near the onset of the beam to that over a box downstream of the beam, obtained for four months from the full and the first EOF mode. Each box contains 30 grid points. The location of the boxes are indicated in Fig.A.13 and A.14.

Tab.A.3 suggests that we cannot clearly conclude that a wave train is more strongly damped when it is refracted by an Agulhas Ring relative to when it is essentially unaffected by Agulhas Ring. It is possible that the different behavior of E_{ds}/E_{os} in February/March and June/July is partly related to the different strengths of IT in different seasons. Our efforts to address this problem by analyzing kinetic energy maps (as opposed to kinetic energy averaged over boxes), and by tracking the kinetic energy along the entire beam (rather than just considering two boxes), have not produced a significantly clearer picture (not shown). Likewise, calculating the frequency spectra of the internal velocities along the beams and comparing the spectral energy at the M2 frequency before and after the interaction has provided only limited insight. Likely, longer simulations with more cases and a more detailed analysis on the full energy budget are required to clarify whether and to what extent Agulhas Rings damp the mode 1 IT, as they travel across the mode 1 beams.

A.4.3 *Impact of Agulhas Rings on High Modes*

The high modes—mode 5 to 10—account together for $\approx 1.4\%$ of the total vertical variance in the data. Despite this small amount of explained variance, they can nevertheless be important, as they might result from the scattering of a low mode by Agulhas Rings. The high modes reveal two features, which are depicted by Fig.A.9 and Fig.A.15 in terms of mode 5. The first one, that the high modes are strong in the immediate proximity of the Walvis Ridge, is already mentioned earlier. We interpret them as the modes generated by surface tides at the Walvis Ridge that dissipate shortly after their generation.

The second feature is that the high modes with large velocities cluster into circular patches. Recall that e_5^s occurs a quarter of wave period later than e_5^c. An enlarged picture of e_5^c and e_5^s associated with one patch (the upper right insert in Fig.A.9) suggests that the horizontal structures inside this patch resembles anti-clockwise propagating waves. The patches are located further away from the Walvis Ridge, and are likely not generated by surface tides at the Walvis Ridge. When overlayed with the mean flow velocity (see black lines in Fig.A.15), most of the circular patches collocate very well with the Agulhas rings. They move with the Agulhas rings, which, after circulating around the southern coast of South Africa, move northwestward and enter the South Atlantic. Thus, we interpret these patches as high modes trapped inside the Agulhas rings.

How exactly the high modes are generated and trapped by the Agulhas Rings is unclear. They can also be generated in a way as found in idealized simulations (Wang and Legg, 2023). They can even be a result of instabilities or even slaved modes (Chouksey, Eden, and Olbers, 2022). Whatever mechanism is responsible for their generation, Fig.A.15 suggests that the high modes have already become trapped before the Agulhas Rings have reached the IT beams generated by the Walvis ridge. Thus, the high modes trapped inside Agulhas Rings cannot be considered as resulting from scattering of the low modes that propagate along these beams.

Not all patches of high modes are clearly associated with Agulhas rings. This is the case for the patch in the vicinity of a small seamount near 36.5°S between 6°E and 9°E Fig.A.15. The lower left insert in Fig.A.9 shows the two parts of EOF5, e^c in colors and e^s in contours, essentially overlapping with each other, indicating a horizontally standing wave. These standing waves may represent lee waves resulting from the interaction of the IT with the nearby topography (small white spot inside the lower left insert).

A.4.4 *IT modes derived from Sturm-Liouville equation*

In this subsection, we compare our EOF modes with modes derived from the eigenvectors a_n of the Sturm-Liouville equation (A.4). For each month, we use the time-averaged stratification profiles at each grid point to compute the modes, which are then normalized. The modal velocities are reconstructed by projecting internal tide zonal (meridional) velocity u' (v') on to eigenvectors a_n following Eq.(A.7). We focus on the first 10 for the analysis.

Fig.A.16 shows the resulting mode 1 of the M2 internal tide during a) February when the considered tidal beam is essentially free of Agulhas rings and b) March when an Agulhas ring crosses the beam. The horizontal structures of the zonal velocities as well as their magnitudes compare remarkably well with the ones derived by EOF1, e_1, shown in Fig.A.13. In particular, we see the same displacement of the IT beam from north of 33°S in February to south of 33°S in March. The main features of the high EOF modes are also revealed by the high Sturm-Liouville modes. In particular, as shown in Fig.A.17, we observe again the trapping of the higher modes inside the eddies.

The bottom panel of Fig.A.11 shows the mean horizontal wavelengths obtained using the dispersion relation given in Eq.(A.9). For mode 1, the SL wavelength of 182 km is about 40 km (~ 25%) longer than that of the EOF mode 1. For all higher modes, the SL wavelengths are up to 40 km shorter than the respective EOF wavelengths, with the shortening reaching about 35% for mode 9. Moreover, the SL wavelength clearly decreases with increasing mode number. We interpret this as a weakness of the SL method. Even though the decrease is consistent with the linear theory, quite a few assumptions must be made so that the eigenvalues, and with that the wavelengths, depend only on the local stratification and water depth. As

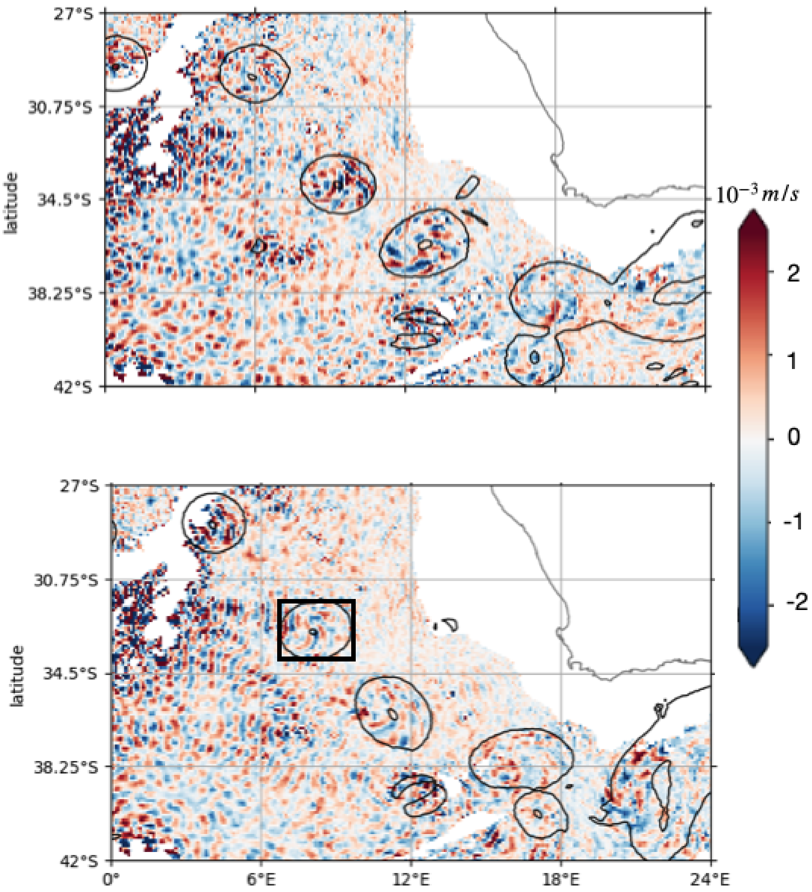

Figure A.15: Same as Fig.A.13, but for the EOF mode 5. The black box indicates the area used to estimate the mean horizontal wavelengths for all modes.

a result, the linear wave theory has difficulties in quantifying the horizontal length scale. In contrast, the EOF decomposition captures the wavelength produced by the non-linear ICON model. We hence interpret the difference in the horizontal wavelength as reflecting the non-linear effects, which is ignored when applying the SL decomposition. Further investigation is needed to identify these non-linear effects.

The vertical structures of the SL modes are shown in Fig.A.18, both in terms of an area-average of eigenvectors (solid lines) and in terms of eigenvectors at three different grid points (dotted lines). We see that for mode 1, the vertical structure does not change much from grid point to grid point. Both the area-averaged (blue solid) and grid-point (blue dotted) eigenvector compare well with PC1 (blue dashed). Thus, mode 1 can be equally well identified by the SL and EOF decomposition as a horizontally propagating wave with a fixed vertical structure. The situation is different for higher modes, as illustrated by the green lines for mode 5. The eigenvector changes from grid point to grid point (green dotted lines), and deviates clearly from the area-averaged eigenvector (green solid) as well as from PC5 (green dashed). This variability implies a variability in the corresponding eigenvalue, and via dispersion relation, a variability in the horizontal wavelength. It appears that for a higher-order SL mode, both the horizontal wavelength and the

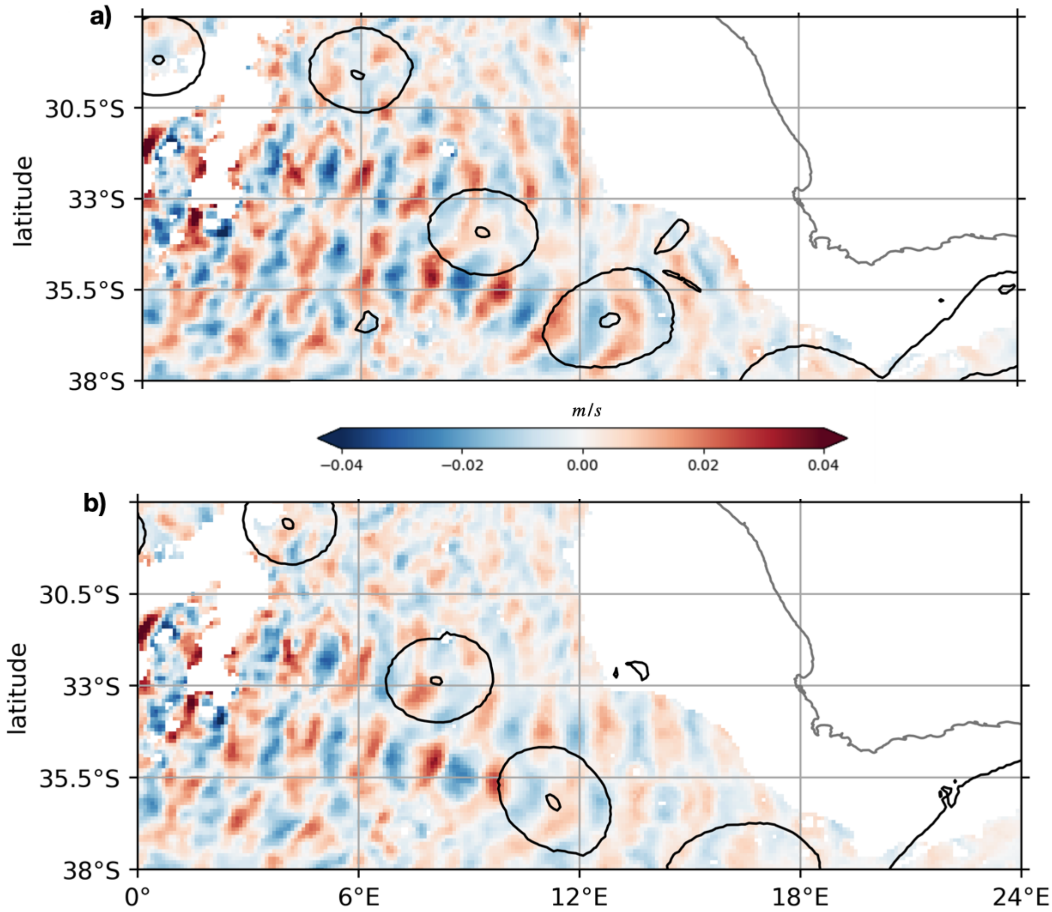

Figure A.16: A snapshot of the reconstructed SL mode 1 zonal velocity in m/s following Eq.(A.7) with $t = 1$ for February (a) and March (b) 2022. Black contours indicate the eddies.

vertical scale vary from grid point to grid point. Given that the SL modes cannot reflect the constraint on horizontal wavelength set by the model resolution, it is not clear which one of the two decomposition methods produces more realistic vertical structures. Further investigation is required to clarify this issue.

A.5 SUMMARY AND CONCLUDING REMARKS

In this work, we studied the eddy-induced changes in the M2 IT using the global general circulation ocean model ICON-O at 5km horizontal resolution with 128 vertical layers. To our knowledge, this is the first study addressing this topic based on a high-resolution GCM in a realistic setting. We focused on the Walvis Ridge region where both eddies and M2 IT are prominent. To investigate the impact of eddies on different modes of the IT we employed two decomposition methods: both the standard decomposition based on solving the SL equation and a new data-driven EOF decomposition. The former is performed at each grid point. The 3-dimensional structure of a SL mode is obtained by combining the solutions at all grid points, albeit the SL equation does not provide any information about how the results at different grid points are linked to each other. In contrast, the latter

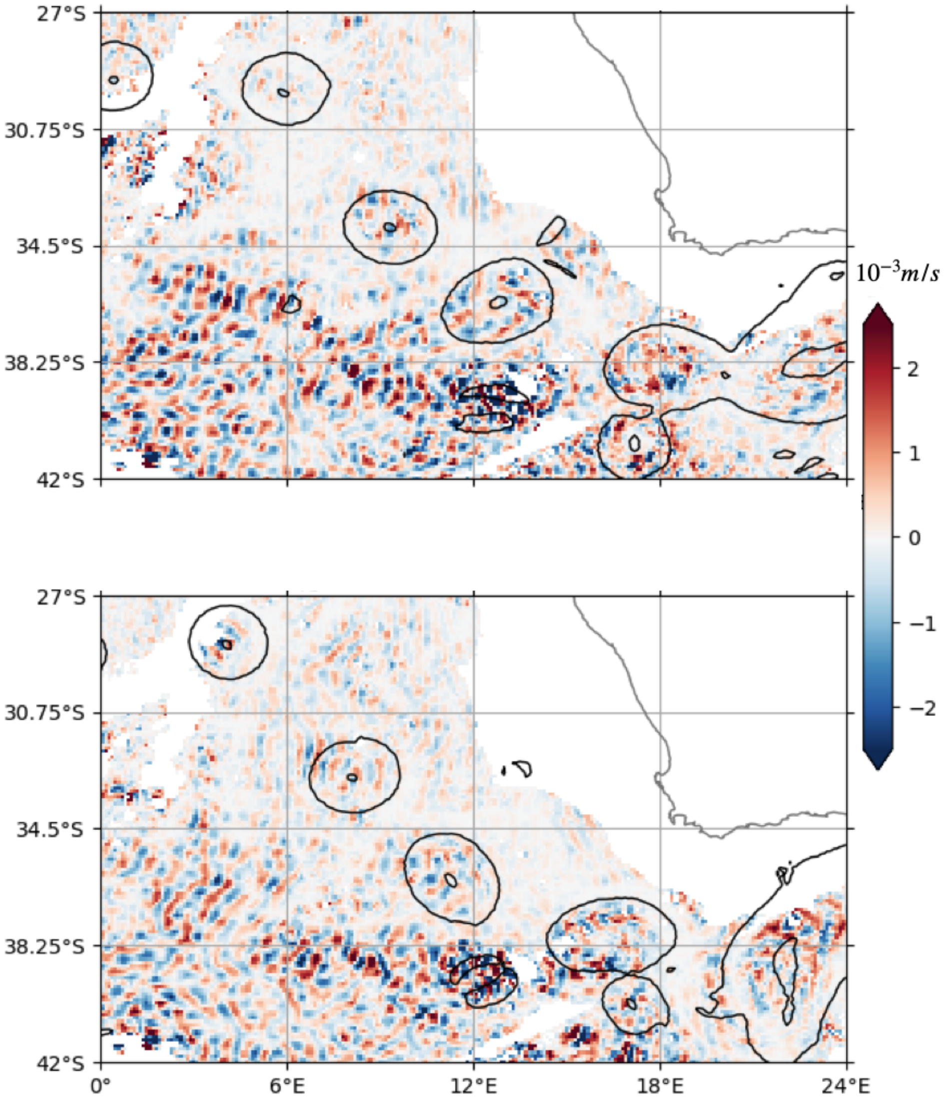

Figure A.17: Same as Fig.A.16 but the SL mode 5.

extracts the spatial structure of the IT directly from model simulations without relying on assumptions underlying linear wave theory. Each EOF mode represents horizontally propagating (or standing) waves that has a fixed vertical structure and variable horizontal wavelength. When both methods identify the same wave feature, it suggests that linear theory is sufficient to describe the dynamics, indicating a minor role of non-linear processes. However, when the results differ, it may signal the presence of non-linear interactions, though further investigation would be needed to confirm this.

Our analysis of the EOF modes revealed that the ITs in the Walvis Ridge region are dominated by mode 1, which explains over 70% of the total vertical variance and travels all the way from the ridge to the coast of African continent. Higher modes tend to have large magnitudes in the direct vicinity of the Ridge, or in form of patches. These patches often represent waves trapped inside Agulhas rings, but occasionally also lee waves arising near small sea mounts without involving strong eddies. The mean horizontal wavelength decreases with increasing mode number

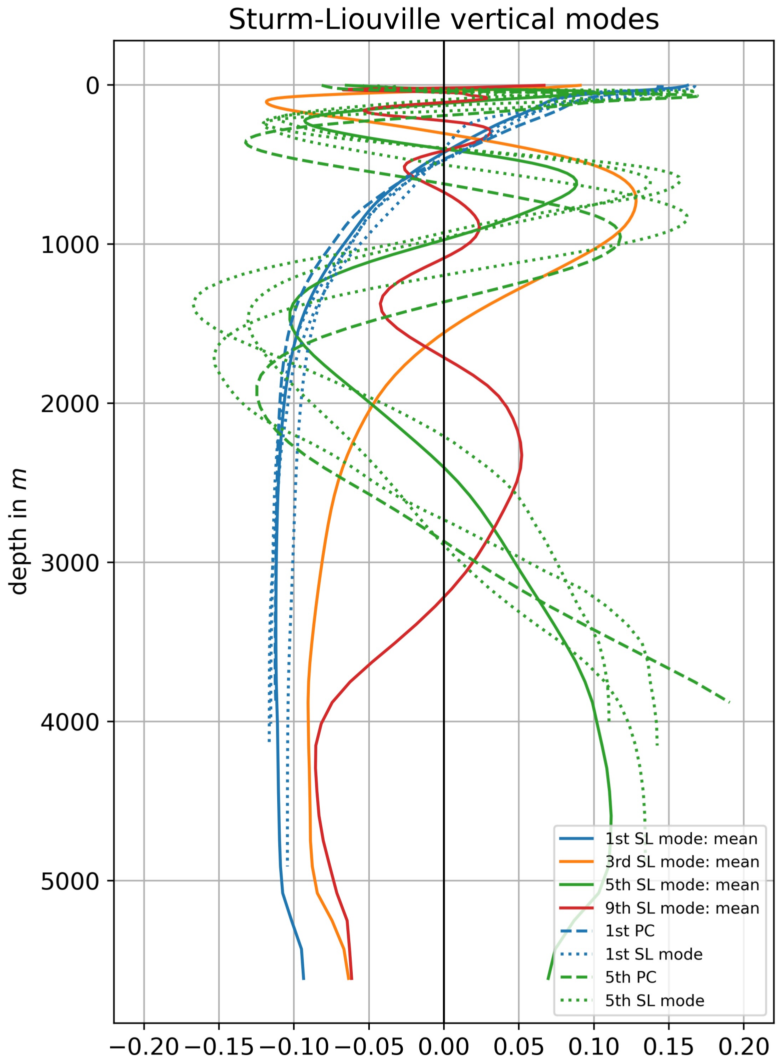

Figure A.18: Eigenvectors of the Sturm-Liouville equation. Solid lines are eigenvectors horizontally averaged over the study area, dotted lines indicate the first and the fifth eigenvector at three locations, and dashed lines indicate the first and fifth PC from the EOF decomposition method.

from around 150 km for mode 1 to about 60 km for mode 9, even though the decrease is hardly noticeable for mode number larger than three, possibly due to the fact that the model resolution is not sufficient to fully resolve the high modes. Seasonal differences in stratification also influence modal properties: stronger stratification in summer than in winter amplifies the modes, shortens the horizontal wavelengths, and raises the zero-crossing points in the vertical modal structures.

Regarding the role of Agulhas rings, we find that the main effect of Agulhas rings on internal tides is a refraction of mode 1 that makes its beam to shift southwards. The same southward shift is found in both months when a mode-1 beam is crossed by an Agulhas ring. The refraction concerns only the propagation path, without noticeably altering the vertical structure of mode 1. The high modes are trapped and carried by Agulhas rings as they enter the Atlantic from Agulhas retroflection region. As such, these modes cannot be considered as resulting from scattering of mode 1 generated at the Walvis Ridge by eddies. Comparing the EOF modes with the SL modes reveals both similarities and differences. Regarding the role of Agulhas rings, their effect is identified by both decomposition methods as a refraction of mode 1, characterized by a southward shift of the beam without noticeable change in vertical structure. This result suggests that the interaction between eddy and IT, at least that occurring in the Walvis region, does not involve strong nonlinear processes capable of producing waves that are strongly different from those described by linear wave theory. However, notable differences exist in wave properties: SL mode 1 wavelengths are longer and those of higher SL modes shorter than the corresponding EOF modes. The difference can be as large as 25 to 35%. Furthermore, SL high modes have vertical structures that vary strongly from grid point to grid point, whereas all EOF modes have a fixed vertical structure by construction. It is beyond the scope of this paper to clarify which representation of vertical structure of a high mode is more realistic.

We also briefly looked at the IT energetics before and after interacting with an Agulhas ring. Our findings on the eddy-induced change of the kinetic energy E_{kin} suggest weakening of the full and mode 1 E_{kin} during summer (Feb-Mar). However during winter (Jun-Jul) we observe a counter-intuitive strengthening of the IT kinetic energy. A possible explanation could be the seasonal variability of the IT properties. While our findings offer new insight into wave-eddy interactions, the detailed energetics remain unresolved. A full energy budget for this region should be conducted. This will allow for a deeper understanding of the energy transfer between modes and/or between the internal tide and eddies. This is planed for future work.

This study marks an important step toward quantifying the wave-eddy interactions in realistic global general circulation model simulations. Our results are likely more representative of real-world ocean dynamics due to both the more realistic encounter of waves with eddies and spatially varying environment simulated by the model. Additionally, the EOF method is computationally less demanding than the SL method. As computational power and model resolution continue to advance, this data-driven approach may prove more effective for diagnosing and quantifying complex nonlinear processes than theoretical methods, which often rely on strong simplifying assumptions.

BIBLIOGRAPHY

Adcroft, Alistair and Jean-Michel Campin (2004). "Rescaled height coordinates for accurate representation of free-surface flows in ocean circulation models." In: *Ocean Modelling* 7.3, pp. 269–284. ISSN: 1463-5003. DOI: `https://doi.org/10.1016/j.ocemod.2003.09.003`. URL: `https://www.sciencedirect.com/science/article/pii/S1463500303000544`.

Becker, J. J. et al. (2009). "Global Bathymetry and Elevation Data at 30 Arc Seconds Resolution: SRTM30_PLUS." In: *Marine Geodesy* 32.4, pp. 355–371. DOI: `10.1080/01490410903297766`.

Box, G.E.P. (1979). "Robustness in the Strategy of Scientific Model Building. Robustness in Statistics." In: DOI: `https://doi.org/10.1016/B978-0-12-438150-6.50018-2`.

Buijsman, Maarten C., Gordon R. Stephenson, Joseph K. Ansong, Brian K. Arbic, J.A. Mattias Green, James G. Richman, Jay F. Shriver, Clément Vic, Alan J. Wallcraft, and Zhongxiang Zhao (2020). "On the interplay between horizontal resolution and wave drag and their effect on tidal baroclinic mode waves in realistic global ocean simulations." In: *Ocean Modelling* 152, p. 101656. ISSN: 1463-5003. DOI: `https://doi.org/10.1016/j.ocemod.2020.101656`. URL: `https://www.sciencedirect.com/science/article/pii/S146350032030158X`.

Chen, Zifei, Fei Yu, Zhiwu Chen, Jianfeng Wang, Feng Nan, Qiang Ren, Yibo Hu, Anzhou Cao, and Tongtong Zheng (2023). "Downward Propagation and Trapping of Near-Inertial Waves by a Westward-Moving Anticyclonic Eddy in the Subtropical Northwestern Pacific Ocean." In: *Journal of Physical Oceanography* 53.9, pp. 2105 –2120. DOI: `10.1175/JPO-D-22-0226.1`. URL: `https://journals.ametsoc.org/view/journals/phoc/53/9/JPO-D-22-0226.1.xml`.

Chouksey, Manita, Carsten Eden, and Dirk Olbers (2022). "Gravity Wave Generation in Balanced Sheared Flow Revisited." In: *Journal of Physical Oceanography* 52.7, pp. 1351 –1362. DOI: `10.1175/JPO-D-21-0115.1`. URL: `https://journals.ametsoc.org/view/journals/phoc/52/7/JPO-D-21-0115.1.xml`.

Cummins, P.F., J.Y. Cherniawsky, and M.G.G Foreman (2001). "North Pacific internal tides from the Aleutian Ridge: Altimeter observations and modeling." In: *Journal of Marine Research* 59.2.

Cusack, Jesse M., J. Alexander Brearley, Alberto C. Naveira Garabato, David A. Smeed, Kurt L. Polzin, Nick Velzeboer, and Callum J. Shakespeare (2020). "Observed Eddy–Internal Wave Interactions in the Southern Ocean." In: *Journal of Physical Oceanography* 50.10, pp. 3043 –3062. DOI: `10.1175/JPO-D-20-0001.1`. URL: `https://journals.ametsoc.org/view/journals/phoc/50/10/jpoD200001.xml`.

D.Olbers, C.Eden, and J.Willebrand (2012). *Ocean Dynamics*.

Dong, Jihai, Baylor Fox-Kemper, Hong Zhang, and Changming Dong (2020). "The Seasonality of Submesoscale Energy Production, Content, and Cascade." In: *Geophysical Research Letters* 47.6. DOI: `https://doi.org/10.1029/2020GL087388`.

Dunphy, Michael, Aurelie L.Ponte, Patrice Klein, and Sylvie Le Gentil (2017). "Low-Mode Internal Tide Propagation in a Turbulent Eddy Field." In: *Journal of Physical Oceanography* 47.3.

Dunphy, Michael and Kevin G. Lamb (2014). "Focusing and vertical mode scattering of the first mode internal tide by mesoscale eddy interaction." In: *Journal of Geophysical Research: Oceans* 119.1, pp. 523–536. DOI: `https://doi.org/10.1002/2013JC009293`.

Eden, Carsten and Dirk Olbers (2017). "A closure for eddy-mean flow effects based on the Rossby wave energy equation." In: *Ocean Modelling* 114, pp. 59–71. ISSN: 1463-5003. DOI: `https://doi.org/10.1016/j.ocemod.2017.04.005`. URL: `https://www.sciencedirect.com/science/article/pii/S1463500317300537`.

Epke, Moritz and Nils Brueggemann (2025). "Overturning of Mixed Layer Eddies in a submesoscale resolving simulation of the North Atlantic." In: *Journal of Physical Oceanography* submitted.

Ferrari, Raffaele and Carl Wunsch (2009). "Ocean Circulation Kinetic Energy: Reservoirs, Sources, and Sinks." In: *Annu. Rev. Fluid Mech.* 41.253-82. DOI: `10.1146/annurev.fluid.40.111406.102139`.

Foreman, M. G. G., J. Y. Cherniawsky, and V. A. Ballatyne (2008). "Versatile Harmonic Tidal Analysis: Improvements and Applications." In: *Journal of Atmospheric and Oceanic Technology* 26, p. 806.

Garrett, Chris and Eric Kunze (2007). "Internal Tide Generation in the Deep Ocean." In: *Annual Review of Fluid Mechanics*.

Gaspar, Philippe, Grégoris Yves, and Jean-Michel Lefevre (1990). "A simple eddy kinetic energy model for simulations of the oceanic vertical mixing: Tests at station Papa and long-term upper ocean study site." In: *Journal of Geophysical Research* 95.C9, pp. 16179–16193. DOI: `https://doi.org/10.1029/JC095iC09p16179`.

Gerkema, T. and J.T.F. Zimmerman (2008). *An introduction to internal waves*.

Gill, A. E. (1982). *Atmosphere-Ocean Dynamics*.

Giorgetta, M. A. et al. (2018). "ICON-A, the Atmosphere Component of the ICON Earth SystemModel: I. Model Description." In: *Journal of Advances in Modeling Earth Systems* 10.7, pp. 1613–1637. DOI: `https://doi.org/10.1029/2017MS001242`.

Guo, Zheng, Shuya Wang, Anzhou Cao, Jieshuo Xie, Jinbao Song, and Xinyu Guo (2023). "Refraction of the M2 internal tides by mesoscale eddies in the South China Sea." In: *Deep Sea Research Part I: Oceanographic Research Papers* 192, p. 103946. ISSN: 0967-0637. DOI: `https://doi.org/10.1016/j.dsr.2022.103946`. URL: `https://www.sciencedirect.com/science/article/pii/S096706372200259X`.

Gutjahr, O., J. H. Jungclaus, N. Brüggemann, H. Haak, and J. Marotzke (2022). "Air-sea interactions and water mass transformation during a katabatic storm in the Irminger Sea." In: *Journal of Geophysical Research: Oceans*, submitted.

Hennon, Tyler D., Stephen C. Riser, and Matthew H. Alford (2014). "Observations of Internal Gravity Waves by Argo Floats." In: *Journal of Physical Oceanography* 44.9, pp. 2370 –2386. DOI: `10.1175/JPO-D-13-0222.1`. URL: `https://journals.ametsoc.org/view/journals/phoc/44/9/jpo-d-13-0222.1.xml`.

Hersbach, Hans et al. (2020). "The ERA5 global reanalysis." In: *Quarterly Journal of the Royal Meteorological Society* 146.730, pp. 1999–2049. DOI: `https://doi.org/10.1002/qj.3803`. eprint: `https://rmets.onlinelibrary.wiley.com/doi/pdf/10.1002/qj.3803`. URL: `https://rmets.onlinelibrary.wiley.com/doi/abs/10.1002/qj.3803`.

Hohenegger, Cathy, Peter Korn, Leonidas Linardakis, René Redler, Reiner Schnur, Panagiotis Adamidis, Jiawei Bao, Swantje Bastin, Milad Behravesh, Martin Bergemann, et al. (2023). "ICON-Sapphire: simulating the components of the Earth system and their interactions at kilometer and subkilometer scales." In: *Geoscientific Model Development* 16.2, pp. 779–811.

Huang, Xiaodong, Zhaoyun Wang, Zhiwei Zhang, Yunchao Yang, Chun Zhou, Qingxuan Yang, Wei Zhao, and Jiwei Tian (2018). "Role of Mesoscale Eddies in Modulating the Semidiurnal Internal Tide: Observation Results in the Northern South China Sea." In: *Journal of Physical Oceanography* 48.8, pp. 1749 –1770. DOI: `https://doi.org/10.1175/JPO-D-17-0209.1`. URL: `https://journals.ametsoc.org/view/journals/phoc/48/8/jpo-d-17-0209.1.xml`.

IPCC (2023). *Climate Change 2023: Synthesis Report. Contribution of Working Groups I, II and III to the Sixth Assessment Report of the Intergovernmental Panel on Climate Change*. IPCC. DOI: `10.59327/IPCC/AR6-9789291691647`.

Johnson, Gregory C., Shigeki Hosoda, Steven R. Jayne, Peter R. Oke, Stephen C. Riser, Dean Roemmich, Tohsio Suga, Virginie Thierry, Susan E. Wijffels, and Jianping Xu (2022). "Argo—Two Decades: Global Oceanography, Revolutionized." In: *Annual Review of Marine Science* 14.Volume 14, 2022, pp. 379–403. ISSN: 1941-0611. DOI: `https://doi.org/10.1146/annurev-marine-022521-102008`. URL: `https://www.annualreviews.org/content/journals/10.1146/annurev-marine-022521-102008`.

Johnston, T. M. Shaun and Mark A. Merrifield (2003). "Internal tide scattering at seamounts, ridges, and islands." In: *Journal of Geophysical Research: Oceans* 108.C6. DOI: `https://doi.org/10.1029/2002JC001528`.

Johnston, T. M. Shaun, Mark A. Merrifield, and Peter E. Holloway (2003). "Internal tide scattering at the Line Islands Ridge." In: *Journal of Geophysical Research: Oceans* 108.C11. DOI: `https://doi.org/10.1029/2003JC001844`. URL: `https://agupubs.onlinelibrary.wiley.com/doi/abs/10.1029/2003JC001844`.

Johnston, T. M. Shaun, Daniel L. Rudnick, and Samuel M. Kelly (2015). "Standing Internal Tides in the Tasman Sea Observed by Gliders." In: *Journal of Physical Oceanography* 45.11, pp. 2715 –2737. DOI: `10.1175/JPO-D-15-0038.1`. URL: `https://journals.ametsoc.org/view/journals/phoc/45/11/jpo-d-15-0038.1.xml`.

Klymak, Jody M., Robert Pinkel, and Luc Rainville (2008). "Direct Breaking of the Internal Tide near Topography: Kaena Ridge, Hawaii." In: *Journal of Physical Oceanography* 38.2, pp. 380 –399. DOI: `10.1175/2007JPO3728.1`. URL: `https://journals.ametsoc.org/view/journals/phoc/38/2/2007jpo3728.1.xml`.

Korn, P. et al. (2022). "ICON-O: The Ocean Component of the ICON Earth System Model—Global Simulation Characteristics and Local Telescoping Capability." In: *Journal of Advances in Modeling Earth Systems* 14.10. e2021MS002952 2021MS002952, e2021MS002952. DOI: `https://doi.org/10.1029/2021MS002952`. eprint: `https://agupubs.onlinelibrary.wiley.com/doi/pdf/10.1029/`

2021MS002952. URL: https://agupubs.onlinelibrary.wiley.com/doi/abs/10.1029/2021MS002952.

Korn, Peter (2017). "Formulation of an unstructured grid model for global ocean dynamics." In: *J. Comp. Phys.* 339, pp. 525–552.

— (2018). "A structure-preserving discretization of ocean parametrizations on unstructured grids." In: *Ocean Modelling* 132, pp. 73–90. ISSN: 1463-5003. DOI: https://doi.org/10.1016/j.ocemod.2018.10.002. URL: https://www.sciencedirect.com/science/article/pii/S1463500318301859.

Laxenaire, R., S. Speich, B. Blanke, A. Chaigneau, C. Pegliasco, and A. Stegner (2018). "Anticyclonic Eddies Connecting the Western Boundaries of Indian and Atlantic Oceans." In: *Journal of Geophysical Research: Oceans* 123.11, pp. 7651–7677. DOI: https://doi.org/10.1029/2018JC014270.

Li, Q., Wang B., Chen X., Chen X., and Park J. (2016). "Variability of nonlinear internal waves in the South China Sea affected by the Kuroshio and mesoscale eddies." In: *Journal of Geophysical Research Oceans* 121.4, pp. 2098–2118. DOI: https://doi.org/10.1002/2015JC011134.

Li, Zhuhua and Jin-Song von Storch (2020). "M2 Internal-Tide Generation in STORMTIDE2." In: *Journal of Geophysical Research: Oceans* 125.

Li, Zhuhua, Jin-Song von Storch, and Malte Mueller (2015). "The M2 Internal Tide Simulated by a 1/10°OGCM." In: *Journal of Physical Oceanography* 45.12. DOI: https://doi.org/10.1175/JPO-D-14-0228.1.

Liu, Kun, Junchuan Sun, Chuncheng Guo, Yang Yang, Weidong Yu, and Zexun Wei (2019). "Seasonal and Spatial Variations of the M2 Internal Tide in the Yellow Sea." In: *Journal of Geophysical Research: Oceans* 124.2, pp. 1115–1138. DOI: https://doi.org/10.1029/2018JC014819. eprint: https://agupubs.onlinelibrary.wiley.com/doi/pdf/10.1029/2018JC014819. URL: https://agupubs.onlinelibrary.wiley.com/doi/abs/10.1029/2018JC014819.

Löb, J., J. Köhler, C. Mertens, M. Walter, Z. Li, J. von Storch, Z. Zhao, and M. Rhein (2020). "Observations of the Low-Mode Internal Tide and Its Interaction With Mesoscale Flow South of the Azores." In: *JGR Oceans* 125.11.

MacKinnon, J. A., M. H. Alford, Oliver Sun, Rob Pinkel, Zhongxiang Zhao, and Jody Klymak (2013). "Parametric Subharmonic Instability of the Internal Tide at 29°N." In: *Journal of Physical Oceanography* 43.1, pp. 17 –28. DOI: 10.1175/JPO-D-11-0108.1. URL: https://journals.ametsoc.org/view/journals/phoc/43/1/jpo-d-11-0108.1.xml.

MacKinnon, Jennifer A. et al. (2017). "Climate Process Team on Internal Wave–Driven Ocean Mixing." In: *Bulletin of the American Meteorological Society* 98.11, pp. 2429 –2454. DOI: 10.1175/BAMS-D-16-0030.1.

Manders, A. M. M., L. R. M. Maas, and T. Gerkema (2004). "Observations of internal tides in the Mozambique Channel." In: *Journal of Geophysical Research: Oceans* 109.C12. DOI: https://doi.org/10.1029/2003JC002187.

Masson-Delmotte, V. et al. (2018). *Global Warming of 1.5°C. An IPCC Special Report on the Impacts of Global Warming of 1.5°C above Pre-industrial Levels and Related Global Greenhouse Gas Emission Pathways, in the Context of Strengthening the Global Response to the Threat of Climate Change, Sustainable Development, and Efforts to Eradicate Poverty*. IPCC. DOI: 10.59327/IPCC/SR15.

Munk, Walter and Carl Wunsch (1998). "Abyssal recipes II: energetics of tidal and wind mixing." In: *Deep Sea Research Part I: Oceanographic Research Papers* 45.12, pp. 1977–2010. ISSN: 0967-0637. DOI: `https://doi.org/10.1016/S0967-0637(98)00070-3`. URL: `https://www.sciencedirect.com/science/article/pii/S0967063798000703`.

Nycander, J. (2005). "Generation of internal tides in the deep ocean by tides." In: *JGR Oceans* 110.

Park, Jae-Hun and David Farmer (2013). "Effects of Kuroshio intrusions on nonlinear internal waves in the South China Sea during winter." In: *Journal of Geophysical Research: Oceans* 118.12, pp. 7081–7094. DOI: `https://doi.org/10.1002/2013JC008983`.

Rainville, Luc, Craig M. Lee, Daniel L. Rudnick, and Kai-Chieh Yang (2013). "Propagation of internal tides generated near Luzon Strait: Observations from autonomous gliders." In: *Journal of Geophysical Research: Oceans* 118.9, pp. 4125–4138. DOI: `https://doi.org/10.1002/jgrc.20293`.

Ray, Richard D. and Gary T. Mitchum (1997). "Surface manifestation of internal tides in the deep ocean: observations from altimetry and island gauges." In: *Progress in Oceanography* 40.1. Tidal Science In Honour of David E. Cartwright, pp. 135–162. ISSN: 0079-6611. DOI: `https://doi.org/10.1016/S0079-6611(97)00025-6`. URL: `https://www.sciencedirect.com/science/article/pii/S0079661197000256`.

Savva, M.A.C., H.A. Kafiabad, and J. Vanneste (2021a). "Inertia-gravity-wave scattering by three-dimensional geostrophic turbulence." In: *Journal of Fluid Mechanics* 916, A6. DOI: `10.1017/jfm.2021.205`.

— (2021b). "Inertia-gravity-wave scattering by three-dimensional geostrophic turbulence." In: *Journal of Fluid Mechanics* 916, A6. DOI: `10.1017/jfm.2021.205`.

Shakespeare, Callum J. (2023). "Eddy Acceleration and Decay Driven by Internal Tides." In: *Journal of Physical Oceanography* 53.12, pp. 2787 –2796. DOI: `10.1175/JPO-D-23-0127.1`. URL: `https://journals.ametsoc.org/view/journals/phoc/53/12/JPO-D-23-0127.1.xml`.

Simmons, H.L. and M.H. Alford. (2012). "Simulating the long-range swell of internal waves generated by ocean storms." In: *Oceanography* 25, pp. 30–41. DOI: `http://dx.doi.org/10.5670/oceanog.2012.39`.

Srinivasan, Margaret and Vardis Tsontos (2023). "Satellite Altimetry for Ocean and Coastal Applications: A Review." In: *Remote Sensing* 15.16. ISSN: 2072-4292. DOI: `10.3390/rs15163939`. URL: `https://www.mdpi.com/2072-4292/15/16/3939`.

Steele, Michael, Rebecca Morley, and Wendy Ermold (2001). "PHC: A Global Ocean Hydrography with a High-Quality Arctic Ocean." In: *Journal of Climate* 14.9, pp. 2079 –2087. DOI: `10.1175/1520-0442(2001)014<2079:PAGOHW>2.0.CO;2`. URL: `https://journals.ametsoc.org/view/journals/clim/14/9/1520-0442_2001_014_2079_pagohw_2.0.co_2.xml`.

Stevens, Bjorn, Victor Brovkin, and Antje Weitz (2022). *An introduction to Earth System Modelling.*

Storch, Hans von and W. Zwiers Francis (1999). *Statistical analysis in climate research.* Cambridge University Press.

Thomson, Richard E. and William J. Emery (2014). "Chapter 4 - The Spatial Analyses of Data Fields." In: *Data Analysis Methods in Physical Oceanography (Third*

Edition). Ed. by Richard E. Thomson and William J. Emery. Third Edition. Boston: Elsevier, pp. 313–424. ISBN: 978-0-12-387782-6. DOI: `https://doi.org/10.1016/B978-0-12-387782-6.00004-1`. URL: `https://www.sciencedirect.com/science/article/pii/B9780123877826000041`.

Vic, C., Naveira Garabato, Green A.C., and J.A.M. et al (2019). "Deep-ocean mixing driven by small-scale internal tides." In: *Nat Commun* 10. DOI: `https://doi.org/10.1038/s41467-019-10149-5`.

Vic, C., A.C. Naveira Garabato, and J.A.M. et al Green (2019). "Deep-ocean mixing driven by small-scale internal tides." In: *Nature Communications* 10, p. 2099. DOI: `https://doi.org/10.1038/s41467-019-10149-5`.

Wang, Y. and S. Legg (2025). "Agulhas rings locally enhance dissipation of internal tides." In: *Science Advances* 11.20. DOI: `DOI:10.1126/sciadv.adq5963`.

Wang, Yang and Sonya Legg (2023). "Enhanced Dissipation of Internal Tides in a Mesoscale Baroclinic Eddy." In: *Journal of Physical Oceanography* 53.10, pp. 2293 –2316. DOI: `https://doi.org/10.1175/JPO-D-23-0045.1`. URL: `https://journals.ametsoc.org/view/journals/phoc/53/10/JPO-D-23-0045.1.xml`.

Wang, Yang, Zhenhua Xu, Qun Li, Zhaohui Chen, Jia You, Baoshu Yin, and Robin Robertson (2023). "Observed internal tides in the deep northwestern Pacific by Argo floats." In: *Deep Sea Research Part II: Topical Studies in Oceanography* 207, p. 105248. ISSN: 0967-0645. DOI: `https://doi.org/10.1016/j.dsr2.2022.105248`. URL: `https://www.sciencedirect.com/science/article/pii/S096706452200234X`.

Waterhouse, Amy F., Samuel M. Kelly, Zhongxiang Zhao, Jennifer A. MacKinnon, Jonathan D. Nash, Harper Simmons, Dmitry Brahznikov, Luc Rainville, Matthew Alford, and Rob Pinkel (2018). "Observations of the Tasman Sea Internal Tide Beam." In: *Journal of Physical Oceanography* 48.6, pp. 1283 –1297. DOI: `10.1175/JPO-D-17-0116.1`. URL: `https://journals.ametsoc.org/view/journals/phoc/48/6/jpo-d-17-0116.1.xml`.

Wijesekera, H.W., W.J. Teague, E. Jarosz, D.W. Wang, H.J.S. Fernando, and Z.R. Hallock (2019). "Internal tidal currents and solitons in the southern Bay of Bengal." In: *Deep Sea Research Part II: Topical Studies in Oceanography* 168. Atmosphere-Ocean Dynamics of Bay of Bengal - Volume I, p. 104587. ISSN: 0967-0645. DOI: `https://doi.org/10.1016/j.dsr2.2019.05.010`.

Wu, Qian, Jing Meng, Xu Chen, and Yulin Guo (2024). "Behavior and Energy of the M2 Internal Tide in the Madagascar–Mascarene Region." In: *Remote Sensing* 16.22. DOI: `10.3390/rs16224299`. URL: `https://www.mdpi.com/2072-4292/16/22/4299`.

Yang, W., R. Li, and Y. et al. Feng (2023). "Cross-shelf variation of internal tides west of the Dongsha Plateau in the northern South China Sea." In: *Acta Oceanologica Sinica* 42, pp. 23–35. DOI: `https://doi.org/10.1007/s13131-023-2251-1`.

Yao, Jiaqi et al. (2025). "SWOT satellite for global hydrological applications: accuracy assessment and insights into surface water dynamics." In: *International Journal of Digital Earth* 18.1, p. 2472924. DOI: `10.1080/17538947.2025.2472924`.

Zhao, Zhongxiang (2014). "Internal tide radiation from the Luzon Strait." In: *Journal of Geophysical Research: Oceans* 119.8, pp. 5434–5448. DOI: `https://doi.org/10.1002/2014JC010014`.

Zhao, Zhongxiang and Matthew H. Alford (2009). “New Altimetric Estimates of Mode-1 M2 Internal Tides in the Central North Pacific Ocean.” In: *Journal of Physical Oceanography* 39.7, pp. 1669 –1684. DOI: `10.1175/2009JPO3922.1`.

Zhao, Zhongxiang, Matthew H. Alford, James B. Girton, Luc Rainville, and Harper L. Simmons (2016). “Global Observations of Open-Ocean Mode-1 M2 Internal Tides.” In: *Journal of Physical Oceanography* 46.6, pp. 1657 –1684. DOI: `10.1175/JPO-D-15-0105.1`.

Zhao, Zhongxiang, Matthew H. Alford, James Girton, T. M. Shaun Johnston, and Glenn Carter (2011). “Internal tides around the Hawaiian Ridge estimated from multisatellite altimetry.” In: *Journal of Geophysical Research: Oceans* 116.C12. DOI: `https://doi.org/10.1029/2011JC007045`.

Zilberman, Nathalie V. et al. (2023). “Observing the full ocean volume using Deep Argo floats.” In: *Frontiers in Marine Science* Volume 10 - 2023. ISSN: 2296-7745. DOI: `10.3389/fmars.2023.1287867`. URL: `https://www.frontiersin.org/journals/marine-science/articles/10.3389/fmars.2023.1287867`.

von Storch, J.-S., E. Hertwig, V. Luschow, N. Bruggemann, H. Haak, P. Korn, and V. Singh (2023). “Open-ocean tides simulated by ICON-O, version icon-2.6.6.” In: *Geoscientific Model Development* 16.17, pp. 5179–5196. DOI: `10.5194/gmd-16-5179-2023`. URL: `https://gmd.copernicus.org/articles/16/5179/2023/`.

von Storch, Jin-Song and Veit Lüschow (2023). “Wind power input to ocean near-inertial waves diagnosed from a 5-km global coupled atmosphere-ocean general circulation model.” In: *Journal of Geophysical Research: Oceans* 128, e2022JC019111. URL: `https://doi.org/10.1029/2022JC019111`.

EIDESSTATTLICHE VERSICHERUNG | DECLARATION ON OATH

Hiermit erkläre ich an Eides statt, dass ich die vorliegende Dissertationsschrift selbst verfasst und keine anderen als die angegebenen Quellen und Hilfsmittel benutzt habe. Sofern im Zuge der Erstellung der vorliegenden Dissertationsschrift generative Künstliche Intelligenz (gKI) basierte elektronische Hilfsmittel verwendet wurden, versichere ich, dass meine eigene Leistung im Vordergrund stand und dass eine vollständige Dokumentation aller verwendeten Hilfsmittel gemäß der Guten wissenschaftlichen Praxis vorliegt. Ich trage die Verantwortung für eventuell durch die gKI generierte fehlerhafte oder verzerrte Inhalte, fehlerhafte Referenzen, Verstöße gegen das Datenschutz- und Urheberrecht oder Plagiate.

Hamburg, December 2, 2025

Zoi Kourkouraidou

UEBEREINSTIMMUNGSERKLÄRUNG | DECLARATION ON CONFORMITY

Ich versichere, dass dieses gebundene Exemplar der Dissertation und das in elektronischer Form eingereichte Dissertationsexemplar (über den Docata-Upload) sowohl das bei der Fakultät zur Archivierung eingereichte gedruckte gebundene Exemplar der Dissertationsschrift identisch sind.

I hereby confirm that this bound copy of the dissertation and the electronically submitted version (via the Docata upload) are identical to the printed bound copy of the dissertation submitted to the faculty for archiving.

Hamburg, December 2, 2025

Zoi Kourkouraidou